NATIONAL & INTERNATIONAL SCIENTIFIC EVENTS

International Conference on Ubiquitous Information Management and Communication

Venue: Offline and Online
Location: Kuala Lumpur, Malaysia

Begins: January 03 2024
Ends: January 05, 2024

IEEE Consumer Communications & Networking Conference

Venue: Flamingo Hotel
Location: Las Vegas, USA

Begins: January 06 2024
Ends: January 09, 2024

The 37th International Conference on Micro Electro Mechanical Systems

Venue: AT&T Hotel and Conference Center
Location: Texas, USA

Begins: January 21 2024
Ends: January 25, 2024

The 14th International Conference on Key Engineering Materials

Venue: N/A
Location: Dubai, United Arab Emirates

Begins: March 06 2024
Ends: March 09, 2024

10th International Conference on Computer Technology Applications

Venue: Hotel Ibis Wien Mariahilf
Location: Vienna, Austria

Begins: May 15 2024
Ends: May 17, 2024

12nd World Biomaterials Congress

Venue: EXCO
Location: Daegu, Korea

Begins: May 26 2024
Ends: May 31, 2024

22nd Triennial Congress of The International Ergonomics Association

Venue: Jeju International Convention Center
Location: Jeju Island, Korea

Begins: August 25 2024
Ends: August 29, 2024

18th European Conference on Soil Mechanics and Geotechnical Engineering

Venue: Altice Arena
Location: Lisbon, Portugal

Begins: August 26 2024
Ends: August 30, 2024

13th European Symposium on Martensitic Transformations

Venue: Lecco Campus
Location: Lecoo, Italy

Begins: August 26 2024
Ends: August 30, 2024

49th International Conference on Infrared, Millimeter, and Terahertz Waves

Venue: Perth Convention and Exhibition Centre
Location: Perth, Australia

Begins: September 01 2024
Ends: September 06, 2024

38th Internation Conference on Coastal Engineering

Venue: The Pontifical Gregorian University
Location: Rome, Italy

Begins: September 08 2024
Ends: September 14, 2024

69th IEEE Holm Conference on Electrical Contacts

Venue: Graduate Hotel
Location: Annapolis, Maryland, USA

Begins: 06 October 2024
Ends: 10 October, 2024

Abstracted & Indexed in:

TR Dizin Mühendislik ve Temel Bilimler Veri Tabanı | CrossRef | Google Scholar | MIP Database | StuartxChange | ResearchBib | Scientific Indexing Services (SIS)

HJSE Official Journal of Hitit University Volume 10, Issue 4, 2023 dergipark.org.tr/en/pub/hjse

HITIT UNIVERSITY

ISSN 2148-4171

JOURNAL OF SCIENCE & ENGINEERING

HITTITE

Volume 10, Issue 4, 2023

dergipark.org.tr/en/pub/hjse

HJSE Official Journal of Hitit University Volume 10, Issue 4, 2023 dergipark.org.tr/en/pub/hjse

JOURNAL OF SCIENCE & ENGINEERING
HITTITE

This study aims to determine the optimum effective porous radius and wick permeability for this reactor and investigate the effect of effective porous radius and wick permeability on the heat pipe limitations.

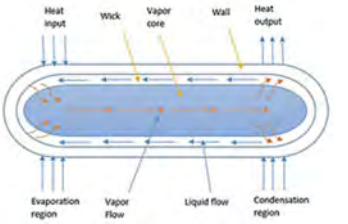

The study conducted a comprehensive examination of the Middle-Late Miocene period in the Dağpazarı, Ballı, and Mut Formations by analyzing the ostracod fauna and utilizing strontium isotope chemostratigraphic dating.

Bending of a laminated composite beam under to a sinusoidal loading is carried out for simply support boundary condition for a specific cross-ply stacking sequence. To demonstrate the accuracy of the analytical results, a computer-aided engineering (CAE) approach is used.

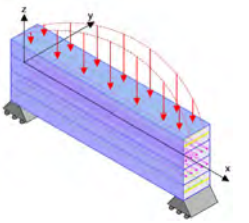

The objective of this study is to fabricate micron-sized hydrogels as adsorbents for DNA.

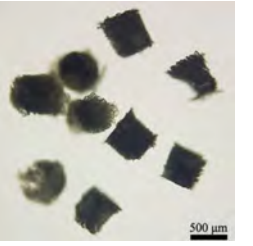

In this study, we produced Aluminum oxide (Al2O3) reinforced carbon fiber and glass fiber reinforced polymer (CFRP, GFRP) composites and investigated mechanical and tribological properties.

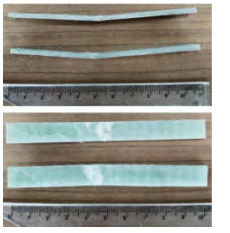

In this work, three distinct compatibilizers were introduced to composites based on polypropylene (PP) and perlite to improve interactions between the constituents.

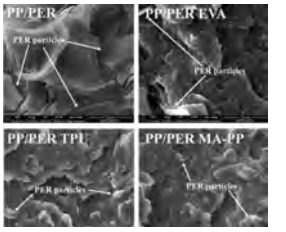

JOURNAL OF SCIENCE & ENGINEERING
HITTITE

This study explores the potential use of waste cooking sunflower oil (WSO) as an eco-friendly collector for coal slime flotation.

Especially when considering the amount of power used in waste plants and the corresponding waste heat generated, an approach to recover waste heat from these facilities has been proposed.

Editor's Office
Tel: +90 364 227 45 33 / 12 36
Fax: +90 364 227 45 35
Email: alikilicarslan@hitit.edu.tr

Subscription Service:
Tel: +90 364 227 45 33 / 12 82
Fax: +90 364 227 45 35
Email: hjse@hitit.edu.tr

EDITORIAL BOARD

Journal Name	: HITTITE JOURNAL OF SCIENCE AND ENGINEERING
Year	: 2023
Managing Editor	: Prof. Dr. Ali KILIÇARSLAN
Managing Office	: Hitit University Faculty of Engineering
Managing Office Tel	: +90 364 227 45 33 / 12 36
Publication Language	: English
Publication Type	: Peer Reviewed, Open Access, International Journal
Delivery Format	: 4 times a year (quarterly)
Print ISSN	: 2149-2123
Online ISSN	: 2148-4171
Publisher Address	: Hitit Üniversitesi Kuzey Kampüsü Çevre Yolu Bulvarı 19030 Çorum / TÜRKİYE
Publisher Tel	: +90 364 227 45 33/1236

As the team of Hittite Journal of Science and Engineering, we have published the new issue (2023-Volume 10, Issue 4). As a Editor in Chief, I am grateful to all our authors and contributing reviewers of this issue. I also would like to thank to the President of Hitit University, Prof. Dr. Ali Osman Öztürk, for his support and interest in HJSE and also to the Associate Editors of HJSE, namely Prof. Dr. Dursun Ali Kose and Assoc. Prof. Dr. Oncu Akyildiz, as well as our Production Editors, Asst. Prof. Dr. Mustafa Reşit Haboğlu, Asst. Prof. Dr. Erhan Çetin, Harun Emre Kıran and Ömer Faruk Tozlu for their invaluable efforts in making of the journal.

I would like to share a good news with the researchers, scientists and reviewers participating with HJSE Team. HJSE has been recently accepted to the DOAJ index, one of the internationally important indexes. DOAJ (Directory of Open Access Journals); It is an independent index containing approximately 20 thousand peer-reviewed open access journals, covering all fields of science, technology, medicine, social sciences, arts and humanities. DOAJ is supported internationally by libraries, publishers and research institutions.

As Editor in Chief, I would like to thank to the authors submitting their papers to HJSE. In this issue, the articles from the eight branches of engineering including "Manufacturing", "Jeological", "Mechanical", "Biomedical", "Metallurgical and Materials", "Textile", "Mining" and "Energy" Engineering were published.

The new team members of HJSE have joined us as "Section Editors". I am grateful to them for accepting this important task. It is an honour for me to announce them. Prof. Dr. Murat Hoşöz from the Department of Automotive Engineering, Kocaeli University, Prof. Dr. Kazim Savaş Bahçeci from the Department of Food Engineering, Hitit University, Prof. Dr. Cengiz Baykasoğlu from the Department of Mechanical Engineering, Hitit University and Prof. Dr. Akif Akgül from the Department of Computer Engineering, Hitit University.

It's my pleasure to invite the researchers and scientists from all branches of engineering to join us by sending their best papers for publication in Hittite Journal of Science and Engineering

Dr. Ali Kilicarslan

Editor-in-Chief

Research Article
Hittite Journal of Science and Engineering, 2023, 10 (4) 279–285
ISSN NUMBER: 2149–2123
DOI: 10.17350/HJSE19030000317

The Effect of Wick Permeability and Porous Radius on Capillary and Entrainment Limit in A Heat Pipe Reactor

Gizem Bakır
Sivas Cumhuriyet University, Department of Manufacturing Engineering, Sivas, Türkiye

Article History:
Received: 2023/01/30
Accepted: 2023/10/24
Online: 2023/12/31

***Correspondence to**: Gizem Bakır,*
E-Mail: gbakir@cumhuriyet.edu.tr
Phone: +90 346 487 00 00/2338

This article has been checked for similarity.

ABSTRACT

For heat extraction in nuclear systems, interest in the design of nuclear reactors with heat pipes has increased. The determination of heat limitations is one of the remarkable factors for safety when heat pipes are used for nuclear systems. In this study, capillary and entrainment limit values for the heat pipe were calculated in a heat pipe reactor with potassium working fluid operating at 650 K. Five different effective porous radii ($10.1x10^{-6}$, $10.225x10^{-6}$, $10.35x10^{-6}$, $10.425x10^{-6}$ and $10.6x10^{-6}$ m) and five different wick permeability ($4.75x10^{-12}$, $5x10^{-12}$, $5.25x10^{-11}$, $5.5x10^{-12}$ and $5.75x10^{-12}$ m^2) is considered for sintered copper wick heat pipe. While the effects of effective porosity radius, wick permeability, and wick radius on the capillary barrier were studied, only the effects of effective porosity radius were studied. While the effects of effective porosity radius, wick permeability, and wick radius on the capillary barrier are studied, only the effects of effective porosity radius are studied. The highest values of the capillary and entrainment limits are obtained when the porosity radius is $10.1x10^{-6}$ m. Besides, maximum capillary limits are achieved when the wick permeability is $5.75x10^{-12}$ m^2 and the effective porosity radius is $10.1x10^{-6}$. This study aims to determine the optimum effective porous radius and wick permeability for this reactor and investigate the effect of effective porous radius and wick permeability on the heat pipe limitations.

Keywords:
Heat pipe; Nuclear reactor; Porous radius; Wick permeability; Wick radius; Capillary limit; Entrainment limit

INTRODUCTION

The heat-pipe-cooled reactor stands out with its high-power density, ease of handling, long-term life (>5 years), and reliability. Recently, the investigation of heat pipes for heat transfer in nuclear cores has been a research topic for researchers [1-4]. The heat pipe is a highly efficient and passive heat transfer mechanism that uses latent heat from evaporation without pump power. It is used in many fields, including nuclear reactors, due to its high efficiency. There are some limitations to the heat transfer of heat pipes. Incorrect determination of heat transfer limits may result in calculating the heat extraction values of the heat pipes incorrectly, in this case, thus causing accidents. The capillary limit is one of the most significant limits for determining these limitations.

Heat pipe reactors have become a popular topic due to the efficiency of heat pipes and their increasing area of applications. Sun et al [5] designed a 120 kWe lithium heat pipe reactor power supply that can be used for multiple applications. In their design, 70% enriched uranium nitride fuel and lithium heat pipes were used. For their study, an MCORE code combining MCNP and ORIGEN was used. In general, it was found that the designed basic parameters met the safety requirements, and the reactor was safe in terms of neutronics. Zhang et al. [6], designed a fast reactor that transfers heat to potassium-filled high-temperature pipes and thermoelectric generators. Both finite element and thermal resistance network methods were used to simulate the potassium heat pipe system. The normal operating conditions and two accident scenarios were calculated to prove the reliability of the new system model. Liu et al. [7], proposed the design of a new passive heat removal system using heat pipe technology to develop the passive safety feature of the molten salt reactor. An experimental system was developed to validate the design of the passive heat removal system of the reactor. An eutectic salt mixture was chosen as the working fluid, and different ranges of it were considered for the heat pipes. They reached lower temperatures when they had a greater distance between the heat pipe spacings. The distance between heat pipe spacings was an important factor affecting the temperature difference. Wang et al.

Cite as:
Bakir G, "The effect of wick permeability and porous radius on capillary and entrainment limit in a heat pipe reactor". Hittite J Sci Eng. 2023;10 (4): 279-285. doi:10.17350/hjse19030000317

[8], analyzed a molten salt reactor using high-temperature heat pipe technology. In their study, they set up an experimental system to verify the feasibility of the passive heat extraction system in the reactor. The experimental results showed that although some of the heat pipes did not work normally, the heat pipe system removed a significant amount of heat from the drain tank. Wang et al. [9], investigated the design of a 25 kWe heat pipe cooled reactor for multiple uses. Based upon the heat pipe cooled reactor design, a thermalhydraulic computer code was developed to analyze the time-dependent and time-independent performance of the reactor. For this reactor, 65% enriched UN and potassium are used as fuel and heat pipe working fluid, respectively. In their results, the selected parameters met the safety requirements. Guillen and Turner [10] used axially grooved heat pipes and investigated the applicability of these heat pipes for heat extraction in microreactors. The HTPIPE code is used for the analysis. The performance limits of a sodium heat pipe with a threaded square wick structure were compared to those of an equivalent heat pipe with a circular wick. It was reported that, at operating temperatures below 777 °C the annular wick outperforms the corrugated wick, while at temperatures above 777 °C the corrugated wick outperforms the annular wick.

Some researchers have studied the capillary limit in the heat pipe. Subedi et al. [11] studied the thermal properties of a flat micro heat pipe. They calculated the capillary and maximum temperature limits to determine the maximum heat transfer. For the theoretical results of the optimized wick design, the maximum heat transfer rate and the surface temperature distribution were compared for the capillary limit and maximum temperature limit cases. Yu et al. [12] analyzed the effect of the wick geometry of a heat pipe on the heat transfer capacities. A special analytical computer model was designed using the Newton-Raphson method and applied this model to analyze the capillary, viscous, entrainment, sonic, and boiling heat transfer limits of the heat pipe. It was found that the capillary limit leads to the determination of the maximum heat transfer limit. Xin et al. [13] aimed to design the optimum mini grooved flat heat pipe. A mathematical model of axial fluid flow and heat transfer in a mini grooved flat heat pipe has been created. They emphasized that capillary radius values are an important parameter for calculating capillary limit values. Zhou et al. [14] investigated experimentally the effects of ultra-thin heat pipe, wick width, and fill rate parameters on thermal performance. It was found that when the wick width is 4 mm, the maximum heat carrying capacity of the ultra-thin heat pipe can reach 8.5 W. Zhang et al. [15] characterized the porous structures and capillary performances of the wicks and measured the thermal efficiency of the heat pipes to calculate the capillary limit of the heat pipe. Copper powder sintered heat pipes in various shapes, dendritic and irregular powder heat pipes provided superior heat transfer capabilities. Some researchers work on entrainment limit. Sandeep and Prakash [16] conducted a study on copper heat pipe filling with acetone. The capillary and entrainment limits were investigated. Python code was used for calculating capillary and entrainment limits. The highest values of capillary and entrainment limits were found as 52.6 W and 98.65 W, respectively. Mansour [17] researched the heat convection limits and heat transfer coefficient for a heat pipe using copper-acetone at various vapor temperatures. A new correlation for the heat transfer coefficient was developed. Latent heat evaporation, pipe diameter, and Reynolds number were effective on all heat transfer limits presented. It was observed that while an increment in the capillary, entrainment and capillary limits occurs with the increase in vapor temperature, the boiling limit is reduced.

THE CONCEPT OF HEAT PIPE

A heat pipe is a mechanism that makes it possible to transport thermal energy efficiently. It consists of a structure whose inner surface is covered with a thin layer of porous material, usually called grooved. The container can be made in a cylindrical shape or in any other suitable shape. The pores of the wick are filled with a working liquid suitable for the application, and the liquid vapor covers the remaining internal volume. Since the vapor and its liquid are in equilibrium, the pressure value in the vessel is same to the vapor pressure value, which conforms with saturation conditions [18].

Heat pipes have a simple configuration and a simple heat transfer mechanism. The heat pipe structure is presented in Fig. 1. Heat pipes allow very efficient heat transfer from one end to the other. When heat is applied on the evaporator part, while the working liquid vaporizes from the wick, it causes the condensation of the vapor on the wick in the condensation part and removes heat by releasing the latent heat of the vapor [18].

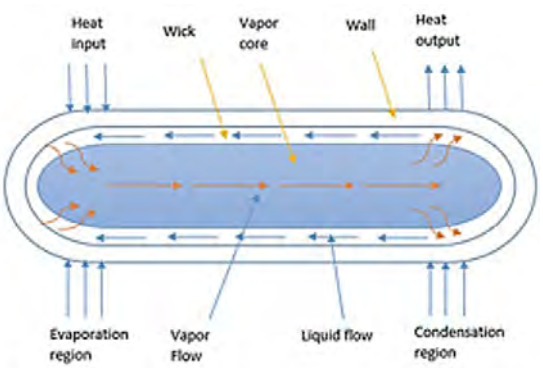

Figure 1. Structure of heat pipe

Heat Pipe Nuclear Reactors

Reactors require a circulating pump or transport fission or decomposition heat with liquid or gas based on a natural circulation, so the use of heat pipes for primary heat transfer is a new approach. The usage of heat pipes technology for nuclear reactors is new for the nuclear industry. However, heat pipe technology has been researched for decades and numerous tests have been conducted in both radiation and non-radiation test environments.

A heat pipe reactor simplifies system integration. Namely eliminating the components required for a pumped loop. This simplifies the system. Other advantages of using heat pipes in a nuclear reactor include modularity, testability, simplified system integration, passivity, and elimination of single point failures. It has also been suggested that the reactor design can operate for more than 10 years without adding fuel and is best suited to serve as a nuclear battery rather than a central power source [19,20].

In this study, the effects of important parameters affecting the capillary limit, such as porosity radius, wick permeability, and wick radius were investigated in a heat pipe reactor with potassium liquid as working fluid. Besides, the effect of the porous radius was studied for entrainment limit.

MATERIALS AND METHODS

The dimensions and materials of the potassium liquid heat pipes used in this study were taken from the literature [21] and the sizes of the heat pipes are presented in Table 1.

Table 1. Heat Pipe Dimension [21].

Evaporation length	*450 mm*
Adiobatic length	*600 mm*
Condenser length	*1200 mm*
Vapor core radius	*18 mm*
Wall thickness	*30 mm*
Wick thickness	*26.4 mm*

The operating temperature of the heat pipe nuclear reactor which is a hypothetical nuclear power plant was assumed to be 650 K and calculations were made based on 650 K. The potassium working fluid was used following the work of [22, 23] and at the above assumed temperature. Neutron absorption values are also one of the important factors in selecting a material for a nuclear reactor. Potassium is a suitable material for use in nuclear reactors because it has a low neutron absorption cross section.

The most appropriate correlations for the capillary limit were taken from the literature to correctly calculate the heat extraction value in a heat pipe nuclear reactor. The necessary parameters for the heat pipe calculations were taken from the values given in Table 1. In addition, the thermophysical properties of potassium were calculated using Ref [24-27].

The porosity radius and wick permeability of the sintered copper tube heat pipe were selected and evaluated following the literature [28-31]. Some important parameters affect the capillary limit, such as porosity radius, wick permeability, wick radius, thermophysical properties of the fluid, and contact angle. Five different porosity radius (10.1×10^{-6}, 10.225×10^{-6}, 10.35×10^{-6}, 10.425×10^{-6}, and 10.6×10^{-6} m) and five different wick permeabilities (4.75×10^{-12}, 5×10^{-12}, 5.25×10^{-11}, 5.5×10^{-12}, and 5.75×10^{-12} m^2) were considered and the effects of these parameters on the capillary limit were investigated. In these calculations, the capillary limit was calculated using Eq. (1) and it is given as follow,

$$Q_c = \frac{\sigma L_v \rho_l}{12\mu_1} \cdot \frac{KA_w}{l_{eff}} \cdot \left(\frac{2}{r_{eff}} - \frac{\rho_l . g . \cos\psi . l_t}{\sigma} \right) \quad (1)$$

In Eq. (1) , lv is latent heat (J/kg), σ is surface tension (N/m), Aw is cross-sectional area of wick (m^2), ρl is density of liquid (kg) /m^3), K is wick permeability (m^2), μl is viscosity of fluid (N·s/m^2), reff effective porosity radius of wick (m), g is gravitational force (9.8 m/s^2) and lt is total length of heat pipe (m). where ψ is the contact angle between the liquid and the wick. Here this angle is assumed to be 90°. reff is the effective radius of the surface pore (m) and K (wick permeability) values were taken from ref [28-31] in accordance with the literature. leff is the effective length of the heat pipe (m) and is expressed as follows;

$$l_{eff} = \frac{L_{evaporator}}{2} + L_{adiobatic} + \frac{L_{condenser}}{2} \quad (2)$$

where $L_{evaporator}$ is the evaporation zone length (m), the $L_{adyabatic}$ is adiabatic zone length (m) and the $L_{condenser}$ is the condensation zone length (m).

Five different porosity radii (10.1×10^{-6}, 10.225×10^{-6}, 10.35×10^{-6}, 10.425×10^{-6}, and 10.6×10^{-6} m) were considered and the effects of these parameters on the entrainment limit were investigated. The entrainment limit was calculated by using Eq. (3) The equation is given as follow [28];

$$Q_{sr} = A_v . L_v . \sqrt{\frac{\rho_v . \sigma}{2 . r_c}} \quad (3)$$

Here, r_c is the hydraulic radius of the surface pore (m), A_v is vapor core cross-sectional area (m^2) and ρ_v is vapor

density (kg/m^3). It is assumed that the wick hydraulic radius is equal to the effective of porosity radius for entrainment limit.

All calculations are done by using calculator.

RESULTS AND DISCUSSSION

Capillary Limit

The capillary limit is related to the fundamental conditions that enable heat pipe operation and is formed due to capillary pressure differentiation at the vapour-liquid interfaces in the section of the evaporator and condenser. The driving potential for liquid circulation is the capillary pressure differentiation, the maximum capillary pressure has to be higher than the sum of all pressure drops in the heat pipe.

The maximum heat transfer rate can be specified because of capillary limitation for most of the heat pipes, [28,32].

Effect of Porosity Radius on Capillary Limit

The pore radius directly affects the capillary pumping potential, as a smaller pore radius results in higher capillary pressure. Pore size and wick properties affect the operating limits of heat pipes. It has become a popular topic to work on the fabrication of new wicks with improved properties that can hinder the development of vapor in the porous structure or release it easily. Many studies have been conducted on the effects of the properties of the porous structure on heat limitation [32-34].

Fig. 2 demonstrates the variation of the capillary limit with temperature for all effective porosity radii. Eq. (1) is used to calculate the capillary limit. As can be seen from the figure, the capillary limit does not change significantly with increasing temperature. The values of capillary limit were calculated when the effective porosity radius was 10.1x10^{-6}, 10.225x10^{-6}, 10.35x10^{-6}, 10.425x10^{-6} and 10.6x10^{-6} m (K=4.75x10^{-12} m^2). The capillary limit changes inversely with the effective porosity radius. For this reason, the capillary limit values decrease as the effective porosity radius increases. The highest capillary limit values were found the effective porosity radius was 10.1x10^{-6} m, while the lowest capillary limit values were found when the porosity was 10.6x10^{-6} m.

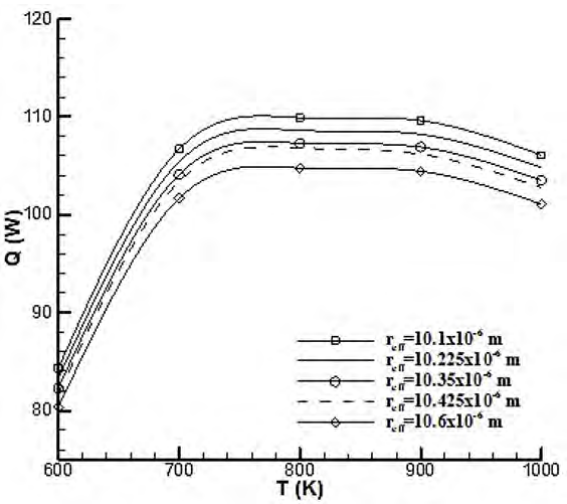

Figure 2. The variation of capillary limit with temperature for all effective porosity radius

The graph of capillary limits for five different effective porosity radii at a temperature of 650 K is presented in Fig. 3. It can be seen from the Fig. 3, the value of the capillary limit value decreases as the effective porosity radius increases. When the values of effective porosity radius are 10.1x10^{-6}, 10.225x10^{-6}, 10.35x10^{-6}, 10.425x10^{-6} and 10.6x10^{-6} m at a temperature of 650 K, the capillary limit values are 95.5, 94.3, 93.2, 92.5 and 90.8 W, respectively. The highest capillary limits occurred when the effective porosity radius was 10.1x10^{-6} m. Since the effective porosity radius inversely proportional with the capillary limits, the highest capillary limit is obtained when the lowest effective porosity radius is used.

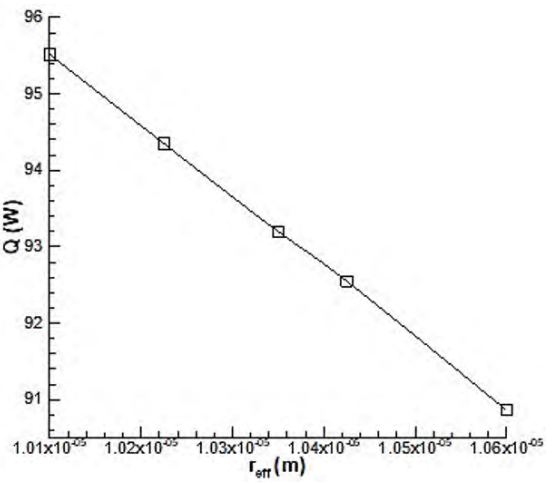

Figure 3. Variation of capillary limit values for all porosity radius at a temperature of 650 K.

Effect of Wick Permeability on Capillary Limit

The increment in the permeability can cause a decrement in flow resistance and increment of the capillary limit. The wick permeability is one of the most significant parameters effecting the capillary limit. The effect of wick permeability on capillary limit is an interesting topic for researchers [35,36].

Fig. 4 shows the change in the effect of wick permeability on the capillary limit with temperature. As can be seen, the capillary limit does not change significantly with incre-

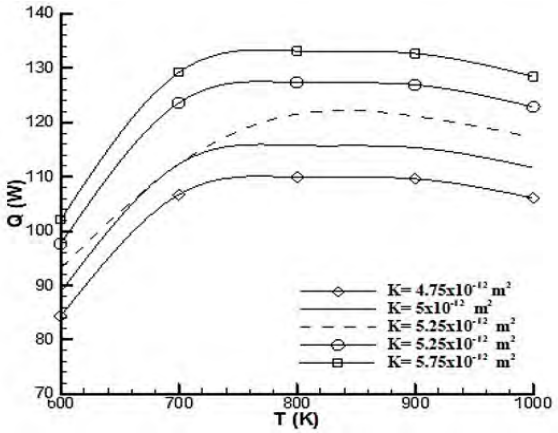

Figure 4. Variation of the effect of wick permeability on the capillary limit with temperature

asing temperature. The capillary limit increases with increasing wick permeability. The reason for this is that the wick permeability and the capillary limit are directly proportional. The capillary limits were calculated for wick permeability $4.75x10^{-12}$, $5x10^{-12}$, $5.25x10^{-11}$, $5.5x10^{-12}$ and $5.75x10^{-12}$ m^2 (the porosity radius was assumed to be $10.1x10^{-6}$ m). The results show that the highest capillary limit is obtained when the wick permeability is $5.75x10^{-12}$ m^2, while the lowest capillary limit is obtained when it is $4.75x10^{-12}$ m^2.

The graph of capillary limits for five different effective wick permeability values at a temperature of 650 K is shown in Fig. 5. The wick permeability is plotted such that the capillary limit value increases with increasing permeability. From Fig. 5, it can be seen that as the permeability increases, the capillary limit value also increases. At 650 K, when the permeability of the wicks is $4.75x10^{-12}$, $5x10^{-12}$, $5.25x10^{-11}$, $5.5x10^{-12}$ and $5.75x10^{-12}$ m^2, the capillary limit values are 95.5, 100.5, 102.7, 110.6 and 115.6 W, respectively. The case where the capillary limit is the highest is the one where the wick permeability value is $5.75x10^{-12}$ m^2.

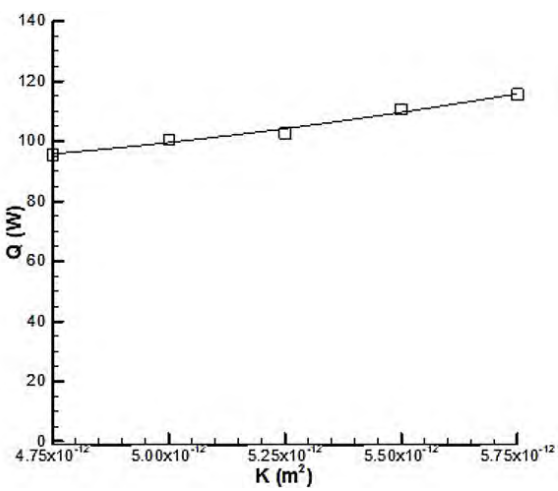

Figure 5. Variation of capillary limit values for all wick permeability values at a temperature of 650 K

Entrainment Limit

Since vapor and liquid move in converse directions, a shear force occurs at the interface between liquid vapor interfaces. At high relative speeds, liquid droplets can break off from the wick surface and enter the vapor flowing into the condensation region. If the entrainment is too much, the evaporation zone dries out. The entrainment limit is the heat transfer rate at which this phenomenon occurs. Entrainment is determined by the sound of droplets hitting the condenser region end of the heat pipe. The entrainment limit is generally associated with either low or medium temperature small diameter heat pipes or heat pipes has high temperature when heat input is high in the evaporator zone. Eq. (3) is used to calculate the entrainment limit.

Effect of Porosity Radius on Entrainment Limit

Fig. 6 shows the variation of entrainment limit with temperature for all effective porosity radii. Eq. (1) is used in the capillary limit calculations. It can be seen from Fig. 5 that entrainment increases with increasing temperature. The entrainment limits were calculated once the effective porosity radius was $10.1x10^{-6}$, $10.225x10^{-6}$, $10.35x10^{-6}$, $10.425x10^{-6}$, and $10.6x10^{-6}$ m. The entrainment limit and the effective porosity radius are inversely proportional. Therefore, the entrainment limits reduce as the effective porosity radius increases. When the effective porosity radius was $10.1x10^{-6}$ m, the highest entrainment limit was achieved.

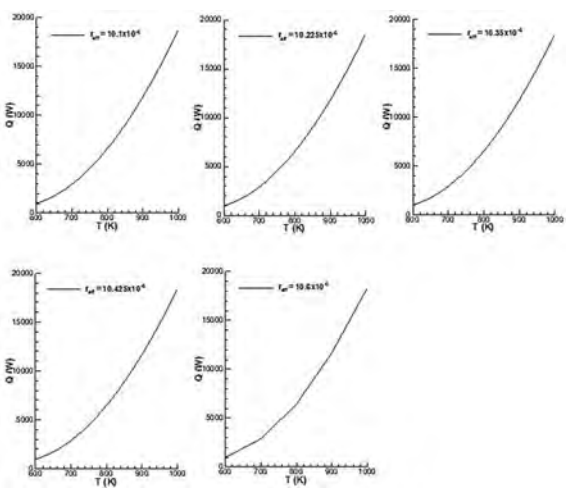

Figure 6. Variation of entrainment limit with temperature for all effective porosity radius.

In Fig. 7 entrainment limits for five values of the effective porosity radius at a temperature of 650 K is presented. Increasing the effective porosity radius resulted in decreasing the entrainment limits. At 650 K, when the effective porosity radius is $10.1x10^{-6}$, $10.225x10^{-6}$, $10.35x10^{-6}$, $10.425x10^{-6}$, and $10.6x10^{-6}$ m, the entrainment limits are 2310, 1968, 1956,

1949, and 1945 W, respectively. The highest entrainment limit was reached when the effective porosity radius is $10.1x10^{-6}$ m.

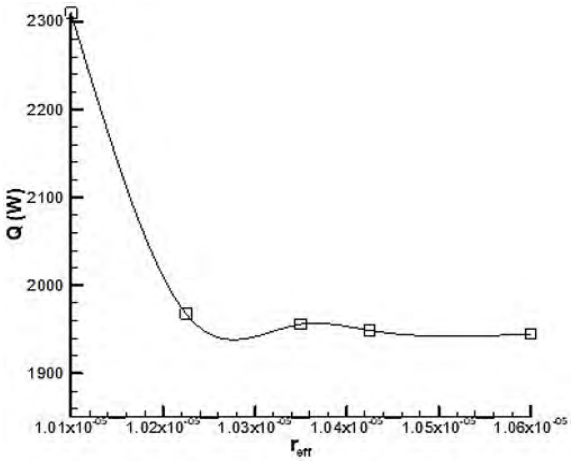

Figure 7. Variation of entrainment limit values for all values for all porosity radius at a temperature of 650 K

CONCLUSION

In this study, the effects of effective porosity radius and wick permeability on capillarity and entrainment limit in a heat pipe nuclear reactor were investigated. Based on the results of this study, the following conclusions are made:

- The highest capillary limit was reached when the effective porosity was $10.1x10^{-6}$ m.
- A decrease in effective porosity results in an increase in capillary limit
- The case where the capillary limit is obtained highest is when the wick permeability value is $5.75x10^{-12}$ m^2.
- An increase in wick permeability results in a increase in capillary limit.
- When the effective porosity radius was $10.1x10^{-6}$ m, the highest entrainment limit was achieved.
- An decrease in effective porosity results in a increase in entrainment limit.
- It has been found that the capillary limit is more effective than the entrainment limit in determining the heat pipe limitation. This is because the capillary limit has lower temperature values.
- For this heat pipe reactor, the best effective porosity radius and permeability are determined as $10.1x10^{-6}$ m and $5.75x10^{-12}$ m^2, respectively.

CONFLICT OF INTEREST

The author deny any conflict of interest.

REFERENCES

1. Wright SA, Lipinski RJ, Pandya T, Peters. Proposed design and operation of a heat pipe reactor using the Sandia National Laboratories Annular Core test facility and existing UZrH fuel pins. Space Technology and Applications International Forum–Staif. 2005,746; 449-60. doi:10.1063/1.1867161
2. Koenig DR, Ranken WA, Salmi EW. Heat–pipe reactors for space power applications. Journal of Energy. 1977, 237-43. doi:10.2514/3.62334
3. Greenspan E. Solid Core Heat–Pipe Nuclear Battery Type Reactor, University of California. 2008.doi:10.2172/940911.
4. Ma Y, Chen E, Yu H, Zhong R, Deng J, Chai X, Huang S, Ding S, Zhang Z. Heat pipe failure accident analysis in megawatt heat pipe cooled reactor. Annals of Nuclear Energy. 2020, 149; 107755. doi: 10.1016/j.anucene.2020.107755
5. Sun H, Wang C, Ma P, Tian W, Qiu S, Su G. Conceptual design and analysis of a multipurpose micro nuclear reactor power source. Annals of Nuclear Energy. 2018,121; 118-27. doi:10.1016/j.anucene.2018.07.025
6. Zhang W, Zhang D, Liu X, Tian S, Qiu S, Su G. Thermal–hydraulic analysis of the thermoelectric space reactor power system with a potassium heat pipe radiator. Annals of Nuclear Energy. 2020, 136;19–25. doi: 10.1016/j.net.2019.06.021
7. Liu X, Sun H, Tang S, Wang C, Tian W, Qiu S, Su G. Thermal - hydraulic design features of a micronuclear reactor power source applied for multipurpose. International Journal of Energy Research. 2019, 43; 4170-183. doi: 10.1002/er.4542
8. Wang C, Liu M, Zhang D, Qiu S, Su GH, Tian W. Experimental study on transient performance of heat pipe–cooled passive residual heat removal system of a molten salt reactor. Progress in Nuclear Energy. 2020, 118; 103113. doi: 10.1016/j. pnucene.2019.103113
9. Wang C, Sun H, Yang S, et al., Thermal–hydraulic analysis of a new conceptual heat pipe cooled small nuclear reactor system. Nuclear Engineering and Technology. 2020, 52; 19–26. doi: 10.1016/j.net.2019.06.021
10. Guilen DP, Turner CG, Assessment of Screen–Covered Grooved Sodium Heat Pipes for Microreactor Applications. Nuclear Technology. 2022, 208; 1301-310. doi:10.1080/00295450.2021 .1977085.
11. Subedi B, Kim SY, Jang SP, Kedzierski MA. Effect of mesh wick geometry on the maximum heat transfer rate of flat–micro heat pipes with multi–heat sources and sinks. International Journal of Heat and Mass Transfer. 2019, 131; 537-45. doi: 10.1016/j.ijheatmasstransfer.2018.11.086
12. Yu M, Diallo TMO, Zhao X, Zhou J, Du Z, Ji J, Chen Y, Analytical study of impact of the wick's fractal parameters on the heat transfer capacity of a novel micro–channel loop heat pipe. Energy. 2018, 158; 746–759. Doi: 10.1016/j. energy.2018.06.075
13. Xin F, Ma T, Wang Q, Thermal performance analysis of flat heat pipe with graded mini–grooves wick. Applied Energy. 2018, 228; 2129-139. Doi: 10.1016/j.apenergy.2018.07.053

14. Zhou W, Li Y, Chen Z, Effect of the passage area ratio of liquid to vapor on an ultra−thin flattened heat pipe, Applied Thermal Engineering. 2019, 162; 114215.

15. Zhang J, Lian L, Liu Y, Wang R, The heat transfer capability prediction of heat pipes based on capillary rise test of wicks. International Journal of Heat and Mass Transfer. 2021, 164; 120536. doi: 10.1016/j.ijheatmasstransfer.2020.120536

16. Meseguer J, P-rez−Grande I, Sanz−Andr-s, A. Heat pipes. Spacecraft Thermal Control. 2012, 175−207. Doi: 10.1533/9780857096081

17. Sandeep SS, Prakash SB. Design of heat pipe based on capillary and entrainment limitations. AIP Conference Proceedings. 2019, 2200(1). Doi: 10.1063/1.5141239

18. Mansour M, Heat Transport Limitations and Overall Heat Transfer Coefficient for a Heat Pipe. International Journal of Engineering and Advanced Technology (IJEAT). 2016 ,5(4); 119−23.

19. El−Genk, MS, Space nuclear reactor concepts for avoidance of a single point failure. Nuclear Energy and Design. 2008, 238; 2245-255.

20. Yuan Y, Shan JQ, Zhang B, Gou J, Bo Z, Lu T,Ge L, Yang Z. Accident analysis of heat pipe cooled and AMTEC conversion space reactor system. Annals of Nuclear Energy. 2016, 94; 706-71. doi: 10.1016/j.anucene.2016.04.017

21. Zhang Y, Guo K, Wang C, Tang S, Zhang D, Tian W, Su GH. Numerical analysis of segmented thermoelectric generators applied in the heat pipe cooled nuclear reactor. Applied Thermal Engineering. 2022, 204; 117949. Doi: 10.1016/j. applthermaleng.2021.117949

22. Peterson G. An overview of micro heat pipe research and development. Journal Applied Mechanics Review. 1992, 45; 175-189. doi: 10.1115/1.3119755

23. Karabulut K, Alnak DE. Investigation of heat transfer and flow properties in separated flow and reattachment regions for liquid sodium flow at fast reactors. Nuclear Engineering and Design. 2021, 379; 1-5. Doi: 10.1016/j. nucengdes.2021.111224

24. Faghri A, Zhang Y. Transport phenomena in multiphase systems. Elsevier, Burlington, MA, 2006, 1030.

25. Faghri A, Zhang Y, Howell J, Advanced heat and mass transfer. 1st ed., Global Digital Press, Columbia, MO, 2010, 934.

26. Ivanovskii MN, Sorokin VP, Yagodkin IV. The physical principles of heat pipes. Clarendon Press, Oxford, United Kingdom, 1982, 268.

27. Vargaftik NB. Handbook of physical properties of liquids and gases. Hemisphere, New York, NY, 1975, 758.

28. Chi W. Heat pipe theory and practice. Hemisphere Publishing Corporation, New York, 1976, 242.

29. Deng D, Liang D, Tang Y, Evaluation of capillary performance of sintered porous wicks for loop heat pipe. Experimental Thermal and Fluid Science. 2013, 50; 1−9. doi: 10.1016/j. expthermflusci.2013.04.014

30. Semenic T, Lin YY, Catton I, Thermophysical properties of biporous heat pipe evaporators, ASME Journal of Heat Transfer. 2008, 130; 022602. doi: 10.1115/1.2790020

31. Dominguez Espinosa FA, Peters TB, Brisson JG. Effect of fabrication parameters on the thermophysical properties of sintered wicks for heat pipe applications. International Journal of Heat Mass Transfer. 2012, 55; 7471−7486. doi: 10.1016/j.ijheatmasstransfer.2012.07.037

32. Busse CA. Theory of the ultimate transfer of cylindrical heat pipes. International Journal of Heat and Mass Transfer. 1973, 16; 169-186. Doi: 10.1016/0017−9310(73)90260−3

33. Ochterbeck JM, Heat pipes, Heat Transfer Handbook, 1st ed., 2003, 1481.

34. Williams RR, Harris DK, A device and technique to measure the heat transfer limit of a planar heat pipe wick. Experimental Thermal and Fluid Science. 2006, 3; 277−284. Doi: 10.1016/j. expthermflusci.2005.07.008

35. Holley B, Faghri A. Permeability and effective pore radius measurements for heat pipe and fuel cell applications. Applied Thermal Engineering. 2006, 26; 448−462. Doi: 10.1016/j. applthermaleng.2005.05.023.

36. Carnogurská M, P-íhoda M, Brestovi- T, Molínek J, Pyszko R. Determination of permeability and inertial resistance coefficient of filter inserts used in the cleaning of natural gas. Journal of Mechanical Science and Technology. 2012, 26; 103−111. Doi: 10.1007/s12206−011−0937−3.

Research Article
Hittite Journal of Science and Engineering, 2023, 10 (4) 287-299
ISSN NUMBER: 2148-4171
DOI: 10.17350/HJSE19030000318

Strontium Isotopes, Ostracod Fauna, and Paleoenvironmental Characteristics in the Late Miocene Sequence of the Mut/Dağpazarı Region, Southern Turkey

Umit Safak* **Hande Sonsun** **Nusret Nurlu**
Cukurova University, Department of Geological Engineering, Adana, Türkiye

Article History:
Received: 2023/02/18
Accepted: 2023/11/29
Online: 2023/12/31

***Correspondence to**: Ümit Şafak,*
E-mail: usafak01@gmail.com;
Phone: +05433980699

This article has been checked for similarity.

ABSTRACT

The primary focus of this study was the Dağpazarı village in the Mut region of Mersin, southern Turkey. In this research area, two stratigraphic sections were meticulously measured. The study conducted a comprehensive examination of the Middle-Late Miocene period in the Dağpazarı, Ballı, and Mut Formations by analyzing the ostracod fauna and utilizing strontium isotope chemostratigraphic dating. This research determined that the upper levels of the Mut/Köselerli formations, specifically from the Burdigalian to Serravallian, signify the commencement of the Miocene succession in the study area.The Dağpazarı Formation, characterized by abundant silty-clay, Ostrea fossils, and lignite layers, is deposited unconformably just above these levels.This formation contains the following ostracod taxa; *Bairdia subdeltoidea, C. glypta, Cytheridea acuminata acuminata, Acanthocythereis hystrix, Krithe monosteracensis, Neomonoceratina mouliana, Hemicyprideis sp., Cistacythereis caelatura, Cyherella terguemi, T. prava, K. langhiana, A. ulicznyi, Pokornyella deformis minor, Loxoconcha alata, Tenedocythere salebrosa.* Furthermore, the planktonic foraminifera species are; *O. universa, Globigerinoides trilobus, Glb. ruber, Orbulina bilobata, Glb. sacculifer, O. suturalis*, and the formation includes abundant bryozoa, echinoid spines, gastropods such as Terebralia at distinct levels, and fish otolith. The formation, dating from the late Serravallian to the early Tortonian, exhibits the shallow reef characteristics that continued to develop in the late Miocene.The formation consists of dark green, bulbous weathered claystone, *Bairdia subdeltoidea* and *Ostrea* which are reduced in size at the levels that pass into hard clayey sandstone, abundant benthic foraminifera with abundant echinoid spines. The formation consists of benthic foraminifera, hard clayey sandstone, and weathered dark green claystone, which contains numerous echinoid spines.*Ostrea* and *Bairdia subdeltoidea* are also present. The upper section of the analyzed succession concludes with silty, compact, clayey limestone layers and light-colored limestone bands. The Tırtar Ballı Formation, which conformably overlays the Dağpazarı Formation, signifies the culmination of a relatively recent reef formation during the Tortonian period.Ostracod species such as *Aurila pigadiana, Thalmannia hodgii, Buntonia sublatissima dertonensis, Bairdia subdeltoidea, Aurila sp. Bassiouni* have been defined. The limestones also contain abundant benthic foraminifera and echinoid spines. The $^{87}Sr/^{86}Sr$ ratio analyzed from the carbonate sample obtained from the Dağpazarı formation is 0.708920. Based on these isotope data, the age of the Dağpazarı formation was calculated to be 8.7 million years (Ma).

Keywords:
Mut; Dağpazarı; Planktonic foraminifera; Strontium isotope; Ostracod

INTRODUCTION

The study area is situated in the northern part of the town center of Mut, within the Central Taurus Mountains (Fig. 1). In the initial geological investigations conducted in the research area and its vicinity, particular emphasis was placed on studying the structural evolution of the region since the Paleozoic, mapping the rock formations, and analyzing tectono-stratigraphic developments. Following this, numerous researchers conducted comprehensive studies in the fields of general geology, paleontology,

Cite as:
U. SAFAK, H. SONSUN and N. NURLU, "Strontium Isotopes, Ostracod Fauna, and Paleoenvironmental Characteristics in the Late Miocene Sequence of the Mut/Dağpazarı Region, Southern Turkey" Hittite Journal of Science and Engineering, vol. 10, no. 4, pp. 287–299, 2023. doi:10.17350/hjse19030000318

and stratigraphy [1-23]; [24-33]. Economic geology studies have predominantly focused on oil and coal [34-35]. Furthermore, there has been a significant increase in studies related to carbonate precipitation in Neogene rocks. This research was conducted to provide a comprehensive analysis of the Neogene sediments exposed in the Dağpazarı area, with a primary focus on ostracod fauna. In the Mut Basin, situated in the Middle Taurus Belt, calcareous nannofossil biochronology has been documented in the Mut-Ermenek section, specifically in the Dağpazarı reef. This reef developed as a result of the Miocene marine transgression and is primarily found in the upper sections of the reef, known as the Dağpazarı Formation. Coral biofacies were identified by Gürler [22] ,and Ilgar et al. [137] documented the late Serravallian to early Tortonian dug valley fill sediments, known as the Dağpazarı Formation [33-23]. The main objective of this study was to conduct a comprehensive analysis, including stratigraphic, chemostratigraphic (Sr isotopic), and micropaleontological examinations, with a specific focus on ostracod fauna. The research highlights the relatively recent reef sediments found in the Dağpazarı Formation, which is the primary subject of this study, as well as the overlying Tırtar/Ballı Formation.

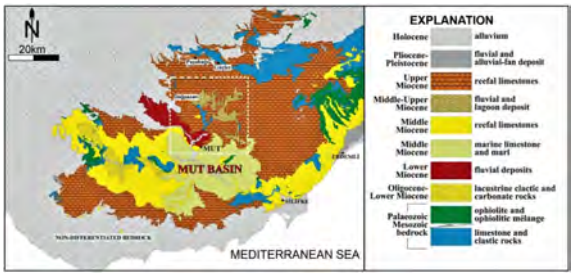

Figure 1. Geological map of the Dağpazarı research area and its vicinity [23].

The ostracod assemblages from the Late Miocene (Tortonian) in this research were examined and compared with ostracod faunas from Late Miocene (Tortonian) studies conducted in other regions of the Eastern Mediterranean in Turkey. Additionally, isotope data reported from nearby areas were analyzed in conjunction with the data obtained in this study. Ostracod assemblages from the Tortonian period in these Eastern Mediterranean-origin basins, namely Antalya/Serik, Mut, Mut/Dağpazarı, Karaman, Silifke-Erdemli/Mersin, Adana, and Antakya basins, were compared with the ostracod assemblage in this study. It was observed that they shared similar species. This study elucidates the formation of a young reef during the Tortonian period in the Adana Basin (Kuzgun Formation) [36], as well as in Silifke-Erdemli (Sarıaydın Formation) [37]. Similar depositional conditions and young reef characteristics were also identified in the Antakya Basin (Nurzeytin Formation) [38-39] (Fig. 8).

MATERIAL AND METHODS

Paleontological Analysis

The research was carried out on the 1/25000 scaled Mersin O30b3 map sheet. Measured sections were taken from two different areas in Dağpazarı Village and 50 washing samples were collected for micropaleontological analyses. The laboratory washing method was performed to obtain the ostracod fauna. 150 grams of each of the hard and moderately soft samples obtained from the sections were taken and divided into small pieces by placing them between thick paper and hitting them with a hammer Crumbled samples were placed in 1-liter glass beakers and hot water and 15% diluted hydrogen peroxide (H_2O_2) were added to disintegrate and left for 24 hours to dissolve. The samples have been washed under pressurized water with a set of 60, 120, 230 mesh sieves and then dried in an oven and put into separate bags according to their sieve numbers. After the separation of the microfossils contained in the samples from the grains, the genus and species of the samples collected in the collection slides were determined. 28 ostracod genera and 44 taxa have been defined in the research.

Identified species and genera have been counted, lateral and vertical distribution of ostracods have been enumerated and their numerical abundances have been defined. Symbols describing the semiquantitative frequency of ostracodes are used in this distribution table. Very rare (1-2 cover) ve rare (3-5 cover) frequencies are denoted by symbols such as r + and ○, common (6-15 cover), frequent (16- 25 cover) and very frequent (>25 cover) and frequencies ●,□,■. Paleoenvironmental interpretation of the research area was conducted based on the statistical and relative data. This interpretation was carried out in accordance with previous works by Morkhoven [110], Doruk [111], Bassiouni [112], and Freels [40-43]. Plate 1-2 was created by choosing scanning electron microscope (SEM) images of specific ostracod species and genera that were identified in these studies.

Petrographical and Isotopical Analyses

Thin sections of the samples were analyzed using binocular microscopes under polarized light (Leica DMEP). Subsequently, these thin sections were further examined using an optical microscope that utilized both transmitted and reflected light.Two of the most commonly utilized classifications are those developed by Folk and Dunham [44-45,46]. The thin sections of the limestones from the Divlek and Maz Formations were prepared by the Department of Geological Engineering at Çukurova University. The petrographic examination was conducted using the Leica DMEP microscope at Çukurova University. Strontium isotope geochemistry experiments were carried out at the Radiogenic Isotope Laboratory, R & D Training, and Mea-

surement Center of METU (Sr Isotope Ratio Analysis Experimental Instruction), following the detailed procedures and conditions outlined by Köksal et al. [47]. The isotope analyses were conducted by METU and involved using ultrapure water and chemicals. Weighing, chemical dissolution, and chromatographic operations were performed in a clean laboratory setting that met class 100 cleanroom standards. Specifically, certain sedimentary (limestone) samples underwent $^{87}Sr/^{86}Sr$ isotopic analyses at the METU Central Laboratory's Radiogenic Isotope Laboratory in Ankara, following the analytical techniques outlined by Köksal and Göncüoğlu [48].

RESULTS

Stratigraphy

The Miocene units in the research region can be listed from bottom to top as follows: Langhian-Serravallian Mut Formation, late Serravalian-early Tortonian Dağpazarı Formation, and Tortonian Tırtar/Ballı Formation (Fig. 2).

Lithostratigraphy

Mut Formation

The Mut Formation was initially named by Sezer [119], and later Gedik et al. [34] also used this name [49, 34]. The reefal Mut Formation can be correlated with the following formations: Silifke Formation [27], Göktepe Reef Limestone Member defined around Ermenek-Karaman [11], Mut Formation around Ermenek [50], and Karaisalı Formation in the Adana Basin [51]. The Mut Formation is characterized by reefal limestone and is found at the base of the succession in a relatively low thickness in this study. The age of the formation has been defined by different researchers as late Burdigalian-Langhian [23], Langhian-Serravalian [28-30,17], Middle Miocene [19-21], and late Serravallian-Tortonian [22]. When analyzing the age of the Mut Formation based on the age given by the overlying unit in this study, it is reported as Burdigalian-Serravalian (Fig. 3).

Dağpazarı Formation

The Dağpazarı Formation was initially defined by Atabey et al. [87], while Gedik et al. [34] referred to it as the Köselerli Formation [17,34]. This formation begins with silt, clay, and clayey limestone, and includes ostreal silty and sandy layers, greenish claystone with vegetation, and lignite. Towards the upper part of the succession, there is a lithological transition to fossiliferous sandstones and hard clayey sandstones (Fig. 2).

The age of the Dağpazarı Formation has been previously reported as Serravallian [17] and late Serravallian-Tortonian [23]. In this study, the age of the formation was determined as late Serravallian-early Tortonian, primarily based on the ostracod content and supported by strontium isotope data.

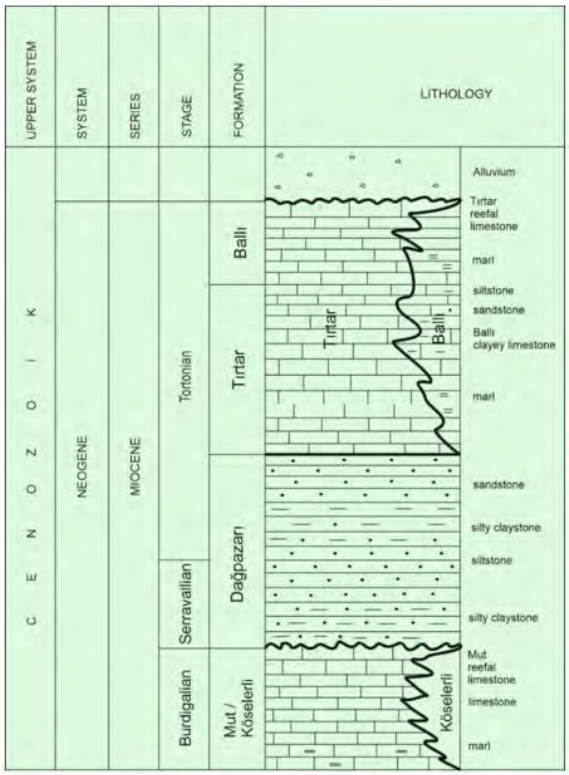

Figure 2. Generalized stratigraphic section of the research region of Dağpazarı [47].

Figure 3. a. General view of the outcrops of Mut formation (view to north) b-c. General outcrop of Dağpazarı formation and clayey limestone.

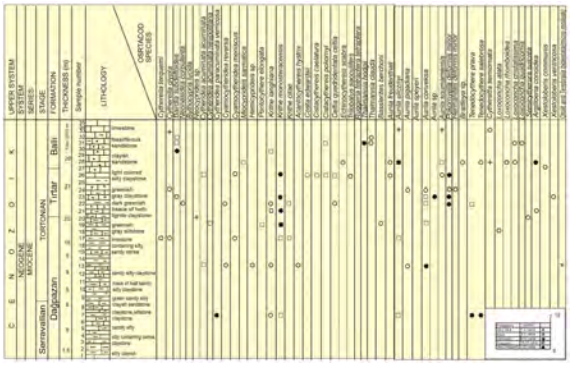

Figure 4. The distribution of the ostracod species in the Dağpazar 1 measured stratigraphic section.

Tırtar Formation

The Tırtar Formation was initially named by Atabey et al. [87]. This unit is characterized by limestone as the predominant lithology and contains algae, corals, benthic foraminifers, and mollusks [17]. Atabey et al. [87] and Ilgar et al. [93] proposed the age of the formation as Tortonian (Fig. 2) [17,34]. In this study, a predominant consideration of ostracod content and strontium isotope data led to the determination of the formation's age as Tortonian.

Ballı Formation

Atabey et al. [87] the unit was named for the first time and this name was given because the type section location is in the village of Ballı [17]. Planktonic foraminifera and nannoplanktons have been defined in the formation where claystone, marl and clayey limestone form the dominant lithology (Fig.2). Atabey et al. [87] found Globigerinoides obliquus extremus in the unit [17]. In addition, Ilgar et al. [93] suggested the age of the formation as Tortonian [23]. In this study, when the ostracod content and strontium isotope data are evaluated predominantly, the age of the formation is considered as Tortonian.

Measured Stratigraphic Sections

Stratigraphic sections were measured from two distinct ridges by selecting strategic locations within the research area. These locations offered the best exposure of successions providing Late Miocene age information in the Dağpazarı region.

Dağpazarı I Measured Stratigraphy Section

The section was measured between coordinates X1: 36.829371, Y1: 33.464047, Z1: 1287 m, and X2: 36.828976, Y2: 33.464154, Z2: 1492 m, with a total thickness of 205 meters. The section begins at the base with ostreid-rich, clayey, and silty layers belonging to the Dağpazarı Formation. As we move upwards, it transitions into weathered, greenish-gray claystone, silty clay, and fossiliferous clay-siltstone layers. Above this, the Tırtar/Ballı Formation is found, showing a smooth transition. The upper part of the succession is characterized by clayey sandstone, fossiliferous clayey sandstone, which remains relatively intact. This formation characterizes a reef in unweathered silty, clayey limestone (Tırtar) and upwardly unweathered limestone (Ballı) lithology. The following ostracod taxa were reported at the base levels of the Dağpazarı Formation in the section: *Cytherella terguemi, Cytheridea acuminata acuminata, Cytheridea acuminata verrucosa, Krithe monosteracensis, Krithe langhiana, Aurila ulicznyi, Cytherella glypta, Cytheridea acuminata neapolitana, Miocyprideis sarmatica, Hemicyprideis sp., Krithe monosteracensis, Krithe citae, Aurila convexa, Ruggieria tetraptera tetraptera, Aurila soummamensis, Tenedocythere salebrosa, Pokornyella deformis minor, Tenedocythere prava, Echinocythereis scabra.* In the upper levels, *Bairdia subdeltoidea, Thalmannia hodgii, Thalmannia clauda, Aurila soummamensis,* and *Aurila ulicznyi* were identified in the middle level of the formation. At the bottom levels, gastropods like Terebralia and fish otoliths were found. It's also notable that there is an increase in shallowing, and lagoonal conditions seem to dominate the environment.The ostracod genera identified in this formation generally suggest an epineritic environment, including *Ruggieria, Tenedocythere, Cytheretta, Aurila,* and *Pokornyella.* Additionally, ostracod species that typically indicate infraneritic environments, like *Krithe, Echinocythereis*, and *Buntonia*, have also been reported. The presence of ostracod species characterizing lagoon-littoral environments suggests a transitional feature from very shallow marine conditions to partially deep-sea conditions, including species like *Hemicyprideis, Loxoconcha*, and *Loxocorniculum*.Hence, it can be concluded that there is data indicating the presence of reef front and back textures in the Late Miocene (Tortonian) sequence. Shallow-water (epineritic depth) ostracod species like *Bairdia subdeltoidea, Aurila ulicznyi,* and *Aurila soummamensis* symbolize the reef's back and roof within the clay layers between the limestone beds of the Tırtar/Ballı Formation.

In the stratigraphic section, the Tırtar/Ballı Formation contains a wealth of b*ryozoa, echinoid spines,* and *gastropods*, including Terebralia, which is also observed at various levels within the section.

Dağpazarı II Measured Stratigraphy Section

The section was measured between coordinates X1: 36.826641, Y1:33.460034, Z1:1315 m., and X2: 36.826871, Y2:33.461080, Z2:1420 m. The section has a total thickness of 135 m and consists of cream-colored clayey limestone, clayey limestone-sandstone alternation, and sandstone belonging to the Dağpazarı Formation, which are observed at the lower, middle, and upper levels of the succession.The Dağpazarı Formation is succeeded by the reefal Tırtar/Ballı Formation, which consists of claystone, hard clayey limestone, and hard limestone, conformably overlaying it (Fig.5).

The ostracod species observed at the base levels of the Dağpazarı Formation in the section include *Cytherella glypta, Neonesidea corpulenta, Bairdoppilata supradentata, Neomonoceratina mouliana, Ruggieria tetraptera tetraptera, Aurila convexa, Aurila albicans, Aurila soummamensis, Aurila woodwardii.* Planktonic foraminifera species reported at the base of the section comprise *Trilobatus sacculifers, Orbulina suturalis, Morozovella angulosa.* Planktonic foraminifera species identified in the middle and upper levels include *Cytherella terquemi, Aurila sp.* Additionally, ostracoda species such as *Globigerinoides ruber, Orbulina bilobata, Orbulina suturalis, Orbulina universa* have been reported.The ostracod species identified in the claystone and clayey limestone levels of the Tırtar/Ballı Formation include *Aurila convexa, Krithe langhiana, Pokornyella deformis minor, Ruggieria tetraptera tetraptera, Acanthocythereis hystrix, Aurila speyeri, Aurila soummamensis, Aurila ducasseae, Tenedocythere mediterranea, Loxoconcha tumida, Argilloecia conoidea* (Fig.5). This assemblage characterizes the reef lagoon and the core of a young reef, indicating that the section is influenced by lagoon-littoral conditions as well as the neritic marine environment.

Strontium Isotope Chemostratigraphy

Strontium isotope chemostratigraphy plays a crucial role in deciphering the Earth's geological history. The $^{87}Sr/^{86}Sr$ pattern in seawater can be employed for robust correlations when other chemostratigraphic, lithostratigraphic, or biostratigraphic indicators prove to be inadequate.The accuracy of reconstructing seawater strontium isotopes depends significantly on two factors: the quality and reliability of chronological control in the reference data and the preservation of the samples, both of which can vary with the age of the period under examination.

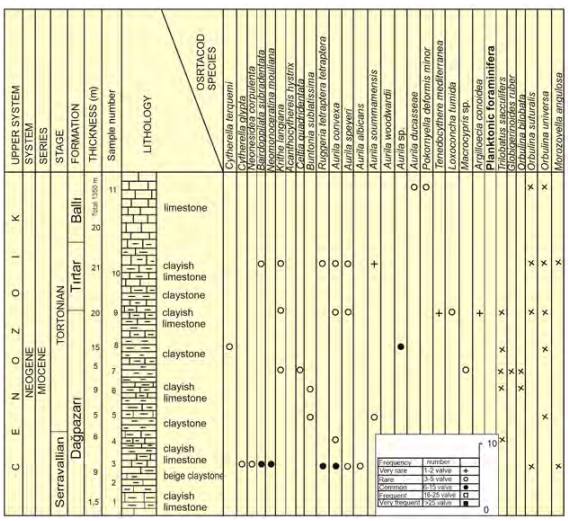

Figure 5. The distribution of the ostracod species in the Dağpazar 2 measured section

Marine strontium ratios ($^{87}Sr/^{86}Sr$) have evolved over the Earth's history, primarily driven by the interplay between unradiogenic strontium sourced from the Earth's mantle and radiogenic strontium from terrestrial input (continental crust) [54-55], as illustrated in Fig. 6 [52-53].

Three samples (Dp-1; 0,708920±15, Dp-2; 0,709644±8, Dp-3; 0,709733±7) were gathered from the studied area in order to analyze strontium and two of these samples did not yield results due to effects such as contamination and diagenesis. The ratio of $^{87}Sr/^{86}Sr$ analyzed from the limestone sample collected from the Dağpazarı formation is 0.708920. The age of the Dağpazarı formation was estimated as 8.7 Ma based on these isotope data.

DISCUSSION

Ostracod fauna-based correlation of Late Miocene (Tortonian) lithostratigraphic units of the study area with other Late Miocene (Tortonian) lithostratigraphic units in the Eastern Mediterranean region of Turkey is depicted in Fig. 7.

Antalya (Serik), Karpuzçay Formation

Karpuzçay formation was first named and reported by Akay et al. [57]. The type locality of the formation is Karpuzçay Village in the Antalya Miocene Basin. This formation comprises siltstone, thin-bedded sandstone, and sandy limestone alternations. The ostracod assemblage identified in the formation includes *Bairdia subdeltoidea, Miocyprideis sarmatica*, and *Aurila soummamensis* [57-58] (Fig.8).

Dağpazarı/Mut, Dağpazarı and Tırtar/Ballı Formations

The Dağpazarı/Mut, Dağpazarı, and Tırtar/Ballı formations were initially named by Atabey et al. [17]. The Dağpazarı Formation is characterized by clayey, weathered, greenish-gray siltstone at its base, which transitions into ostreal-bearing clayey siltstone, and further up

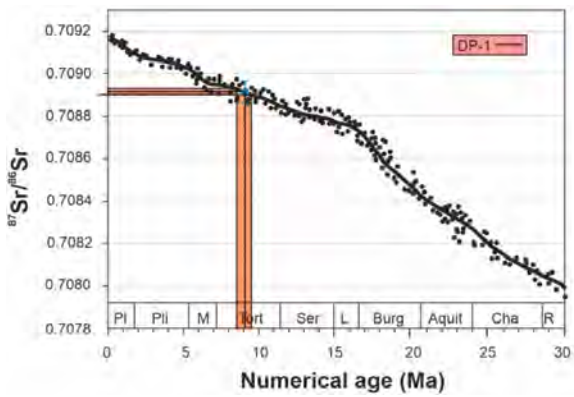

Figure 6. Strontium isotope variation curve for the Miocene interval [56].

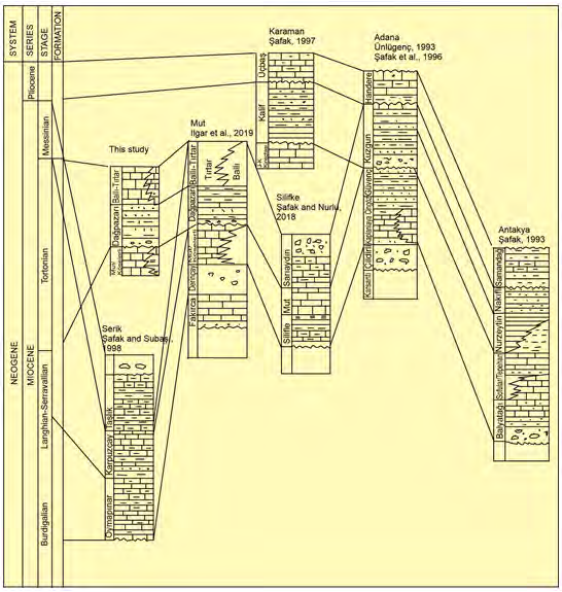

Figure 7. Correlation of Miocene-Pliocene Formations deposited in Antakya, Mut, Karaman, Silifke-Erdemli, Adana, Antakya basins (Eastern Mediterranean)

the succession, cream-colored clayey limestone, clayey limestone-sandstone alternations, and sandstones are present.The ostracod assemblage in the Dağpazarı Formation includes the following species: *Bairdia subdeltoidea, Hemicyprideis sp., Acanthocythereis hystrix, Aurila soummamensis, Pokornyella deformis minor, Ruggieria tetraptera tetraptera, Loxoconcha tumida,* and *Xestoleberis glabrescens* [23]. The formation has been assigned a middle (Serravallian) age [17] and a middle-late Miocene age (late Serravalian-Early Tortonian) [23]. The Tırtar Formation is primarily composed of light-colored, silty, hard clayey limestone. It exhibits both lateral and vertical transitions with the Ballı Formation [17,23]. These formations are dated to the Tortonian age [17,23], as shown in Fig. 8.

Kalif (Karaman) Formation

The Kalif (Karaman) Formation was initially defined by Koçyiğit in [129], based on the unit exposed in and around Karaman [59]. The formation's type locality, as first investigated by Koçyiğit in 1978, is best observed in Karaman Province and its surrounding areas [59]. The Kalif (Karaman) Formation comprises fossiliferous clayey limestone, sandy limestone, marl, mudstone shale, and evaporite layers. The ostracod assemblage in this formation is diverse and includes many species, listed as follows: *Neomonoceratina interiecta, N. acupicta, Sylvestra posterobursa, Cyprideis seminulum, C. sohni, Cytheridea acuminata acuminata, Chrysocythere paradisus, Krithe monosteracensis, Loxoconcha cristatissima,* and *Xestoleberis ventricosa.* The formation is assigned a late Miocene age [60] (Fig. 8).

Sarıaydın (Silifke-Erdemli/Mersin) Reef Limestone

The Sarıaydın Formation, also known as Sarıaydın Reef Limestone, was originally described by Gökten [97] based on exposures in Sarıaydın Village [27]. The formation's type locality is in Sarıaydın Village. It primarily consists of cream-colored limestone interbedded with clay sediments, marl, and caliche [37]. The ostracod assemblage

	bu bilgisayar konumuna kaydedildi						
Serik/Antalya Şafak ve Subaşı (1998)	Karaman Şafak(1997)	Dağpazarı Ilgar et al. (2019)	Mut/Mersin This study	Silifke-Erdemli MERSİN Şafak and Nurlu (2018)	Adana Basin Ünlügenç(1993) Şafak(1996)	Antakya Şafak(1993)	Ostracod species identified in the Eastern Mediterranean Tortonian
	×			×	×		*Cytherella vandenboldi*
					×		*Cytherella vulgata*
					×		*Cytherella obulus*
	×		×		×		*Cytherella glypta*
					×		*Cytherelloidea variopunctata*
							Cytherella petrosa
						×	*Cytherella postdenticulata*
				×			*Cytherella creutzburgi*
				×			*Cytherella sordida*
			×	×			*Cytherella terquemi*
×	×	×	×		×		*Bairdia subdeltoidea*
	×		×	×	×		*Neonesidea corpulenta*
						×	*Bairdia mediterranea*
			×	×			*Bairdoppilata subradentata*
				×			*Neomonoceratina interiecta*
	×			×			*Neomonoceratina acupicta*
	×						*Neomonoceratina iaskaravi*
	×		×		×	×	*Neomonoceratina moulana*
				×	×		*Sohnieidrella dromas*
	×					×	*Leptacythere multipunctata*
			×				*Cyprideis torosa*
				×		×	*Cyprideis anatolica*
				×		×	*Cyprideis sohni*
	×			×	×		*Cyprideis pannonica*
	×			×	×		*Cyprideis seminulum*
×			×	×	×		*Miocyprideis sarmatica*
	×		×	×	×		*Cytheridea acuminata acuminata*
	×		×	×	×		*Cytheridea acuminata neapolitana*
						×	*Sylvestra posterobursa*
	×		×	×		×	*Cyamocytheridea reversa*
	×				×	×	*Cyamocytheridea obstipa*
	×		×		×	×	*Cyamocytheridea meniscus*
	×					×	*Cyamocytheridea polygona*
						×	*Cyamocytheridea deveva*
		×	×				*Hemicyprideis sp.*
	×		×			×	*Pontocythere elongata*
	×		×				*Krithe citae*
	×		×	×		×	*Krithe monosteracensis*
			×				*Krithe langhiana*
					×	×	*Krithe papillosa*
				×			*Parakrithe robusta*
	×	×	×		×		*Acanthocythereis hystrix*
	×		×		×	×	*Costa edwardsii*
				×			*Costa fricoslate*
	×				×	×	*Chrysocythereis paradisus*
	×		×	×	×		*Clatacythereis pokornyi*
			×	×		×	*Clatacythereis caelatura*
	×				×		*Cerinocythereis antiquata*
	×		×		×		*Cellia quadridentata*
	×		×				*Echinocythereis scabra*
	×				×		*Incongruellina rotundata*
	×	×	×		×		*Ruggieria tetraptera tetraptera*
	×		×		×		*Thalmannia hodgii*
					×	×	*Thalmannia procera*
					×		*Thalmannia dolabrata*
	×					×	*Heterocythereis albomaculeta*
×		×	×	×			*Aurila soummamensis*
	×		×		×	×	*Aurila speyeri*
	×		×		×	×	*Aurila convexa*
	×		×		×		*Aurila freudenthali*
	×		×				*Aurila uliczniyi*
					×	×	*Aurila skalae*
			×		×	×	*Aurila ducasseae*
						×	*Aurila cicatricosa*
			×		×	×	*Aurila albicans*
	×	×	×	×	×	×	*Pokornyella deformis minor*
	×				×		*Procytherеis sulcatopunctatus*
	×		×		×	×	*Hermanites haidingeri minor*
	×		×		×	×	*Tenedocythere mediterranea*
	×		×		×	×	*Tenedocythere prava*
	×		×		×	×	*Tenedocythere salebrosa*
	×			×	×	×	*Urocythereis favosa(Nonucythereis)*
	×					×	*Urocythereis seminulum*
						×	*Bosquetina carinella*
						×	*Occultocythereis bireticulata*
					×		*Cytherella orthozensis*
	×		×		×		*Cytheretta semiovata*
				×			*Cytheretta simplex*
			×		×	×	*Loxoconcha rhomboidea*
	×	×	×	×			*Loxoconcha tumida*
	×				×		*Loxoconcha subovata*
	×		×				*Loxoconcha cristatissima*
	×				×		*Loxoconcha stellifera*
				×			*Loxoconcha alata*
			×	×		×	*Xestoleberis communis*
	×			×	×		*Xestoleberis reymenti*
	×		×	×	×		*Xestoleberis ventricosa*
		×			×	×	*Xestoleberis glabrescens*
	×		×				*Loxocorniculum quadricornis*
	×	×			×	×	*Paracypris polita*
			×				*Semicytherura sulcata*
	×		×				*Argilloecia conoidea*

Figure 8. Ostracod species identified in the Eastern Mediterranean Late Miocene

within this formation includes the following genera and species: *Cytherella vandenboldi, C. creutzburgi, C. sordida, C. seminulum, Neomonoceratina acupicta, N. interiecta, Miocyprideis sarmatica, Parakrithe robusta, Cyprideis anatolica, Krithe monosteracensis, C. pannonica, Cytheridea acuminata acuminata, Cistacythereis pokornyi, C. caelatura, Loxoconcha tumida,* and *Paracypris polita*. The age of the Sarıaydın Formation was given as Tortonian? [27] (Gökten, [97]) and Late Serravallian-Tortonian [37], (Fig.8).

Kuzgun (Adana) Formation

The Formation (Adana) Formation was originally defined by Schmidt [51], and its type locality is situated in Kuzgun Village along the Adana-Karaisalı road. This formation is characterized by a transition from meandering river sediments at the base to shallow marine conditions in the upper levels. During the Tortonian, the region experienced sea level fluctuations, with alternating rises and falls [61]. Within this formation, you can find substantial fossiliferous greenish claystone, light-colored clayey limestone, and well-sorted yellowish-cream colored sandstones with a reefal character, particularly at the İncirlik locality, situated to the southeast of Adana [36]. The ostracod community in this formation is exceptionally diverse, including the following species: C*ytherella vulgata, C. glypta, Neomonoceratina mouliana, Schneidrella dromas, Cyamocytheridea meniscus, Carinocythereis antiquata antiquata, Aurila soummamensis, Loxoconcha rhomboidea, Paracypris polita*. The formation is attributed to the Tortonian age [36,61-62].

Nurzeytin (Antakya Basin) Formation

The Nurzeytin Formation in the Antakya Basin was initially designated by Selçuk in [63]. The type locality is situated in the vicinity of Nurzeytin, Yazır, Sivrikavak, and Babatorun. This formation is characterized by reef-like lithologies including sandstone, clayey limestone, marl, and claystone. The ostracod assemblage in this formation is highly diverse, and the following taxa have been identified: *Cytherella glypta, Cyprideis torosa, Acathocythereis hystrix, Aurila convexa, A. speyeri, Hermanites haidingeri minor, Ruggieria tetraptera tetraptera, Tenedocythere prava, T. mediterranea, Xestoleberis ventricosa, X. communis.* The formation has been suggested to span the Late Serravalian-Tortonian and Tortonian ages [38-39,63].From these descriptions, it's clear that the Tortonian development in these six significant locations in the Eastern Mediterranean Region of Anatolia is remarkably similar in terms of lithology, environmental conditions, and ostracod fauna.The ostracod fauna of the Dağpazarı Formation in this new study closely resembles the ostracod species identified from these six locations, with the exception of *Cyprideis* species, which were not encountered in this study.The environment exhibits distinct back-reef facies characteristics with lagoon-like *Neocyprideis* and lagoon-litoral ostracod species like *Hemicyprideis* and *Loxoconcha*. It also displays distinct shallow reef front and core characteristics with ostracod genera adapted to epineritic depths, such as *Acanthocythereis, Aurila, Pokornyella, Tenedocythere, Neomonoceratina, Pontocythere,* and *Ruggieria*. Furthermore, ostracod genera indicative of infraneritic depths and bathyal environments, such as *Macrocypris, Argilloecia, Bythocypris, Krithe,* and *Bradleya*, are typical of deep reef front facies (Fig. 7).The Mut Basin is situated in the Eastern Mediterranean region of the Alpine-Himalayan Mountain Belt (AHMB) and in the Central Taurus sector of the Taurus Mountains in southern Turkey.

The late Burdigalian marine transgression led to the submersion of the Antalya, Mut, and Adana basins, initiating the deposition of the first marine sediments in these basins during the Neogene. Consequently, the Burdigalian-Serravallian period witnessed the formation of the reefal limestones of the Mut Formation and the marl-clay limestones of the Köselerli Formation in the Mut Basin. As a result of the decrease in sea level in the Late Serravallian, the basin started to become shallow and a young reef deposition took place on the Mut formation reef limestones in the Late Serravallian-early Tortonian. This unit is the Dağpazarı Formation, and the reef limestones of the Tırtar Formation and the layered limestones of the Ballı Formation were deposited on the unit in the north of the Mut Basin. In the vicinity of Dağpazarı Village, the sedimentary layers consisting of mudstone, silty claystone, and sandstone that overlay the Mut Formation were initially considered part of the Köselerli Formation and examined. However, due to variations in lithology, deposition environment, and age, these layers were later designated as the Sertavul Formation.The formation typically represents a lagoon environment situated behind the reef. It is occasionally associated with fluvial deposits, coastal sand, coal seams, and limestone deposits. This rock unit has been identified as the Dağpazarı Formation, indicating its characteristics of a back-reef lagoon and alluvial fan environment. [17]. It was also stated by these authors that the Dağpazarı formation is transitional with the Köselerli and Mut formations deposited in the completely regressive phase of the sea. Early-middle Miocene sea level changes in the Mut Basin have also been studied, but clear data are not available [20, 22].

It is detailed that an incised valley, formed as a result of the late Serravallian eustatic sea-level decline, is observed, where the Dağpazarı Formation overlies the Mut reefal limestones with erosive unconformity [23]. It is mentioned that the sedimentary facies identified in the formation were deposited within this valley, following a subsequent relative

sea-level rise that occurred in the early Tortonian. A comprehensive study of planktonic foraminifera was conducted using mudstone and marl samples obtained from the Dağpazarı and Ballı Formations.

The study employed Mediterranean planktonic foraminiferal biostratigraphy and the ATNT52004 magnetic chronostratigraphy table to determine the Serravallian and Tortonian ages.It was also noted that due to the isostatic uplift of the Taurus Mountains in the late Tortonian, marine sedimentation in the Mut Basin ceased, leading to the exposure of the basin [65-67]. In this research, the fossil content of the unconformable Dağpazarı Formation overlying the Mut limestones at the base and the Tırtar/Ballı Formations, based on the ostracod fauna, was documented.These three lithological units (Dağpazarı, Tırtar/Ballı Formations) have developed with a young reef character and contain ostracod genera and species that accurately represent the back-reef-lagoon, core, and fore-reef facies.

In this new study, the Dağpazarı Formation exhibits a lagoon character with ostracod species like *Neocyprideis*, while the back reef is characterized by ostracod species such as *Hemicyprideis* and *Loxoconcha*, displaying lagoon-littoral characteristics. Additionally, the shallow reef fore-core is marked by ostracod genera with epineritic depth, including *Acanthocythereis, Aurila, Pokornyella, Tenedocythere, Neomonoceratina, Pontocythere*, and *Ruggieria*. The deep reef front is identified by ostracod genera with infraneritic depth, including *Macrocypris, Argilloecia, Bythocypris, Krithe*, and *Bradleya*. Additionally, this study identified significant genera indicative of lagoon sediments and marine input. [23].

The study notably provided a comprehensive presentation of the ostracod genera and species specific to the fore-reef facies, marking the first such detailed account in this research. Additionally, banded levels of Ostrea were identified in the littoral sections of the middle levels of the Dağpazarı Formation.The presence of the genus Ostrea is recognized as an indicator of shallowing in the environment [68-69]. This study was conducted in a succession characterized by the deposition of a young reef, which culminated in the Tortonian age in the northern part of the Mut Basin.

CONCLUSIONS

This study was conducted in and around Dağpazarı Village, located to the north of the Mut Basin. The research area includes sandy, clayey, silty, fossiliferous, and relatively younger sequences that overlay the Mut limestones (Mut Formation).The fossil content of the Dağpazarı, Tırtar/Ballı formations, which are very thin and unconformably emplaced on the Mut formation, has been revealed by predominantly using the ostracod assemblage and strontium isotopic data. Within this assemblage, ostracod genera indicative of a deepening neritic environment with a shallow neritic core, along with a litoral reef next to a lagoon, have been identified. This reefal succession, which originated during the Tortonian, has been investigated from lithological, chronostratigraphic, and chemostratigraphic perspectives. Furthermore, the ostracod assemblages from late Miocene (Tortonian) studies within the Eastern Mediterranean bioprovince of Turkey were also compared. In the lithostratigraphic and chronostratigraphic correlation from west to east, it was observed that the ostracod assemblages in the Tortonian of the Antalya, Mut, Karaman, Silifke-Erdemli, Adana, and Antakya basins closely resemble the ostracod assemblages found in the Tortonian of the Dağpazarı region.

Late Miocene reef-like sedimentary deposits with young reef characteristics were identified in the Late Tortonian (Miocene) successions within the Antalya, Dağpazarı/Mut, Karaman, Silifke-Erdemli, and Adana Basins, which are part of the Turkey-Eastern Mediterranean Province.

The ostracod assemblage has confirmed that the late Miocene (Tortonian) sediments in the Antakya Basin exhibit a shallow reefal character, characterized by creamy-white clayey units and marls. The $^{87}Sr/^{86}Sr$ ratio obtained from the carbonate sample within the Dağpazarı Formation is 0.708920. Based on this isotope data, the age of the Dağpazarı Formation has been calculated as 8.7 million years (Ma).

ACKNOWLEDGEMENT

Financial support for this research was generously provided by the Çukurova University Research Foundation under Project No: FBA-2021-13446. We would like to express our gratitude to two anonymous reviewers for their valuable comments, which have greatly improved this paper. We extend our thanks to Dr. Köksal for conducting the strontium isotopic analyses..

CONFLICT OF INTEREST

Authors approve that to the best of their knowledge, there is not any conflict of interest or common interest with an institution/organization or a person that may affect the review process of the paper.

AUTHOR CONTRIBUTION

The authors shared all the roles and contributed equally to the paper.

REFERENCES

1. Blumenthal, M.M., Niğde ve Adana vilâyetleri dahilinde Torosların jeolojisine umumi bakış. Maden Tetkik Arama Enat., Ankara, No 8, 48 s., 1941.
2. Blumenthall, M., Schichtfolge und Bauder Taurusketten im Hinterland Von Bozkır: Rev. Fak. Sc. Üniv., İstanbul, Serie B,t. lX, fasc., 2, 1944.
3. Blumenthal, M., Recherces géologiques dansle Taurus occidental dans l'arriere-pays d'Alanya. MTA Enst. Yay. Seri D., No: 5, 134 s., 1951.
4. Blumenthal, M., Géologie des Hohen Bolkardağ, seiner nördlichen Randgebiete und westlichen Ausläufer. Veröff des Inst, M. T. A., Serie D, No. 7, 1955.
5. Blumenthal, M., Karaman-Konya havzası güneybatısında Toros kenar silsileleri ve şist-radyolarit formasyonunun stratigrafi meselesi. Maden Tetkik Arama Dergisi No 48, s. 1-36, 1956.
6. Blumenthal, M., Gülek Boğazı-Tarsus ile SilifkeMut arasındaki sahanın (Güney Anadolu Torosları / Kilikya Zonu) tabaka serileri ve yapısı. MTA Derleme Rapor No : 2590, Yayımlanmamış, 1961.
7. Akarsu.İ., Mut Bölgesi Jeolojisi. Maden Tetkik Arama Dergisi, Cilt 54, s.35-35, 1960, Ankara.
8. Niehoff, W., Mut 126/1 numaralı harita paftasının revizyon neticeleri hakkında rapor. MTA Derleme rapor no: 3390 (yayımlanmamış), 1960.
9. Özgül, N., Orta Torosların Kuzey Kesiminin Yapısal Gelişiminde Blok Hareketlerinin Önemi. Türkiye Jeoloji Bülteni, 14 (1), 85-101, 1971.
10. Özgül, N., Torosların bazı temel jeoloji özellikleri; Türkiye Jeol. Kur. Bült., 19/1, 65-78, 1976.
11. Koçyiğit, A., Karaman-Ermenek (Konya) Bölgesinde ofiyolitli melanj ve diğer oluşuklar. TJK Bülteni, 19: 103-116,1976.
12. Koçyiğit, A., Karaman-Ermenek arasındaki bölgenin tektoniği. Türkiye Jeoloji Kur. Bült., 20-1, 1-8,1977.
13. Şaroğlu, F., Boray, A., Özer, S., ve Kuşçu, İ., Orta Anadolu'nun Neotektoniği Üzerine Bazı Görüşler. Türkiye jeoloji Kurultayı Bildiri Özetleri,1982.
14. Şaroğlu, F., Boray, A., Özer, S., Kuşçu, İ., Orta Toroslar – Orta Anadolu'nun Güneyinin Neotektoniği İle İlgiliGörüşler. Jeomorfoloji Dergisi, S:11, s:35-44, 1983.
15. Demirtaşlı, E., Gedik, İ., İmik, M. Ermenek batısında Göktepe-Dumlugöze ve Tepebaşı arasında kalan bölgenin jeolojisi. Maden Tetkik ve Arama Genel Müdürlüğü Rapor No: 5783, Ankara (yayımlanmamış), 1986.
16. Pampal, S., Ayrancı Havzasında metamorfik Bolkar grubu ve Tersiyer oluşukları. Gazi Üni-versitesi Mühendislik Mimarlık Fakültesi Dergisi, 2 (2), 99-115, 1987.
17. Atabey, E., Atabey, N., Hakyemez, A., İslamoğlu, Y., Sözeri, Ş., Özçelik, N.N., Saraç, G., Ünay, E., Babayiğit, S., Mut-Karaman arası Miyosen havzasının litostratigrafisi ve sedimantolojisi (Orta Toroslar). Maden Tetkik Arama Enstitüsü Dergisi, Sayı 122, s. 53-72, 2000.
18. Gül, M. And Eren, M., The Sedimentary Characteristics of Dağpazarı Patch Reef (Middle Miocene, Mut- Içel/ Turkey). Carbonates and Evaporites, v. 18, No. 1, 2003, p. 51- 62,2003.
19. Mandic O., Harzhauser M., Schlaf J., Piller W. E. Schuster F., Wielandt-Schuster U., Nebelsick J.H., Kroh A., Rögl F., Bassant P., Palaeoenvironmentalreconstruction of an epicontinentalfl ooding-Burdigalian (early Miocene) of the Mut Basin (southern Turkey). Courier Forschunginstitut Senckenberg 248, 57- 92, 2004.
20. Bassant, P., van Buchem, F.S.P., Görür, N. The stratigraphic architecture and evolution of the Burdigalian carbonate–siliciclastic sedimentary systems of the Mut Basin, Turkey. Sedimentary Geology 173, 187–232, 2005.
21. Şafak, Ü., Kelling, G., Gökçen, N. and Gürbüz, K., The mid-Cenozoic succession and evolution of the Mut basin, southern Turkey, and its regional significance. Sedimentary Geology, 173(1):121-150, 2005.
22. Cipollari, P., Halasova, E., Gürbüz, K., Cosentino, D., Middle-Upper Miocene paleogeography of southern Turkey: insights from stratigraphy and calcareous nannofossil biochronology of the Olukpınar and Başyayla sections (Mut-Ermenek Basin). Turkish Journal of Earth Sciences 22, 820–838,2013.
23. Ilgar,A.,Esirtgen,T.,Hakyemez,A.,Çulha,G.,Demirkaya,S.,Türkm en-Bozkurt,B.,The control of sea-level changes on sedimentation in the Mut Basin: Late Serravallian-Early Tortonian incised valley-fill. Bull. Min. Res. Exp.159, 2019.
24. Erünal-Erentöz, L., Mollusques du Neogene desbassing de Karaman, Adana et Hatay (Turquie). MTA Bulletin, Serie, C, No: 4, 232 p. 36 pl., 1958.
25. Özer, B., Duval, B., Courrier, P., Letouzey, J., Antalya-Mut-Adana Neojen Havzaları Jeolojisi. Türkiye II. Petrol Kongresi, Ankara, 57–84, 1974.
26. Bizon, G., Bizon, J.J., Feinberg, H. ve Öztümer, E., Antalya-Mut-Adana Neojen Havzaları Tersiyer biyostratigrafiisi ve mikropaleontoloji yenilikleri. Türkiye ikinci Petrol Kongresi Tebliğleri, 217-228, 1974.
27. Gökten, E., Silifke yöresinin temel kaya birimleri ve Miyosen stratigrafisi. Türkiye Jeol. Kur. Bült., 19, 2, 103-117, 1976.
28. Tanar, Ü., Mut Havzası Tersiyer istifinin stratigrafisi ve mikropaleontolojisi, MTA Dergisi, sayı:110, s.175-180, 1989.
29. Tanar Ü., ve Gökçen, N., Mut-Ermenek Tersiyer istifinin stratigrafisi ve mikropaleontoljisi; MTA Derg., 110; 175-181, 1990.
30. Şafak, Ü., ve Gökçen, N., Planktik Foraminifer Zonlamasına Doğu Akdeniz Provensinden Bir Örnek: Mut Havzası Tersiyer İstifi, Türkiye Jeoloji Bülteni, C.34 27-3.5, 1991.
31. Özdoğan, M., Şahbaz, A., Transgresif set ada-lagüner sistemi içinde yıkanmış bir yelpaze deltanın gelişimi ve fasiyes özellikleri (Mut Miyosen havzası, Güney Türkiye). H.Ü. Yerbilimleri Uyg. ve Araş. Mrkz. Bülteni, 21, 143-160, 1999.
32. Özkan Köksoy, T., Catapsydrax, Globorotalia, Globigerinoita'n›n (planktik foraminifer) Mut havzas› denizel Miyosen istifindeki biyostratigrafisi ve sistematik paleontolojisi, Yerbilimleri, 29, 11-27, 2004.
33. Gürler, G., Mut Baseni (Güney Türkiye) Miyosen Resiflerin Mercan Sistematiği, Stratigrafisi Biyofasiyesleri ve Paleoekolojisi. Çukurova Üniversitesi Doktora Tezi, 2017.
34. Gedik, A., Birgili, Ş., Yılmaz, H. ve Yoldaş, R., Mut-Ermenek-Silifke yöresinin jeolojisi ve petrol olanakları. Türkiye Jeol. Kur. Bülteni, C.22, S.l s.7-26, 1979.
35. Korkmaz, S. ve Gedik, A., Mut - Ermenek - Silifke (Konya - Mersin) havzasında ana kaya fasiyesi ve petrol oluşumunun organik jeokimyasal yöntemlerle incelenmesi. Türkiye Jeoloji Bülteni, C. 33, 29-38,1990.
36. Şafak, Ü., Ünlügenç, U.C. ve Şenol, M., İncirlik (Adana güneydoğusu) çevresinde yeralan Geç Miyosen resifinin stratigrafisi ve mikropaleontolojisi. T.J.K. Bülteni, 11, 138-153, 1996.
37. Şafak, Ü. and Nurlu, N., A strontium isotopic, petrographic, and Ostracoda biostratigraphic study of Middle-Late Miocene sequences: implications of record in the Silifke–Erdemli/Mersin, southern Turkey. Arabian Journal of Geosciences 11:168, 2018.
38. Şafak, Ü., Antakya Havzası ostrakod biyostratigrafisi. Türkiye Jeoloji Bülteni, c.36, s.2, 115-137, 1993.
39. Boulton, S., Robertson, H.F. A., Ellam, R.M., Şafak, Ü. and

Ünlügenç, U.C., Strontium Isotopic and Micropalaeontological Dating Used to Help Redefine the Stratigraphy of the Neotectonic Hatay Graben, Southern Turkey. Turkish Journal of Earth Sciences (Turkish J. Earth Sci.), Vol. 16, pp.141-179, 2007.
40. Morkhoven, F.P.C.M., Post-Palaeozoic Ostracoda. V.II, 478 p., Newyork, 1963.
41. Doruk, N., A stereo-atlas of ostracod shells. Puplished by the department of Geology in the University of Leicester, volume 1, part 1, England, 1973.
42. Bassiouni, M.A., Brackische und marine Ostrocoden (Cytheridеinae, Hemicytherinae, Trachyleberidinae) aus dem Oligozaen und Neogen der Turkei. Geol. Jb. Reihe B, Heft 31, Hannover, 1-200, 1979.
43. Freels, D., Limnische Osrakoden aus jungtertiar und Quartarder Turkey. Geologische Jahrbuch, Reihe B, Heft 39, 172 p. ,1980.
44. Folk, R.L., Practial Petrographie classification of limestones. A.A.P.G. Bull., 43, 1-38, 1959.
45. Folk R.L., Spectral subdivision of limestone types, Amer. Assoc. Petrol. Geol. Mem. 1, p. 62–84, 1962.
46. Dunham, R.J., Classification of carbonate rocks according to depositional texture. In: Ham, W.E. (Ed.), Classification of Carbonate Rocks, 1,62–84, 108-121, 1962
47. Köksal, S., Toksoy-Köksal, F., Göncüoğlu, M.C., Petrogenesis and geodynamics of plagiogranites from Central Turkey (Ekecikdağ/Aksaray): new geochemical and isotopic data for generation in an arc basin system within the northern branch of Neotethys. Int. J. Earth Sci., 106, 1181–1203, 2017.
48. Köksal, S., Göncüoğlu, M.C., Sr and Nd Isotopic Characteristics of Some S-, I- and A-type Granitoids from Central Anatolia. Turkish J. Earth Sci., 17, 111–127, 2008.
49. Sezer, S., The Miocene stratigraphy of Mut region, southern Turkey (Doktora tezi). Bırkbeck college London University, 1970.
50. Demirel, İ. H., Köksoy, M., Ermenek Yöresinin Litostratigrafisi ve Jeoloji Evrimi. Türkiye 9. Petrol Kongresi, 17-21 Şubat 1992, s:198-206, 1992.
51. Schmitd, G.C., Adana petrol bölgesinin stratigrafik homenklatürü. Petrol Dairesi Negriyatı No. 6, s. 49-65, 1961.
52. Peterman, Z.E., Hetge, C.E., Tourtelot, H.A., Isotopiccomposition of strontium in sea water through out Phaner-ozoic time. Geochim. Cosmochim. Acta 34, 105, 1970.
53. Veizer, J., Compston, W., 87Sr/86Sr composition of seawater during the Phanerozoic. Geochim. Cosmochim. Acta 38,1461-1484, 1974.
54. Palmer M. R. and Edmond, J. M., Strontium isotope budget of the modern ocean. Earth Planet.Sci. Lett., 92, 11–26, 1989.
55. Taylor, A.S., Lasaga, A.C., The role of basalt weathering in the Sr isotope budget of the oceans. Chem. Geol. 161 (1–3), 199–21, 1999.
56. McArthur JM, Howarth RJ, Bailey T. R., Strontium isotope stratigraphy: LOWESS version 3: best fit to the marine Sr-isotope curve for 0–509 Ma and accompanying look-up table for deriving numerical age. J Geol 109:155–170, 2001.
57. Akay, E., Uysal, S., Poisson, A., Cravatte C.F.P.J. ve Müler, C., Antalya Neojen havzasının stratiğrafisi. Türkiye Jeoloji Kurumu Bülteni, 28, 105–119, 1985.
58. Şafak, Ü. ve Subaşı, Y., Beşkonak-Altınkaya (Serik KD'su, Antalya) dolayı Miyosen İstifinin mikropaleontolojik ve ortamsal özellikleri. İstanbul Üniversitesi Yerbilimleri Dergisi, Cilt 11, Sayı 1, s. 67-86, 1998.
59. Koçyiğit, A., Sarıkaya-Üçbaş (Karaman) Yöresinin Jeolojisi. Türkiye Jeoloji Kurumu Bülteni, c. 21, 77-86, 1978.
60. Şafak, Ü., Karaman yöresi Üst Miyosen-Pliyosen istifinin ostrakod faunası ve ortamsal yorumu. M. T. A. Dergisi, No. 119, 89-102, 1997.
61. Ünlügenç, U.C., Kelling, G., Williams, G.D., Demirkol, C., Aspects of Basin Evolution in the Neogene Adana Basin, SE Turkey, International Earth Sciens Congress on Aegean Regions (IESCA), 1-6 October, Edit: Savaşçın, M.Y. and Eronat,A.H., p. 353-369, 1990.
62. Avşar, N., Nazik, A., Dinçer, F. ve Darbaş, G. Adana Havzası Kuzgun Formasyonunun mikro fosiller ile ortamsal yorumu. Hacettepe Yerbilimleri Dergisi, 27 (1), 1-21, 2006.
63. Selçuk, H., Kızıldağ - Keldağ (Hatay) dolayının jeolojisi ve jeodinamik evrimi. M.T.A. Enst. (Doktora Tezi), 75 -103, 1985.
64. Demir, N. E., Mut doğu yöresi Miyosen yaştaki kayaçların stratigrafi si, Yük. Müh. Tezi. H.Ü. Fen Bilimleri Enstitüsü 93 s., Ankara, 1997.
65. Cosentino, D., Schildgen, T.F., Cipollari, P., Faranda, C., Gliozzi, E., Hudáčková, N., Lucifora, S., Strecker, M.R., Late Miocene surface uplift of the southern margin of the Central Anatolian plateau, Central Taurides, Turkey. Bulletin of the Geological Society of America 124, 133–145, 2012.
66. Ilgar, A., Nemec, W., Hakyemez, A., Karakuş, E., Messinian forced regressions in the Adana Basin: a near-coincidence of tectonic and eustatic forcing. Turkish Journal of Earth Sciences Special Publication 22, 864–889, 2013a.
67. Ilgar, A., Nemec, W., Hakyemez, A., Esirtgen, T., Messina, C., Türkmen, B., Çiner, A., The varied development and regional implications of late Serravalian erosional unconformity in the peri-Mediterranean basins of southern Turkey. RCMNS, 14th Congress of Regional Committee on Mediterranean Neogene Stratigraphy, İstanbul, Turkey, p. 21, 2013b.
68. Bremer, H., Paleontoloji. Ege Üniversitesi Fen Fakültesi Kitapları Serisi, No 46, 1978.
69. Sayar, C., Paleontoloji Omurgasız Fosiller. İstanbul Teknik Üniversitesi Kütüphanesi Sayı: 1435, 1991.
70. Morkhoven, F.P.C.M., Post-Palaeozoic Ostracoda. V.II, 478 p., Newyork, 1963.
71. Blumenthal, M.M., Niğde ve Adana vilâyetleri dahilinde Torosların jeolojisine umumi bakış. Maden Tetkik Arama Enat., Ankara, No 8, 48 s., 1941.
72. Blumenthall, M., Schichtfolge und Bauder Taurusketten im Hinterland Von Bozkır: Rev. Fak. Sc. Üniv., İstanbul, Serie B,t. lX, fasc., 2, 1944.
73. Blumenthal, M., Recherces géologiques dansle Taurus occidental dans l'arriere-pays d'Alanya. MTA Enst. Yay. Seri D., No: 5, 134 s., 1951.
74. Blumenthal, M., Géologie des Hohen Bolkardağ, seiner nördlichen Randgebiete und westlichen Ausläufer. Veröff des Inst, M. T. A., Serie D, No. 7, 1955.
75. Blumenthal, M., Karaman-Konya havzası güneybatısında Toros kenar silsileleri ve şist-radyolarit formasyonunun stratigrafi meselesi. Maden Tetkik Arama Dergisi No 48, s. 1-36, 1956.
76. Blumenthal, M., Gülek Boğazı-Tarsus ile SilifkeMut arasındaki sahanın (Güney Anadolu Torosları / Kilikya Zonu) tabaka serileri ve yapısı. MTA Derleme Rapor No : 2590, Yayımlanmamış, 1961.
77. Akarsu.İ., Mut Bölgesi Jeolojisi. Maden Tetkik Arama Dergisi, Cilt 54, s.35-35, 1960, Ankara.
78. Niehoff, W., Mut 126/1 numaralı harita paftasının revizyon neticeleri hakkında rapor. MTA Derleme rapor no: 3390 (yayımlanmamış), 1960.
79. Özgül, N., Orta Torosların Kuzey Kesiminin Yapısal Gelişiminde Blok Hareketlerinin Önemi. Türkiye Jeoloji Bülteni, 14 (1), 85-101, 1971.
80. Özgül, N., Torosların bazı temel jeoloji özellikleri; Türkiye Jeol. Kur. Bült., 19/1, 65-78, 1976.
81. Koçyiğit, A., Karaman-Ermenek (Konya) Bölgesinde ofiyolitli melanj ve diğer oluşuklar. TJK Bülteni, 19: 103-116,1976.

82. Koçyiğit, A., Karaman-Ermenek arasındaki bölgenin tektoniği. Türkiye Jeoloji Kur. Bült., 20-1, 1-8,1977.
83. Şaroğlu, F., Boray, A., Özer, S., ve Kuşçu, İ., Orta Anadolu'nun Neotektoniği Üzerine Bazı Görüşler. Türkiye jeoloji Kurultayı Bildiri Özetleri,1982.
84. Şaroğlu, F., Boray, A., Özer, S., Kuşçu, İ., Orta Toroslar – Orta Anadolu'nun Güneyinin Neotektoniği İle İlgiliGörüşler. Jeomorfoloji Dergisi, S:11, s:35-44, 1983.
85. Demirtaşlı, E., Gedik, İ., İmik, M. Ermenek batısında Göktepe-Dumlugöze ve Tepebaşı arasında kalan bölgenin jeolojisi. Maden Tetkik ve Arama Genel Müdürlüğü Rapor No: 5783, Ankara (yayımlanmamış), 1986.
86. Pampal, S., Ayrancı Havzasında metamorfik Bolkar grubu ve Tersiyer oluşukları. Gazi Üni-versitesi Mühendislik Mimarlık Fakültesi Dergisi, 2 (2), 99-115, 1987.
87. Atabey, E., Atabey, N., Hakyemez, A., İslamoğlu, Y., Sözeri, Ş., Özçelik, N.N., Saraç, G., Ünay, E., Babayiğit, S., Mut-Karaman arası Miyosen havzasının litostratigrafisi ve sedimantolojisi (Orta Toroslar). Maden Tetkik Arama Enstitüsü Dergisi, Sayı 122, s. 53-72, 2000.
88. Gül, M. And Eren, M., The Sedimentary Characteristics of Dağpazarı Patch Reef (Middle Miocene, Mut- Içel/ Turkey). Carbonates and Evaporites, v. 18, No. 1, 2003, p. 51- 62,2003.
89. Mandic O., Harzhauser M., Schlaf J., Piller W. E. Schuster F., Wielandt-Schuster U., Nebelsick J.H., Kroh A., Rögl F., Bassant P., Palaeoenvironmentalreconstruction of an epicontinentalfl ooding-Burdigalian (early Miocene) of the Mut Basin (southern Turkey). Courier Forschunginstitut Senckenberg 248, 57- 92, 2004.
90. Bassant, P., van Buchem, F.S.P., Görür, N. The stratigraphic architecture and evolution of the Burdigalian carbonate–siliciclastic sedimentary systems of the Mut Basin, Turkey. Sedimentary Geology 173, 187–232, 2005.
91. Şafak, Ü., Kelling, G., Gökçen, N. and Gürbüz, K., The mid-Cenozoic succession and evolution of the Mut basin, southern Turkey, and its regional significance. Sedimentary Geology, 173(1):121-150, 2005.
92. Cipollari, P., Halasova, E., Gürbüz, K., Cosentino, D., Middle-Upper Miocene paleogeography of southern Turkey: insights from stratigraphy and calcareous nannofossil biochronology of the Olukpınar and Başyayla sections (Mut-Ermenek Basin). Turkish Journal of Earth Sciences 22, 820–838,2013.
93. Ilgar,A.,Esirtgen,T.,Hakyemez,A.,Çulha,G.,Demirkaya,S.,Türkmen-Bozkurt,B.,The control of sea-level changes on sedimentation in the Mut Basin: Late Serravallian-Early Tortonian incised valley-fill. Bull. Min. Res. Exp.159, 2019.
94. Erünal-Erentöz, L., Mollusques du Neogene desbassing de Karaman, Adana et Hatay (Turquie). MTA Bulletin, Serie, C, No: 4, 232 p. 36 pl., 1958.
95. Özer, B., Duval, B., Courrier, P., Letouzey, J., Antalya-Mut-Adana Neojen Havzaları Jeolojisi. Türkiye II. Petrol Kongresi, Ankara, 57–84, 1974.
96. Bizon, G., Bizon, J.J., Feinberg, H. ve Öztümer, E., Antalya-Mut-Adana Neojen Havzaları Tersiyer biyostratigrafiisi ve mikropaleontoloji yenilikleri. Türkiye ikinci Petrol Kongresi Tebliğleri, 217-228, 1974.
97. Gökten, E., Silifke yöresinin temel kaya birimleri ve Miyosen stratigrafisi. Türkiye Jeol. Kur. Bült., 19, 2, 103-117, 1976.
98. Tanar, Ü., Mut Havzası Tersiyer istifinin stratigrafisi ve mikropaleontolojisi, MTA Dergisi, sayı:110, s.175-180, 1989.
99. Tanar Ü., ve Gökçen, N., Mut-Ermenek Tersiyer istifinin stratigrafisi ve mikropaleontoljisi; MTA Derg., 110; 175-181, 1990.
100. Şafak, Ü., ve Gökçen, N., Planktik Foraminifer Zonlamasına Doğu Akdeniz Provensinden Bir Örnek: Mut Havzası Tersiyer İstifi, Türkiye Jeoloji Bülteni, C.34 27-3.5, 1991.
101. Özdoğan, M., Şahbaz, A., Transgresif set ada-lagüner sistemi içinde yıkanmış bir yelpaze deltanın gelişimi ve fasiyes özellikleri (Mut Miyosen havzası, Güney Türkiye). H.Ü. Yerbilimleri Uyg. ve Araş. Mrkz. Bülteni, 21, 143-160, 1999.
102. Özkan Köksoy, T., Catapsydrax, Globorotalia, Globigerinoita'n›n (planktik foraminifer) Mut havzas› denizel Miyosen istifindeki biyostratigrafisi ve sistematik paleontolojisi, Yerbilimleri, 29, 11-27, 2004.
103. Gürler, G., Mut Baseni (Güney Türkiye) Miyosen Resiflerin Mercan Sistematiği, Stratigrafisi Biyofasiyesleri ve Paleoekolojisi. Çukurova Üniversitesi Doktora Tezi, 2017.
104. Gedik, A., Birgili, Ş., Yılmaz, H. ve Yoldaş, R., Mut-Ermenek-Silifke yöresinin jeolojisi ve petrol olanakları. Türkiye Jeol. Kur. Bülteni, C.22, S.l s.7-26, 1979.
105. Korkmaz, S. ve Gedik, A., Mut - Ermenek - Silifke (Konya - Mersin) havzasında ana kaya fasiyesi ve petrol oluşumunun organik jeokimyasal yöntemlerle incelenmesi. Türkiye Jeoloji Bülteni, C. 33, 29-38,1990.
106. Şafak, Ü., Ünlügenç, U.C. ve Şenol, M., İncirlik (Adana güneydoğusu) çevresinde yeralan Geç Miyosen resifinin stratigrafisi ve mikropaleontolojisi. T.J.K. Bülteni, 11, 138-153, 1996.
107. Şafak, Ü. and Nurlu, N., A strontium isotopic, petrographic, and Ostracoda biostratigraphic study of Middle-Late Miocene sequences: implications of record in the Silifke–Erdemli/Mersin, southern Turkey. Arabian Journal of Geosciences 11:168, 2018.
108. Şafak, Ü., Antakya Havzası ostrakod biyostratigrafisi. Türkiye Jeoloji Bülteni, c.36, s.2, 115-137, 1993.
109. Boulton, S., Robertson, H.F. A., Ellam, R.M., Şafak, Ü. and Ünlügenç, U.C., Strontium Isotopic and Micropalaeontological Dating Used to Help Redefine the Stratigraphy of the Neotectonic Hatay Graben, Southern Turkey. Turkish Journal of Earth Sciences (Turkish J. Earth Sci.), Vol. 16, pp.141-179, 2007.
110. Morkhoven, F.P.C.M., Post-Palaeozoic Ostracoda. V.II, 478 p., Newyork, 1963.
111. Doruk, N., A stereo-atlas of ostracod shells. Puplished by the department of Geology in the University of Leicester, volume 1, part 1, England, 1973.
112. Bassiouni, M.A., Brackische und marine Ostrocoden (Cytherideinae, Hemicytherinae, Trachyleberidinae) aus dem Oligozaen und Neogen der Turkei. Geol. Jb. Reihe B, Heft 31, Hannover, 1-200, 1979.
113. Freels, D., Limnische Osrakoden aus jungtertiar und Quartarder Turkey. Geologische Jahrbuch, Reihe B, Heft 39, 172 p. ,1980.
114. Folk, R.L., Practial Petrographie classification of limestones. A.A.P.G. Bull., 43, 1-38, 1959.
115. Folk R.L., Spectral subdivision of limestone types, Amer. Assoc. Petrol. Geol. Mem. 1, p. 62–84, 1962.
116. Dunham, R.J., Classification of carbonate rocks according to depositional texture. In: Ham, W.E. (Ed.), Classification of Carbonate Rocks, 1,62–84, 108-121, 1962
117. Köksal, S., Toksoy-Köksal, F., Göncüoğlu, M.C., Petrogenesis and geodynamics of plagiogranites from Central Turkey (Ekecikdağ/Aksaray): new geochemical and isotopic data for generation in an arc basin system within the northern branch of Neotethys. Int. J. Earth Sci., 106, 1181–1203, 2017.
118. Köksal, S., Göncüoğlu, M.C., Sr and Nd Isotopic Characteristics of Some S-, I- and A-type Granitoids from Central Anatolia. Turkish J. Earth Sci., 17, 111–127, 2008.
119. Sezer, S., The Miocene stratigraphy of Mut region, southern Turkey (Doktora tezi). Bırkbeck college London University, 1970.

120. Demirel, İ. H., Köksoy, M., Ermenek Yöresinin Litostratigrafisi ve Jeoloji Evrimi. Türkiye 9. Petrol Kongresi, 17-21 Şubat 1992, s:198-206, 1992.
121. Schmitd, G.C., Adana petrol bölgesinin stratigrafik homenklatürü. Petrol Dairesi Negriyatı No. 6, s. 49-65, 1961.
122. Peterman, Z.E., Hetge, C.E., Tourtelot, H.A., Isotopiccomposition of strontium in sea water through out Phaner-ozoic time. Geochim. Cosmochim. Acta 34, 105, 1970.
123. Veizer, J., Compston, W., 87Sr/86Sr composition of seawater during the Phanerozoic. Geochim. Cosmochim. Acta 38,1461-1484, 1974.
124. Palmer M. R. and Edmond, J. M., Strontium isotope budget of the modern ocean. Earth Planet.Sci. Lett., 92, 11–26, 1989.
125. Taylor, A.S., Lasaga, A.C., The role of basalt weathering in the Sr isotope budget of the oceans. Chem. Geol. 161 (1–3), 199–21, 1999.
126. McArthur JM, Howarth RJ, Bailey T. R., Strontium isotope stratigraphy: LOWESS version 3: best fit to the marine Sr-isotope curve for 0–509 Ma and accompanying look-up table for deriving numerical age. J Geol 109:155–170, 2001.
127. Akay, E., Uysal, S., Poisson, A., Cravatte C.F.P.J. ve Müler, C., Antalya Neojen havzasının stratiğrafisi. Türkiye Jeoloji Kurumu Bülteni, 28, 105–119, 1985.
128. Şafak, Ü. ve Subaşı, Y., Beşkonak-Altınkaya (Serik KD'su, Antalya) dolayı Miyosen İstifinin mikropaleontolojik ve ortamsal özellikleri. İstanbul Üniversitesi Yerbilimleri Dergisi, Cilt 11, Sayı 1, s. 67-86, 1998.
129. Koçyiğit, A., Sarıkaya-Üçbaş (Karaman) Yöresinin Jeolojisi. Türkiye Jeoloji Kurumu Bülteni, c. 21, 77-86, 1978.
130. Şafak, Ü., Karaman yöresi Üst Miyosen-Pliyosen istifinin ostrakod faunası ve ortamsal yorumu. M. T. A. Dergisi, No. 119, 89-102, 1997.
131. Ünlügenç, U.C., Kelling, G., Williams, G.D., Demirkol, C., Aspects of Basin Evolution in the Neogene Adana Basin, SE Turkey, International Earth Sciens Congress on Aegean Regions (IESCA), 1-6 October, Edit: Savaşçın, M.Y. and Eronat,A.H., p. 353-369, 1990.
132. Avşar, N., Nazik, A., Dinçer, F. ve Darbaş, G. Adana Havzası Kuzgun Formasyonunun mikro fosiller ile ortamsal yorumu. Hacettepe Yerbilimleri Dergisi, 27 (1), 1-21, 2006.
133. Selçuk, H., Kızıldağ - Keldağ (Hatay) dolayının jeolojisi ve jeodinamik evrimi. M.T.A. Enst. (Doktora Tezi), 75 -103, 1985.
134. Demir, N. E., Mut doğu yöresi Miyosen yaştaki kayaçların stratigrafi si, Yük. Müh. Tezi. H.Ü. Fen Bilimleri Enstitüsü 93 s., Ankara, 1997.
135. Cosentino, D., Schildgen, T.F., Cipollari, P., Faranda, C., Gliozzi, E., Hudáčková, N., Lucifora, S., Strecker, M.R., Late Miocene surface uplift of the southern margin of the Central Anatolian plateau, Central Taurides, Turkey. Bulletin of the Geological Society of America 124, 133–145, 2012.
136. Ilgar, A., Nemec, W., Hakyemez, A., Karakuş, E., Messinian forced regressions in the Adana Basin: a near-coincidence of tectonic and eustatic forcing. Turkish Journal of Earth Sciences Special Publication 22, 864–889, 2013a.
137. Ilgar, A., Nemec, W., Hakyemez, A., Esirtgen, T., Messina, C., Türkmen, B., Çiner, A., The varied development and regional implications of late Serravalian erosional unconformity in the peri-Mediterranean basins of southern Turkey. RCMNS, 14th Congress of Regional Committee on Mediterranean Neogene Stratigraphy, İstanbul, Turkey, p. 21, 2013b.
138. Bremer, H., Paleontoloji. Ege Üniversitesi Fen Fakültesi Kitapları Serisi, No 46, 1978.
139. Sayar, C., Paleontoloji Omurgasız Fosiller. İstanbul Teknik Üniversitesi Kütüphanesi Sayı: 1435, 1991.

Plate I

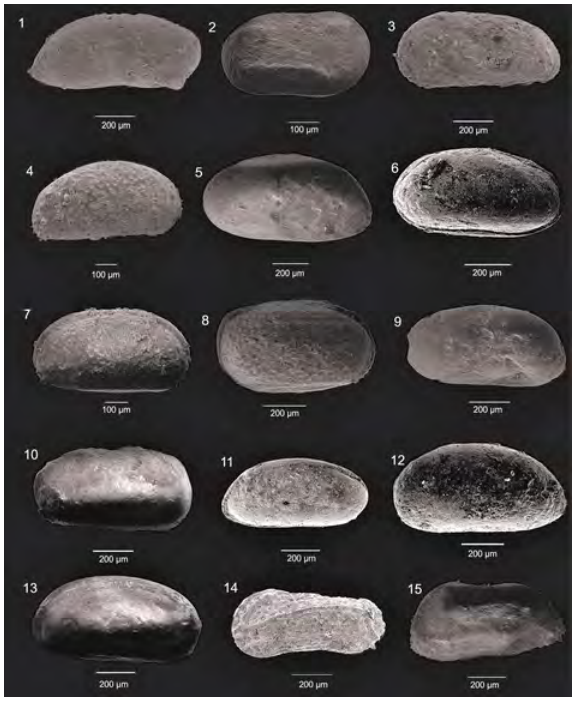

Figure 1. Bythocypris lucida (Sequenza)
1. Left cover, side view, Dağpazarı 1 Measured Stratigraphy Section, Sample 21
Figure 2. Cytherella glypta Doruk
2. Shell, left exterior view, Dağpazarı 2 Measured Stratigraphy Section, Sample 3
Figure 3. Cytheridea acuminata neapolitana Kollmann
3. Left cover, side view, Dağpazarı 1 Measured Stratigraphy Section, Sample 7
Figure 4. Cytheridea acuminata acuminata Bosquet
4. Right cover, side view, Dağpazarı 1 Measured Stratigraphy Section, Sample 26
Figure 5-6. Cyamocytheridea reversa (Egger)
5. Carapace, right external view, Dağpazarı 1 Measured Stratigraphy Section, Sample 22
6. Shell, right external view, Dağpazarı 1 Measured Stratigraphy Section, Sample 13
Figure 7-8. Cyamocytheridea meniscus Doruk
2. Shell, left exterior view, Dağpazarı 1 Measured Stratigraphy Section, Sample 26
3. Carapace, right side view, Dağpazarı 1 Measured Stratigraphy Section, Sample 17
Figure 9-10. Pontocythere elongata (Brady)
9. Shell, right external view, Dağpazarı 1 Measured Stratigraphy Section, Sample 21
10. Carapace, right side view, Dağpazarı 1 Measured Stratigraphy Section, Sample No. 21
Figure 11-12. Krithe citae Oertli
11. Shell, right external view, Dağpazarı 1 Measured Stratigraphy Section, Sample 23
12. Right cover, side view, Dağpazarı 1 Measured Stratigraphy Section, Sample 13
Figure 13. Krithe monosteracensis (Sequenza)
13. Shell, right external view, Dağpazarı 1 Measured Stratigraphy Section, Sample 26
Figure 14. Cistacythereis pokornyi (Ruggieri)
14. Shell, left exterior view, Dağpazarı 1 Measured Stratigraphy Section, Sample 31
Figure 15. Ruggieria tetraptera tetraptera (Sequenza)
15. Shell, left exterior view, Dağpazarı 2 Measured Stratigraphy Section, Sample 10

Plate II

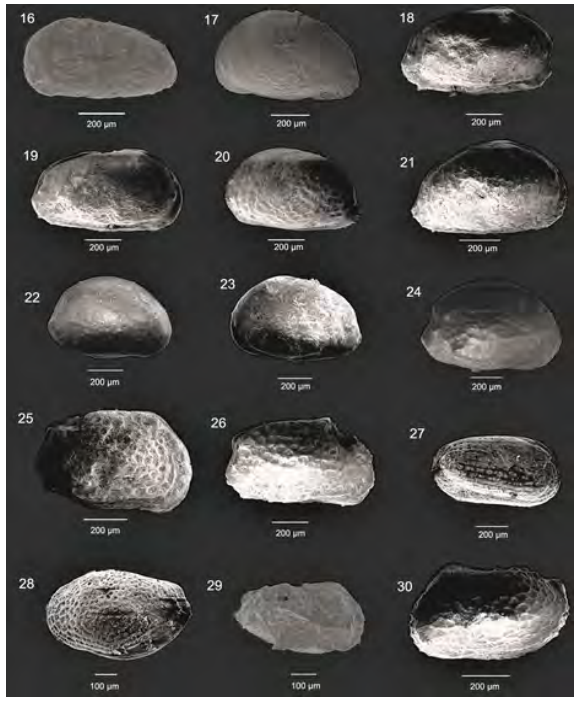

Figure 16. Thalmannia clauda (Doruk)
16. Shell, left exterior view, Dağpazarı 1 Measured Stratigraphy Section, Sample 32
Figure 17. Aurila convexa (Baird)
17. Shell, left exterior view, Dağpazarı 2 Measured Stratigraphy Section, Sample 10
Figure 18-19. Aurila freudenthali Sissingh
18. Shell, right external view, Dağpazarı 1 Measured Stratigraphy Section, Sample 26
19. Shell, right external view, Dağpazarı 1 Measured Stratigraphy Section, Sample 26
Figure 20-21. Aurila ulicznyi Sissingh
20. Shell, left exterior view, Dağpazarı 1 Measured Stratigraphy Section, Sample 28
21. Shell, right external view, Dağpazarı 1 Measured Stratigraphy Section, Sample 17
Figure 22. Aurila speyeri (Brady)
22. Shell, right external view, Dağpazarı 2 Measured Stratigraphy Section, Sample 9
Figure 23. Aurila soummamensis Coutelle and Yassini
23. Shell, left exterior view, Dağpazarı 1 Measured Stratigraphy Section, Sample 28
Figure 24. Pokornyella deformis minor Moyes
24. Shell, right external view, Dağpazarı 2 Measured Stratigraphy Section, Sample 11
Figure 25. Tenedocythere prava (Baird)
25. Shell, right external view, Dağpazarı 1 Measured Stratigraphy Section, Sample 22
Figure 26. Tenedocythere salebrosa Uliczny,
26. Shell, right external view, Dağpazarı 1 Measured Stratigraphy Section, Sample 28
Figure 27. Cytheretta semiornata (Egger)
27. Shell, right external view, Dağpazarı 1 Measured Stratigraphy Section, Sample 34
Figure 28. Loxoconcha rhomboidea (Fischer)
28. Shell, left exterior view, Dağpazarı 1 Measured Stratigraphy Section, Sample 28
Figure 29. Loxoconcha cristatissima Ruggieri
29. Shell, right external view, Dağpazarı 1 Measured Stratigraphy Section, Sample 31
Figure 30. Loxocorniculum quadricornis (Ruggieri)
30. Shell, left exterior view, Dağpazarı 1 Measured Stratigraphy Section, Sample 31

Research Article
Hittite Journal of Science and Engineering, 2023, 10 (4) 301–307
ISSN NUMBER: 2149–2123
DOI: 10.17350/hjse19030000319

Bending of a Cross-Ply Laminated Composite Beam Under a Sinusoidal Transverse Loading

Fatih Karaçam
Trakya University, Department of Mechanical Engineering, Edirne, Türkiye

ABSTRACT

Bending of a laminated composite beam under to a sinusoidal loading is carried out for simply support boundary condition for a specific cross-ply stacking sequence. To demonstrate the accuracy of the analytical results, a computer-aided engineering (CAE) approach is used. In the analytical solution, a unified shear deformation theory with a parabolic shape function is used. The longitudinal and vertical displacements, normal and shear stresses, namely, the bending stresses of analytical and CAE solutions are obtained and compared with the literature. Although two different methods are used in the study, the analysis results converge to the reference values. The variation of the displacements, normal and shear stresses are illustrated in the graphics with respect to the beam length and thickness respectively.

Article History:
Received: 2023/04/10
Accepted: 2023/10/27
Online: 2023/12/31

***Correspondence to**: Fatih Karaçam,*
E-Mail: fatihkar@trakya.edu.tr
Phone: +90 284 226 1226 (1217)
Fax: +90 284 226 1218

This article has been checked for similarity.

Keywords:
Bending; Static analysis; Laminated composite beam; Shear deformation beam theory; Computer-aided engineering

INTRODUCTION

Since the composite materials can be designed in different ways with the desired mechanical properties for various stacking sequences, matrix and fiber materials, they have been widely used in many structural elements. These elements are generally constructed of laminated composite materials, and too many design parameters are taken into consideration in the design and analysis process. Sankar (2001) obtained an elasticity solution for laminated beams under sinusoidal loading. The stresses and displacements were obtained by use of a non-dimensionalized design parameter that varies exponentially for constant mechanical properties [1]. Sayyad et al (2014) performed a static flexural analysis of a simply supported single-layer composite beam under various loadings and obtained the results by a precise elasticity solution [2]. Sayyad et al (2015) investigated the bending of composite beams by use of a trigonometric beam theory due to transverse shear deformation, ad compared the results with those of the other trigonometric theories [3]. Pimenta et al (2015) investigated the sinusoidal-web beams under the effects of lateral and torsional buckling. In this manner, firstly, an experimental investigation was performed, and then a finite-element model was created and tested using the data from the experiments. In the prediction of the beam resistance, a theoretical model was proposed, and a computational program was established. Finally, using the first order reliability approach, reliability analyses were performed, and the results were compared with the literature [4]. Pagani et al (2017) developed the static analyses of sandwich, and laminated beams under a transverse sinusoidal loading by applying the Lagrange expansion-based refined beam model for a simple supported boundary condition. The 3-D FEM (Finite Element Method) results were computed and compared with the previous studies [5]. Jiaoa et al (2017) investigated the effect of geometry of composite I-beams for the buckling capacity theoretically, and in order to validate the theoretical approach, number of experiments and simulations were carried out [6]. Liu et al (2018) searched the non-linear bending behavior of anisotropic composite beams for different distributed loadings and compared the results with FEM solution [7]. Dorduncu (2019) investigated the bending stresses of composite beams by use of a refined zigzag theory. The method's capabilities and robustness were presented for various sets of aspect ratios and boundary conditions [8]. Karakoti and Kar (2019) examined the sinusoidally-corrugated laminated composite panels by use of a customized computational code to obtain the bending responses of panels for various boundary conditions. The model's accuracy was confirmed with the comparison and validation of the analytical results [9]. Pandey and Gadade (2019) used FEM in the static analysis of a composite beam. As a present model, the nine-noded, 12-degree-of-

Cite as:
Karacam F, "Bending of a Cross-Ply Laminated Composite Beam Under a Sinusoidal Transverse Loading". Hittite J Sci Eng. 2023;10 (4): 301-307. doi:10.17350/hjse19030000319

freedom isoparametric Lagrange interpolation function was developed. To compare the FEM results with the literature, the maximum non-dimensionalized deflection values for symmetric and unsymmetric laminates under concentrated loads were calculated for various boundary conditions [10]. By taking into account four different carbon nanotube distributions, Sobhy (2019) introduced a novel analytical method for the bending of functionally graded plates reinforced with single-walled carbon nanotube in different temperature conditions. For simply supported boundary condition, the present plate was subjected to various distributed loadings, and non-dimensionalized stress and displacement values were obtained [11]. In the bending and vibrational analysis of reinforced beams, Wang et al. (2019) suggested a 2-D (Two-Dimensional) elasticity model for a sinusoidal distributed load and various boundary conditions, non-dimensionalized displacement, stress, and natural frequency parameters were derived [12]. Pathirana and Qiao (2019) investigated the critical buckling load of sinusoidal panels under simply support boundary condition by use of Rayleigh-Ritz method. To predict the critical load, a semi-analytical solution was used, and due to the finite element analysis, the results were obtained with better correlation. Considering the twisting capacities and different material properties, the study was conducted to assess the effects of the buckling amplitude, thickness, and aspect ratio [13]. Pathirana and Qiao (2020) studied the buckling behaviour sinusoidal panels under in-plane loading by Rayleigh-Ritz approach. The local buckling load is predicted accurately by a precise solution method. The local buckling behavior were captured at any aspect ratios, thickness, and amplitudes [14]. Zaboon and Jassim (2022) used the classical lamination theory to obtain the analytical solutions for laminated composite beams. In the analytical bending solution, several boundary conditions and loadings were taken into consideration. The boundary conditions were chosen as simple-simple, clamped-free and clamped–clamped, and the loading types were chosen at the center point with uniform distributed load [15]. Zhu et al (2022) investigated the properties of engineered cementitious composites due to the ductility, strength, fatigue and cracking behavior. To examine the impacts of various fiber contents, three different types of hybrid designed cementitious composites with various volume fractions of steel and polyethylene fiber were evaluated [16].

In the present work, the bending analysis of a cross-ply laminated composite beam under a uniform sinusoidal transverse loading for simple support boundary condition is performed both analytically and by use of a CAE software. For the comparison purposes, initially, the longitudinal and vertical displacements, normal and shear stresses are obtained analytically for a specific material, at different points where the maximum displacements and stresses may occur. The computer aided engineering approach is developed for given parameters, and the results are compared with the ones obtained by use of finite element method and analytically by use of a shear deformation beam theory in the literature [20-21].

ANALYTICAL MODEL

The beam is assumed to have a rectangular cross-section and constructed of linear elastic layers. It has a length of "L", total thickness of "h", unit width, and the coordinate axes are located at the mid-plane where $0 \le x \le L$ and $-h/2 \le z \le h/2$, respectively. A laminated composite beam under a uniform sinusoidal transverse loading is presented in Fig.1.

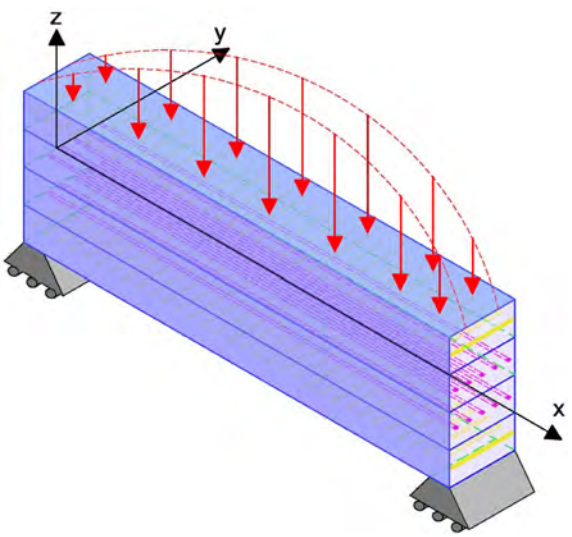

Figure 1. A laminated composite beam under a uniform sinusoidal transverse loading

In the analytical solution, a unified shear deformation beam theory is used which is firstly applied to the composite shells developed by Soldatos and Timarcı (1993). The shear deformation effects are taken into consideration by use of a general shape function "$\phi(z)$" depending on the beam thickness. In addition, with the appropriate selection of the shape functions, the previous beam theories can also be obtained. The displacement fields for the unified shear deformation beam theory are given as follows:

$$\begin{aligned} U(x,y,z;t) &= u(x,y;t) - z\, w(x;t)_{,x} + \varnothing(z)\, u_1(x;t) \\ V(x,y,z;t) &= v(x,y;t) - z\, w(x;t)_{,y} + \varnothing(z)\, v_1(x;t) \\ W(x,y,z;t) &= w(x,y;t) \end{aligned} \tag{1}$$

Since the displacement component along y-axis is zero for the beam, the following displacement fields "U" and "W" are obtained as follows, where "u", "w" and "u_1" are the displacement functions of the mid-plane.

$$U(x,z;t) = u(x;t) - z\,w(x;t)_{,x} + \varnothing(z)\,u_1(x;t)$$
$$W(x,y,z;t) = w(x,y;t) \tag{2}$$

In order to satisfy the stress-free conditions at the top and bottom surfaces and continuity of interlaminar stresses through the thickness of the beam, a parabolic shape function is chosen in the study as follows [17]:

$$\varnothing(z) = z\left(1 - \frac{4z^2}{3h^2}\right) \tag{3}$$

The displacement fields given in Eq. 2 yield to the kinematic relations where the subscript "," corresponds to the differentiation with the relevant axis.

$$\varepsilon_x = u_{,x} - z\,w_{,xx} + \varnothing(z)\,u_{1,x}$$
$$\gamma_{xz} = \varnothing'(z)\,u_1 \tag{4}$$

Using the generalized Hooke's law, the stress-strain relations in each layer of the beam can be expressed as follows:

$$\begin{bmatrix} \sigma_x \\ \tau_{xz} \end{bmatrix} = \begin{bmatrix} \bar{Q}_{11} & 0 \\ 0 & \bar{Q}_{55} \end{bmatrix} \begin{bmatrix} \varepsilon_x \\ \gamma_{xz} \end{bmatrix} \tag{5}$$

The transformed reduced stiffness "$\bar{Q}_{ij}$" depend on the reduced stiffness "Q_{ij}" and fiber orientation angles "θ" of the relevant layers (Jones, 1975). The rigidities with two subscripts, and more than two subscripts correspond to the classical and shear deformation beam theories, respectively [18].

$$\bar{Q}_{11} = Q_{11}cos^4\theta + 2(Q_{12} + 2Q_{66})sin^2\theta cos^2\theta + Q_{22}sin^4\theta$$
$$\bar{Q}_{55} = Q_{44}sin^4\theta + Q_{55}cos^4\theta \tag{6}$$

The reduced stiffness parameters depend on the mechanical properties such as elasticity modulus "E", shear modulus "G" and Poisson's ratio "ν", and are given as follows:

$$Q_{11} = \frac{E_1}{1-\nu_{12}\nu_{21}},\ Q_{12} = Q_{21} = \frac{E_2\nu_{21}}{1-\nu_{12}\nu_{21}},\ Q_{22} = \frac{E_2}{1-\nu_{12}\nu_{21}}$$
$$Q_{44} = G_{23},\ Q_{55} = G_{13},\ Q_{66} = G_{12} \tag{7}$$

$$\frac{E_1}{E_2} = \frac{\nu_{12}}{\nu_{21}} \tag{8}$$

By the appropriate use of stress-strain relations in the force and moment equations,

$$N_x = \int_{-h/2}^{h/2} \sigma_x\,dz,\ Q_x^a = \int_{-h/2}^{h/2} \tau_{xz}\,\Phi^{\bullet}(z)\,dz$$
$$\boldsymbol{M}_x = \int_{-h/2}^{h/2} \sigma_x z\,dz,\ M_x^a = \int_{-h/2}^{h/2} \sigma_x \Phi(z)\,dz \tag{9}$$

the following constitutive equations are obtained. "a" corresponds to the shear deformation effects, "A", "B", "D" denote the extensional, coupling and bending rigidities respectively, and " "Q_x^a" Q_xa" is the shear force. Rigidities with two subscripts correspond to the classical theory, whereas the ones with more than two subscripts correspond to shear deformation theory.

$$\begin{bmatrix} N_x \\ M_x \\ M_x^a \end{bmatrix} = \begin{bmatrix} A_{11} & B_{11} & B_{111} \\ B_{11} & D_{11} & D_{111} \\ B_{111} & D_{111} & D_{1111} \end{bmatrix} \begin{bmatrix} u_{,x} \\ -w_{,xx} \\ u_{1,x} \end{bmatrix},\ Q_x^a = A_{55}u_1 \tag{10}$$

The extensional, coupling and bending rigidities are defined as follows:

$$A_{11} = \int_{-h/2}^{h/2} \bar{Q}_{11}^{(k)}dz,\ A_{55} = \int_{-h/2}^{h/2} \bar{Q}_{55}^{(k)}\left(\varnothing'(z)\right)^2\,dz$$
$$B_{11} = \int_{-h/2}^{h/2} \bar{Q}_{11}^{(k)}z\,dz,\ B_{111} = \int_{-h/2}^{h/2} \bar{Q}_{55}^{(k)}\varnothing(z)\,dz$$
$$D_{11} = \int_{-h/2}^{h/2} \bar{Q}_{11}^{(k)}z^2\,dz, D_{111} = \int_{-h/2}^{h/2} \bar{Q}_{11}^{(k)}\varnothing(z)\,z\,dz,$$
$$D_{1111} = \int_{-h/2}^{h/2} \bar{Q}_{11}^{(k)}\left(\varnothing(z)\right)^2\,dz \tag{11}$$

For a laminated beam under a uniform transverse loading of q(x), the governing equations can be considered as follows:

$$N_{x,x} = 0$$
$$M_{x,xx} = q(x)$$
$$M_{x,x}^a - Q_x^a = 0 \tag{12}$$

The beam is considered to be under a uniform sinusoidal loading where "m" is the wave number, and given as follows:

$$q(x) = q_0\,sin(\alpha x),\ \alpha = \frac{m\pi}{L}(m = 1,2,\ldots) \tag{13}$$

The boundary conditions prescribed at both ends where x=0 and x=L, are obtained by application of Hamilton's principle, and given for simply supported, cantilever and free boundary conditions respectively.

$$N_x = w = M_x = M_x^a = 0$$
$$u = w = w_{,x} = u_1 = 0$$
$$N_x = M_{x,x} = M_x = M_x^a = 0 \tag{14}$$

In order to satisfy the simple support boundary condition, the following Navier-type displacement functions are used, whereas "C_1", "C_2" and "C_3" are the amplitudes of the displacement functions.

$$u = C_1\,sin\left(\frac{m\pi x}{L}\right),\ u_1 = C_2\,cos\left(\frac{m\pi x}{L}\right),\ w = C_3\,sin\left(\frac{m\pi x}{L}\right) \tag{15}$$

Using the constitutive equations in governing equations, the set of three equations with three unknowns are obtained. The unknown parameters can be determined computationally when the boundary condition is applied at both ends.

FINITE ELEMENT MODEL

In recent years, it has been observed that the use of computer-aided design software is insufficient especially in determining the static and dynamic loads, and the thermal effects of the designs under specific operating conditions. Since the performance of the design will largely depend on the actual operating conditions, it is of great importance to predict these conditions correctly. Under the consideration of these parameters, it will be wise to use a different software solution in the analysis of engineering designs. In the design process, a CAE software is generally used to include the real operating conditions and to create a simulation and perform the analysis in a virtual environment. The CAE software is commonly used in many engineering fields such as automotive, aerodynamic, flow and structural analysis. Especially in the engineering applications, the optimum results can be obtained in a shorter time with the minimum cost. While the design process of a product or system is independent of time and operating conditions, the same parameters should also be taken into consideration in the analysis. The reliability of the results will largely depend on the correct use of the solution technique and the limit values. Thus, the theoretical information in the relevant study becomes significant in the determination of these values. Therefore, especially in cases where the theoretical information is incorrect or insufficient, CAE software may not give the correct or sufficient results. Number of different analyses such as static strength, fatigue, vibration, heat transfer and impact can be performed by use of the finite element method (FEM) based engineering software. As a result, the CAE software shortens the time required for the design process considerably and allows to analyze and predict the optimum results for the product or system before the manufacturing process. In this study, Abaqus is utilized for the CAE solution. Since the plane and shell elements are generally effective in modelling and analyzing the laminated composite structures and converge faster, 3-D brick elements are chosen for the solid modelling.

RESULTS AND DISCUSSION

The vertical and longitudinal displacements and the shear and normal stresses, namely, the bending stresses are presented in Table 1 at different points. The vertical and longitudinal displacement values are obtained at x=L/2, z=0 and x=0, z=h/2, respectively. The normal stresses are obtained at x=L/2, z=h/4, whereas the shear stresses are obtained at x=L/4, z=0 in accordance with Ref. [15].

The beam is simply supported, constructed of four layers, has the stacking sequence of [$90^0/0^0/0^0/90^0$], length of L=6.35 m, thickness of h=2.794 m and a uniform sinusoidal distributed loading q_0=1000 N/m is applied at the top. The beam material is chosen as boron/epoxy with the following mechanical properties [19]:

$$\begin{aligned} &E_{11} = 241.5\ GPa,\quad E_{22} = E_{33} = 18.89\ GPa \\ &G_{23} = 3.45\ GPa,\quad G_{12} = G_{13} = 5.18\ GPa \\ &\nu_{23} = 0.25,\quad \nu_{12} = \nu_{13} = 0.24 \end{aligned} \tag{16}$$

The results are compared with Karama et al (1998) that were obtained by Abaqus software [20]. The vertical and longitudinal displacements and bending stresses were also obtained by use of a sinusoidal and exponential shape functions in Karama et al (1998, 2003), and a parabolic shape function in Karacam (2005) [21], respectively. In the present study, the numerical results have shown that the proposed model has better results than the others. In the determination of the displacement and stress values, a unified shear deformation beam theory in which the previous beam theories can be obtained by use of an appropriate shape function, is adopted in the numerical model. In the comparison of results, the following equation is used to obtain the error in percentage.

$$Error(\%) = \frac{(Reference\ Value - New\ Value)}{Reference\ Value} \times 100 \tag{17}$$

Table 1. The vertical (W) and longitudinal (U) displacements, shear (τ_{xz}) and normal (σ_{xx}) stresses for simple support boundary condition.

Model	W (×10⁻⁴) [m]	U (×10-4) [m]	τ_{xz} [Pa]	σ_{xx} [Pa]
Present Study	-6.2155	2.3554	-1031670	7685460
Error (%)	1.88	1.85	2.55	1.91
Karaçam (2005)	-6.2317	2.0382	-892316	7527000
Error (%)	2.2	11.8	11.3	3.9
Karama (2003)	-6.3701	2.1196	-940098	8112840
Error (%)	4.4	8.3	6.6	3.5
Karama (1998)	-6.1006	2.3125	-1006000	7835200

In Fig. 2, the variation of vertical displacement is presented along the beam length. In accordance with the simply support boundary condition, the displacement values at the beginning and end of the beam where x=0 and x=L, are obtained as zero. The maximum displacement value is obtained in the middle of the beam as it is expected. Due to the sinusoidal transverse loading, the negative values in the vertical axis indicate that the displacement values are obtained in the negative z- direction.

In Fig. 3, the vertical displacement distribution is presented. It is obvious from the figure that both sides of the beam which are illustrated in red regions have zero displacement, whereas the regions in dark blue correspond to the maximum displacement values.

In Fig. 4, the variation of longitudinal displacement along the beam thickness is presented. Since the sinusoidal loading acts from the top, the upper surface of the beam is

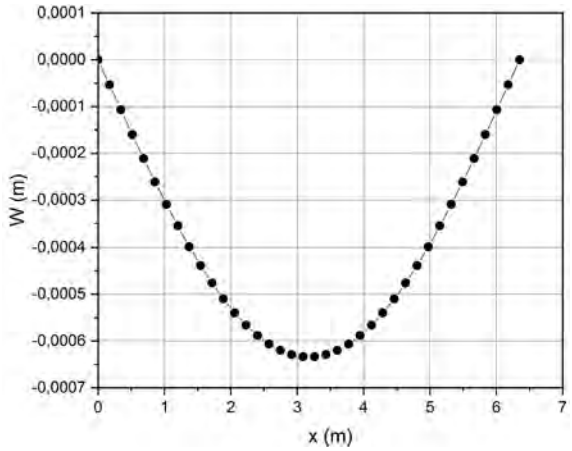

Figure 2. The variation of vertical displacement along the beam length.

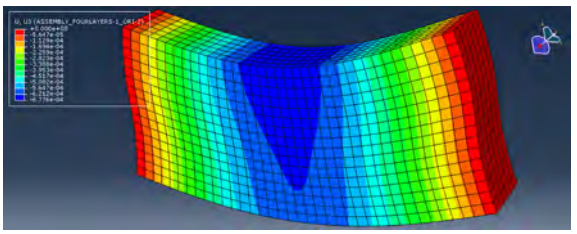

Figure 3. The vertical displacement distribution.

lengthened, whereas the lower surface is shorten. Thus, the maximum values are obtained at the bottom and top surfaces where z=h/2 and z=-h/2. The longitudinal displacement values presented along x-axis in the figure have a common factor of "10^{-4}". Since the longitudinal displacement at the mid-plane of the beam when z=0 is "0.06×10^{-4}", it is obvious from the figure that the displacement at this value is very close to zero.

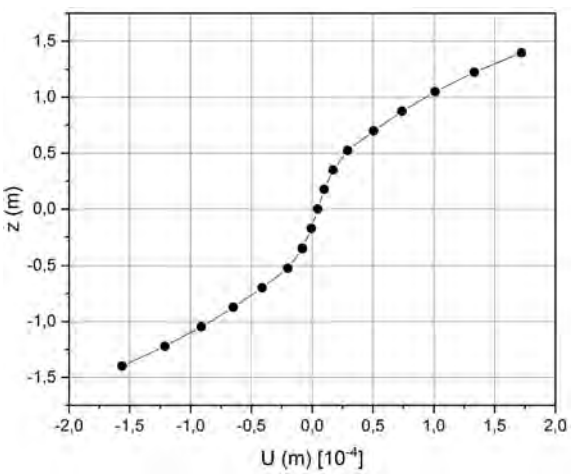

Figure 4. The variation of longitudinal displacement along the beam thickness.

The longitudinal displacement distribution along the beam thickness is presented in Fig. 5. The red and dark blue regions indicate the positive and negative maximum displacement values at the bottom and top surfaces along x-axis.

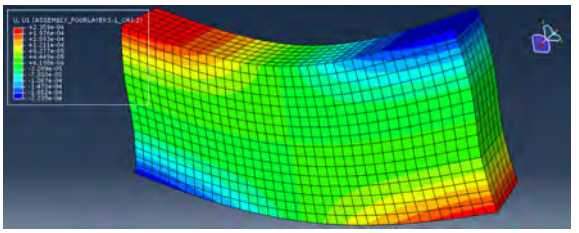

Figure 5. The longitudinal displacement distribution.

In the mid-plane, the longitudinal displacement values are close to zero as in the previous figure.

In Fig. 6, the variation of normal stress along the beam length is presented. The maximum value is obtained in the mid-point, and stress values are obtained as zero at both ends of the beam respectively.

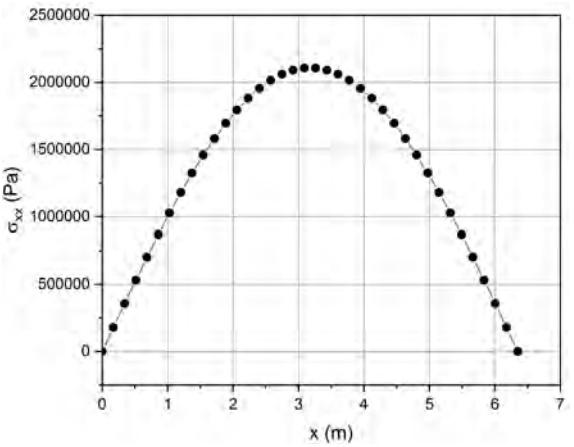

Figure 6. The variation of normal stress along the beam length.

In Fig. 7, the normal stress distribution along the beam length is presented. For the specific point where x=L/2 and z=h/4, the stress values are close to the analytical solution. The positive and negative stress values correspond to the tensile and compressive stresses.

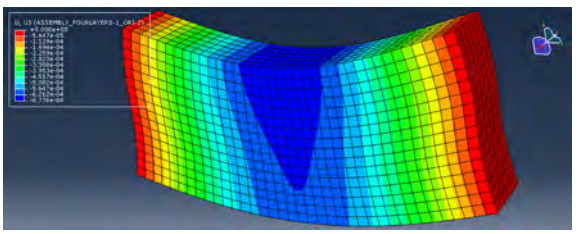

Figure 7. The normal stress distribution.

In Fig. 8, the variation of shear stress along the beam thickness is presented. At the bottom and top surfaces, the shear stresses are obtained as zero in accordance with the shear deformation beam theory, and the maximum stress value is obtained in the mid-plane.

In Fig. 9, the shear stress distribution along the beam thickness is presented. The stress values are close to the refe-

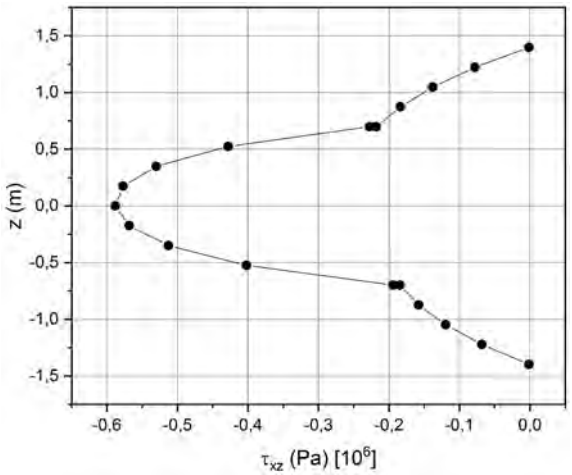

Figure 8. The variation of the shear stress along the beam thickness.

rence values where x=L/4, and z=0. The colored regions are similar with the curve obtained by the analytical solution in the previous figure.

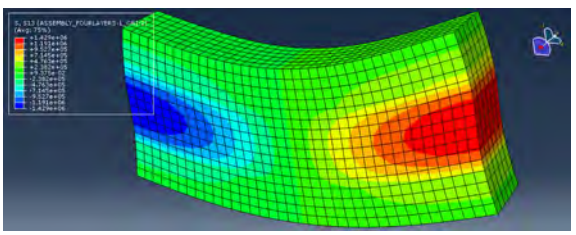

Figure 9. The shear stress distribution.

CONCLUSION

In this study, the bending analysis of a composite beam under a uniform sinusoidal load is performed. By use of the proposed model, the results are compared with the analytical and CAE solutions of the previous studies. When the results are compared with the reference values, the percentage values of errors are obtained as 1.88% and 1.85% for vertical and longitudinal displacements, 2.55% and 1.91% for the shear and normal stresses, respectively. Thus, it is concluded from the results that there is a significant decrease in percentage error values from 11.8% and 11.3% for the longitudinal displacement and shear stress values, whereas there is a minor change from 2.2% and 3.9% for the vertical displacement and normal stress values when compared with the analytical solution of Karaçam, 2005. In the future works, the dynamic analysis can be performed in order to obtain the natural frequencies and buckling loads. Additionally, the static and dynamic analyses can be expanded by taking various design parameters into consideration such as loading type, stacking sequence, layer thickness and boundary conditions.

CONFLICT OF INTEREST

The author deny any conflict of interest.

REFERENCES

1. Sankar BV. An elasticity solution for functionally graded beams. Composites Science and Technology. 2001;61:689–696.
2. Sayyad AS, Ghugal YM, Borkar RR. Flexural analysis of fibrous composite beams under various mechanical loadings using refined shear deformation theories. Composites: Mechanics, Computations, Applications. An International Journal. 2014;5(1):1–19.
3. Sayyad AS, Ghugal YM, Naik NS. Bending analysis of laminated composite and sandwich beams according to refined trigonometric beam theory. Curved and Layered Structures. 2015;2:279–289.
4. Pimenta RJ, Queiroz G, Diniz SMC. Reliability–based design recommendations for sinusoidal–web beams subjected to lateral–torsional buckling. Engineering Structures. 2015;84:195-206.
5. Pagani A, Yan Y, Carrera E. Exact solutions for static analysis of laminated, box and sandwich beams by refined layer–wise theory. Composites Part B. 2017;13:62–75.
6. Jiaoa P, Borchania W, Soleimania S, McGraw B. Lateral–torsional buckling analysis of wood composite I–beams with sinusoidal corrugated web. Thin–Walled Structures. 2017;119:72-82.
7. Liu T, Li ZM, Jin S. Nonlinear bending analysis of anisotropic laminated tubular beams based on higher–order theory subjected to different kinds of distributed loads. International Journal of Pressure Vessels and Piping. 2018;163:23–35.
8. Dorduncu M. Stress analysis of laminated composite beams using refined zigzag theory and peridynamic differential operator. Composite Structures. 2019;218:193–203.
9. Karakoti A, Kar VR. Deformation characteristics of sinusoidally–corrugated laminated composite panel – A higher–order finite element approach. Composite Structures. 2019;216:151–158.
10. Pandey N, Gadade AM. Static response of laminated composite beam subjected to transverse loading. Materials Today: Proceedings. 2019;16:956–963.
11. Sobhy M. Levy solution for bending response of FG carbon nanotube reinforced plates under uniform, linear, sinusoidal, and exponential distributed loadings. Engineering Structures. 2019;182:198–212.
12. Wang M, Xu YG, Qiao P, Li ZM. A two–dimensional elasticity model for bending and free vibration analysis of graphene–reinforced composite laminated beams. Composite Structures. 2019;211:364–375.
13. Pathirana S, Qiao P. Local buckling analysis of periodic sinusoidal corrugated composite panels under uniaxial compression. Composite Structures. 2019;220:148–157.
14. Pathirana S, Qiao P. Elastic local buckling of periodic sinusoidal corrugated composite panels subjected to in–plane shear. Thin–Walled Structures. 2020;157:107134.
15. Zaboon JK, Jassim SF. Bending of cross–ply laminated composite beams with various boundary conditions and loading. Materials Today: Proceedings. 2022;61:930-934.

16. Zhu S, Zhang YX, Lee CK. Experimental investigation of flexural behaviours of hybrid engineered cementitious composite beams under static and fatigue loading. Engineering Structures. 2022;262:114369.

17. Soldatos KP, Tımarcı, T. A unified formulation of laminated composite, shear deformable five–degrees–of–freedom cylindrical shell theories. Composite Structures. 1993;25:165–171.

18. Jones RM. Mechanics of Composite Materials. McGraw–Hill New York; 1975.

19. Karama M, Afaq KS, Mistou S. Mechanical behaviour of laminated composite beam by the new multi–layered laminated composite structures model with transverse shear stress continuity. International Journal of Solids and Structures. 2003;40:1525–1546.

20. Karama M, Harb BA, Mistou S, Caperaa S. Bending, buckling and free vibration of laminated composite with a transverse shear stress continuity model. Composites Part B. 1998;29(B):223–234.

21. Karacam F, Timarci T. Bending of cross–ply beams with different boundary conditions. UNITECH Gabrovo–05 International Scientific Conference, Gabrovo, Bulgaria, November. 2005;2:137–142.

Research Article
Hittite Journal of Science and Engineering, 2023, 10 (4) 309–315
ISSN NUMBER: 2148–4171
DOI: 10.17350/hjse19030000320

Nucleobase-Modified Microgels Synthesized via Microfabrication Technology for DNA Adsorption

Kemal Cetin[1,2]
[1] Necmettin Erbakan University, Faculty of Engineering, Department of Biomedical Engineering, Konya, Türkiye.
[2] Necmettin Erbakan University, Science and Technology Research and Application Center (BITAM), Konya, Türkiye.

ABSTRACT

DNA isolation is a crucial procedure since DNA-based assays have great importance in molecular biology, biochemistry and biomedical applications. The objective of this study is to fabricate micron-sized hydrogels as adsorbents for DNA. Poly(2-hydroxyethyl methacrylate-co-glycidyl methacrylate) microgels were synthesized by free radical polymerization in the presence of N,N'-methylenebisacrylamide as a crosslinker, in the microholes of a microstencil array chip. Then, adenine was immobilized to microgels through the epoxy groups of glycidyl methacrylate. Scanning electron microscopy and Fourier transform infrared spectroscopy were employed to investigate the chemical and morphological characterizations of the microgels. The findings of the experiments demonstrate that the microgels had a cylindrical shape, were of uniform size, and had a height and diameter of around 500 µm. Observation of aromatic C=C peak confirmed the existence of adenine ligand in the microgel structure. Adsorption studies were carried out to determine the optimal conditions for DNA adsorption of nucleobase-immobilized microgels. After initially increasing, the quantity of DNA adsorbed onto the microgels reached a saturation level at a DNA concentration of around 2.0 mg/mL. The maximum adsorption was 38.54 mg/g microgels for an initial DNA concentration of 2.0 mg/mL in the optimum medium pH and temperature. DNA adsorption capabilities are shown to not significantly decline in recurrent adsorption-desorption cycles. As a result of the findings, adenine-immobilized microgels were demonstrated to be a viable option for DNA adsorption. Additionally, as a reference for future research, this study highlights the benefits of microfabrication technology, such as its simplicity of use in fabricating adsorption materials with the desired size, shape, and uniformity.

Keywords:
Adsorption; DNA; Hydrogels; Microfabrication; Microgels; Nucleobase

Article History:
Received: 2023/06/06
Accepted: 2023/10/12
Online: 2023/12/31

***Correspondence to**: Kemal Çetin, kcetin@erbakan.edu.tr*

This article has been checked for similarity.

INTRODUCTION

DNA isolation/extraction from biological samples is a fundamental and significant process in biochemistry, molecular biology, forensics, clinical analysis, and DNA-based biomedical applications [1–3]. DNA isolation has great potential usage in gene therapy, the treatment of autoimmune diseases, DNA vaccination, pathogen detection, biosensor applications and so on [2,4–6]. The importance of DNA and DNA isolation has made it crucial to develop DNA isolation procedures and techniques. The need for innovative methods is demonstrated by the fact that conventional ones need time-consuming steps like centrifugation and precipitation as well as the usage of harmful chemicals for both the environment and human health [7].

Hydrogels are polymeric structures with a high-water retention capacity in their 3D matrices. They are insoluble in water due to their physically or/and chemically cross-linked structure, but instead, exhibit high swelling capacity [8,9]. Because of their promising properties, hydrogels have been used in various applications in biochemistry, biotechnology, and biomedical engineering. For example, they can be used in tissue engineering owing to their tissue-like swelling properties and biocompatibility, in drug delivery systems because of their ability to load the desired amount of drug and injectable formulation, and in affinity chromatography for the separation of biomolecules like proteins due to allowing modifications such as ligand immobilization of the polymer matrix [10–12].

Cite as:
K. CETIN, "Nucleobase-Modified Microgels Synthesized via Microfabrication Technology for DNA Adsorption" Hittite Journal of Science and Engineering, vol. 10, no. 4, pp. 309–315, 2023. doi:10.17350/hjse19030000320

Microfabrication processes have been widely employed in electronics and bioelectronics in order to fabricate micro-electro-mechanical systems (MEMS) including sensors, cantilevers, microreservoirs, micropumps, rotors, channels, valves, and so on [13]. Besides electronics, micro- and nanofabrication methods are potentially powerful tools to improve devices in biotechnology and biochemical processing, such as miniaturized chromatography systems, lab-on-a-chip devices, and microreactors [14,15]. Microengineered hydrogels, one of the significant products of microfabrication, have great potential in tissue engineering and drug delivery systems due to their abilities of mimicking the physical, mechanical, and biological features of natural tissues and organs [16–18].

Recently, Wu et al. studied the effect of metal ions such as Na^+, Mg^{2+}, Ca^{2+}, Mn^{2+} and Zn^{2+} the on the adsorption of both single-stranded DNA (ssDNA) and double-stranded DNA (dsDNA) onto microplastics and they reported that the transition metals, i.e., Mn^{2+} and Zn^{2+}, showed a higher adsorption capacity than Mg^{2+} for both dsDNA and ssDNA [19]. For DNA extraction and amplification, Wang et al. immobilized Ti^{4+} on magnetic composite microspheres and reported the extraction ability as 84 ± 4 μg/mg [20]. By polymerizing HEMA with N-methacryloyl-L-tryptophan which is a hydrophobic ligand, Çorman et al. synthesized two different types of hydrophobic cryogels: the first is poly(2-hydroxyethyl methacrylate-N-methacryloyl-l-tryptophan) [P(HEMA-MATrp)] cryogel, and the second is P(HEMA-MATrp) particles embedded PHEMA cryogel [21]. Maximum adsorption of DNA on p(HEMA-MATrp) cryogel and p(HEMA-MATrp) embedded PHEMA composite cryogel were found to be 15 mg/g and 38 mg/g polymer, respectively. The results showed that embedding hydrophobic microparticles showed higher adsorption capacity compared to hydrophobic cryogels [21]. Zandieh et al. studied on adsorption of DNA oligonucleotides onto microplastics in the absence and presence of metal ions and reported that polyethylene terephthalate and polystyrene showed the highest DNA adsorption efficiency [22]. Wang et al. prepared self-assembled zinc meso-tetra(4-pyridyl)porphyrin for DNA adsorption and adsorption of single-stranded DNA shoed higher efficiency compared to duplex DNA [23]. In another study, Meng et al developed a biosensor based on adsorption of DNA on polydopamine nanoparticles via different metal ions including $Na^{+,}$ K^+, Mg^{2+} and Ca^{2+} coordination and detection limit in various biological samples including serum was provided as <1 nM target DNA [24]. Muñoz et al. investigated the effect of homonuclear boron bonds on the adsorption of DNA nucleobases using quantum-mechanics calculations and concluded that the adsorption is improved by homonuclear bonds in the boron nitride nanosheets [25].

In this study, microfabrication technology was used to synthesize micro-engineered hydrogels, i.e., microgels with a height and diameter of around 500 μm. Microgels were produced in the microholes of a microstencil array chip (MAC) by free-radical polymerization of 2-hydroxyethyl methacrylate (HEMA) and glycidyl methacrylate (GMA) while N, N'-methylenebisacrylamide (MBA) was employed as a crosslinker. Investigating the effects of medium pH, initial DNA concentration, adsorption time, and ambient temperature on the adsorption capacity of microgels allowed for the identification of the optimal DNA adsorption conditions.

MATERIAL AND METHODS

Materials

HEMA, DNA (D3159, from herring sperm), GMA, ammonium persulfate (APS), MBA, and N,N,N',N'-tetramethyl ethylene diamine were purchased from Sigma Chemical Co. (St. Louis, MO, USA). Direct-Q 3 UV; Merck Millipore, Burlington, MA, USA system provided deionized water (DI Water) throughout the duration of the experimental research.

Fabrication of Microgels

Microgels prepared with the aid of a MAC are described as follows: Firstly, MBA (0.1% w/v) was dissolved in deionized (DI) water. HEMA:GMA ratio was adapted from an earlier study [26]. After adding HEMA (2.25 mL) and GMA (0.50 mL) to the MBA solution, it was magnetically stirred for 15 min. After APS (28.96 mg) was dissolved in the mixture, TEMED (11.4 μL) was added. Following the addition of ethanol (4 mL), the solutions were stirred once more and nitrogen bubbled for 5 min. The mixture was carefully put on a MAC. After 3 hours of polymerization at 60 °C, it was terminated at 4 °C, and microgels were collected.

Immobilization of Adenine onto Microgels

0.1 M of adenine solution was prepared in DI water : dioxane (1:1 v/v) and microgels were added into this mixture then the immobilization reaction was performed at 80°C by shaking for 24 h [27].

Characterization Studies

Prior to the Attenuated Total Reflection–Fourier Transform Infrared (ATR–FTIR) analysis, microgels were firstly freeze-dried at –110 °C for 24 h in a freeze-drying unit (Labogene Coolsafe Touch, Denmark). Using a Thermo Scientific Nicolet iS20 FTIR-ATR spectrophotometer (USA), FTIR spectra of the microgels were obtained in the wavelength range from 4000 to 500 cm^{-1} through 32 repeated scans at a 4 cm^{-1} resolution. Before the sample test, background measurements were made, which were automatically subtracted from the sample re-

sults. The overall shape and dimensions of the freeze-dried microgels were examined using an optical microscope (Olympus SZ6, Japan). To discuss the morphology of the microgels, a ZEISS GeminiSEM 500 field emission scanning electron microscope (FE-SEM) (Germany) was used.

Adsorption Studies

DNA adsorption capability of microgels was investigated in a batch experiment setup. The following conditions were studied to determine the optimal conditions for DNA adsorption of the microgels. The effects of medium pH (4-9) and temperature (4-45 °C), as well as the effects of initial DNA concentration (0.25-4.0 mg/mL) and adsorption time (2.5-60 min) on DNA adsorption capacity of microgels were investigated. DNA concentrations were determined at 260 nm using a UV-visible spectrophotometer and the amount of adsorbed DNA was evaluated via the Equation 1:

$$Q = \frac{(c_0 - c_f)v}{w} \quad (1)$$

where Q (mg/g dry microgel) is the adsorption capacity. The initial and final concentrations of DNA (in mg/mL) are shown by the symbols C_0 and C_f before and after the adsorption process, respectively. W is the dried microgel mass in g, and V is the volume of the DNA solution in mL.

RESULTS AND DISCUSSION

General shape and size of the microgels were evaluated via optical microscopy. As shown in Fig.1, microgels exhibit cylindrical shapes with the highest size of around 400–500 µm. Surface morphology of the microgels were revealed using FE-SEM as shown in Fig. 2. Microgels exhibit, in general, homogenous porous microstructure.

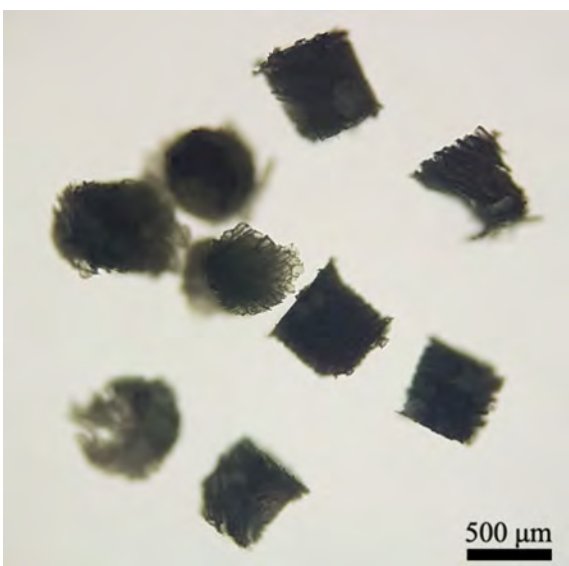

Figure 1. Optical microscopy images of the microgels

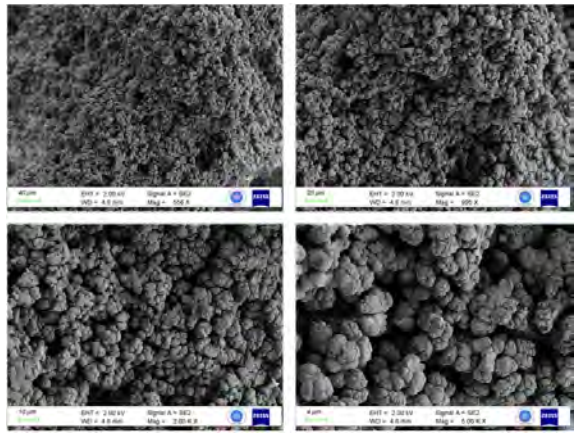

Figure 2. FE-SEM images of the microgels

We employed the Fourier transform infrared (FT-IR) spectroscopy approach to analyze the chemical composition of both plain and immobilized microgels (Fig. 3). The common bands were given at about 3400 cm^{-1}, 1710 cm^{-1}, and 2968 and 2946 cm^{-1}, respectively, for the -OH, C-H (aliphatic) and C=O bonds [26]. The C=C peaks at 1637 cm^{-1} have relatively low intensities, which supports polymerization.

The almost absence of C=C peaks around 1630 cm-1 confirms the polymerization [28]. Besides these, aromatic C=C peak indicates the existence of adenine ligand.

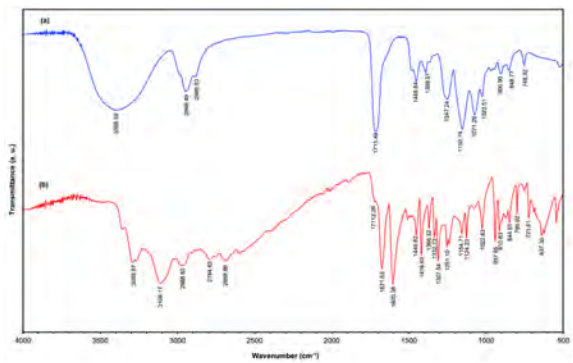

Figure 3. FT-IR spectra of the (a) P(HEMA-GMA) and (b) P(HEMA-GMA)-Adenine microgels

Fig. 4 depicts how medium pH affects the adsorption of DNA by the microgels. At pH 7.0, the adsorption capacity was at its maximum while declined at more alkaline and more acidic pH regions. Decrements in adsorption capacities were observed for pH 4.0 and pH 9.0 by about 18% and 23%, respectively, compared to the one in pH 7.0. This indicates that the interaction between adenine and thymine was weakened in acidic and basic environments by the presence of hydronium or hydroxy ions [29].

Fig. 5 presents the effect of adsorption time on the DNA adsorption by the microgels. Although the rate of DNA ad-

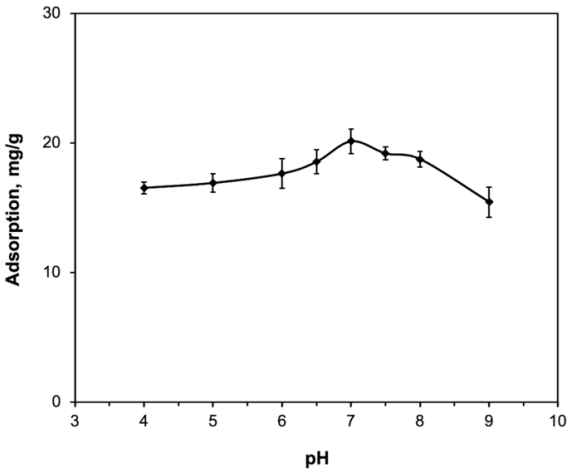

Figure 4. The adsorbed amount of DNA at various pH values (Temperature: 25 °C; initial DNA concentration: 0.5 mg/mL)

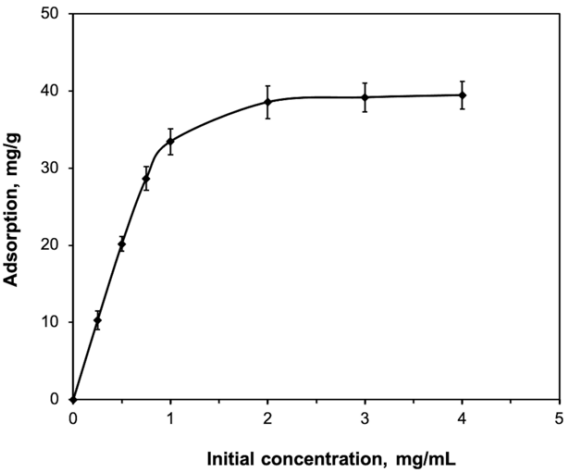

Figure 6. The adsorbed amount of DNA at various DNA concentrations (Running buffer: pH 7.0 phosphate; temperature: 25 °C)

sorption was initially high, it started to decline after only 2.5 min, and equilibrium adsorption was attained upto 5 min. As a result, for the optimal adsorption capacity, ligand and analyte molecules need a short interaction time. It is clear that the interaction between DNA molecules and microgels had a high affinity since microgels might reach their maximum adsorption capacity in just 5 min. This is mostly due to the fact that microgels include adenine molecules as ligands, which is consistent with the literature [7]. Additionally, DNA molecules can quickly reach and interact with the active regions of the gel matrix because of the hydrophilic nature of hydrogels [30].

As it is seen in Fig. 6, there was an increment in the adsorption capacity as the initial concentration of DNA increased. At an initial DNA concentration of 0.5 mg/L, the adsorption capacity of microgels was 20.18 mg/g, whereas, at an initial DNA concentration of 1.0 mg/mL, it reached up to 38.54 mg/g. At a DNA concentration of around 2.0 mg/L, the adsorption process approached a plateau level, i.e., 38.54 mg/g. Even if the initial concentration value of DNA was exceeded, DNA adsorption has reached a dynamic equilibrium value because all active adenine ligands in the microgels were occupied with analyte molecules, i.e. DNA. Similar results have been observed in previous DNA adsorption studies [24,31,32].

As shown in Fig. 7, it can be observed that the adsorption capacity slightly increased as the temperature raised. One possible explanation is that as the temperature increased, the DNA double helix structure may partially expanded, facilitating easier interaction between the ligand and nucleotides [7].

A comparison of the adsorption capacity and duration of adsorption process of the microfabricated microgels with those of some other adsorbents reported in literature is listed in Table 1. Considering the fast kinetics of the DNA adsorption of the microgels, it is predicted that these newly designed microgels may be a good alternative in DNA adsorption.

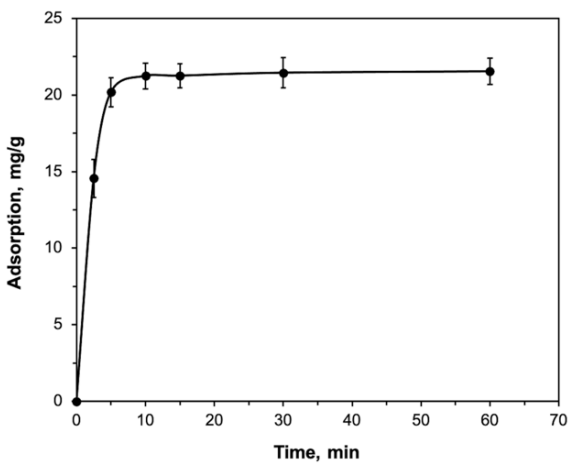

Figure 5. The adsorbed amount of DNA at various adsorption time (Running buffer: pH 7.0 phosphate; temperature: 25 °C; initial DNA concentration: 0.5 mg/mL)

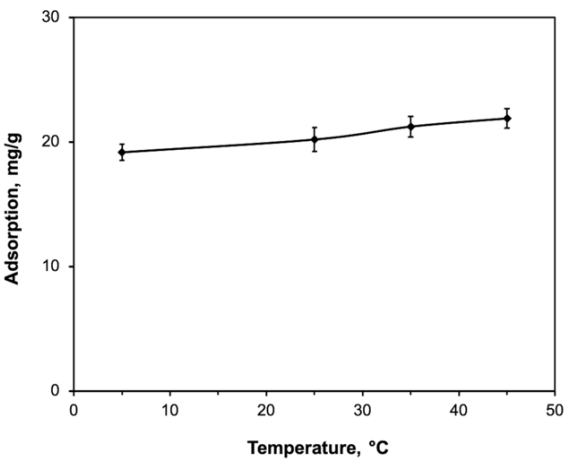

Figure 7. The adsorbed amount of DNA at various temperature values (Running buffer: pH 7.0 phosphate; initial DNA concentration: 0.5 mg/mL)

Table 1. Comparison of the DNA adsorption capacities of numerous adsorbents.

Adsorbent	Adsorption capacity	Adsorption time (min)	Ref.
Hemoglobin modified magnetic nanocomposites (NCs)	27.9 mg/g	15	[1]
Co(II) immobilized poly(GMA-EDMA) cryogels	33.81 mg/g	30	[5]
Aminosilane-modified magnetic nanoparticles (NPs)	4.7 mg/g	40	[33]
Ethylenediamine functionalized poly(glycidyl methacrylate) beads	90.4 µg/g	-	[34]
P(HEMA-(l)-histidine methyl ester)	13.5 mg/g	-	[35]
Silica–magnetite NCs	43.1 mg/g	8	[36]
Triethylamine modified poly(GMA-EDMA) monoliths	21.54 mg/mL	-	[37]
Cibacron Blue F3GA-attached poly(hydroxyethyl methacrylate)	32.5 mg/g	120	[38]
Zirconia magnetic NCs	53.5 mg/g	5	[39]
Magnetic polyaniline/maghemite NCs	75.2 mg/g	10	[40]
P(HEMA-MATrp) cryogels	3.53 mg/g	60	[21]
P(HEMA-MATrp) microbeads in PHEMA cryogels	8.35 mg/g	60	[21]
Composite cryogels of cyanobacterial extracellular polymeric substances and PHEMA	2.4 mg/g	-	[41]
Fe^{3+} ions attached EPS–PHEMA composite cryogels	39.7 mg/g	-	[41]
Cu^{2+}-attached magnetite NPs embedded PHEMA cryogels	19.97 mg/g	120	[42]
16mer peptide modified poly(EDMA-GMA)	65.1 µg/g	5	[43]
Indium Tin Oxide NPs	28.5 nM	120	[44]
Magnetic Mesoporous Silica NPs	121.6 mg/g	>20 h	[45]
Microfabricated nucleobase-modified microgels	38.54 mg/g	10	This study

While a material's capacity to be reused has economic benefits, it is also vital to reducing the usage of single-use plastics from polluting the environment [46]. For this objective, the adsorption capabilities of the synthesized microgels were evaluated for their not only single-use but also repeated-use effects on DNA adsorption capability. Figure 8 illustrates how the adsorption capacity of the same microgels decreased after each use in comparison to the prior capacity. During the adsorption-desorption cycle, a decrease in the adsorption capacity of the adsorbent may be observed for various reasons including loss in the active site for the analyte molecules due to tear and/or wear in the adsorbent, precipitation on the adsorbent surface, low desorption efficiency and so on [47,48]. After five uses, it was found that the reduction was only 10% of the initial adsorption capacity, resulting a good recycling ability compared with the earlier studies [35,38,49].

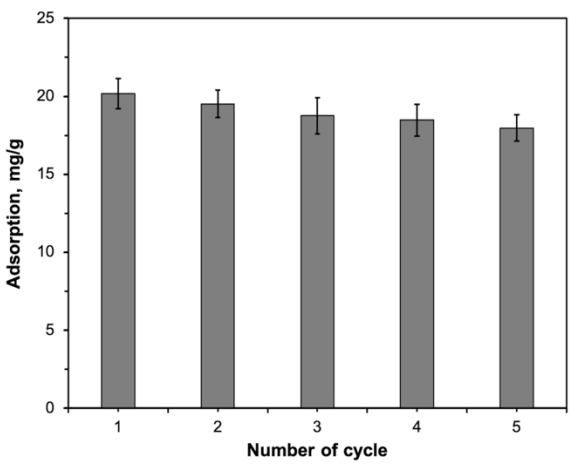

Figure 8. Reusability of the microgels (Running buffer: pH 7.0 phosphate; temperature: 25 °C; initial DNA concentration: 0.5 mg/mL)

CONCLUSION

In the microholes of a microstencil array chip, poly(2-hydroxyethyl methacrylate-co-glycidyl methacrylate) microgels were created by free radical polymerization in the presence of N,N'-methylenebisacrylamide as a crosslinker. Then, adenine was immobilized to microgels using glycidyl methacrylate's epoxy groups. At a DNA concentration of around 2.0 mg/mL, the amount of DNA adsorbed onto the microgels reached a saturation level after initially growing. The amount of adsorbed DNA apparently depends on the initial DNA concentration. At the optimal temperature and pH of the medium, the maximum adsorption was 20.18 mg/g and 38.54 mg/g microgels at initial DNA concentrations of 0.5 and 2.0 mg/mL, respectively. It has been demonstrated that DNA adsorption capacity was not noticeably decreased throughout repeated adsorption-desorption cycles. This study showed that adsorption materials of desired size, shape, and uniform size can be easily produced using the microfabrication technique.

CONFLICT OF INTEREST

Authors approve that to the best of their knowledge, there is not any conflict of interest or common interest with an institution/organization or a person that may affect the review process of the paper.

AUTHOR CONTRIBUTION

Kemal Cetin Methodology, Investigation, Visualization, Writing - original draft.

REFERENCES

1. Chen XW, Mao QX, Liu JW, Wang JH. Isolation/separation of plasmid DNA using hemoglobin modified magnetic nanocomposites as solid-phase adsorbent. Talanta 2012;100:107–12.
2. Fakurpur Shirejini S, Dehnavi SM, Jahanfar M. Potential of superparamagnetic iron oxide nanoparticles coated with carbon dots as a magnetic nanoadsorbent for DNA isolation. Chem Eng Res Des 2023;190:580–9.
3. Türkcan C, Akgöl S, Denizli A. Silanized polymeric nanoparticles for DNA isolation. Mater Sci Eng C 2013;33:4498–503.
4. Akrami M, Dehnavi SM, Barjasteh M, Jahanfar M. Synthesis and characterization of iron oxide/functionalized graphene oxide nanocomposites for highly efficient DNA isolation. Mater Sci Eng B 2023;292:116401.
5. Erol K. DNA adsorption via Co(II) immobilized cryogels. J

Macromol Sci Part A 2016;53:629–35.
6. Akgönüllü S, Denizli A. Recent advances in optical biosensing approaches for biomarkers detection. Biosens Bioelectron X 2022;12:100269.
7. Köse K. Nucleotide incorporated magnetic microparticles for isolation of DNA. Process Biochem 2016;51:1644–9.
8. Çetin K. Metal-Ion Assisted Imprinted Hydrogels For Recognition Of Lysozyme. Duzce Univ J Sci Technol 2021;9:545–55.
9. Şarkaya K, Yildirim M, Alli A. One-step preparation of poly(NIPAM-pyrrole) electroconductive composite hydrogel and its dielectric properties. J Appl Polym Sci 2021;138:50527.
10. Gopinathan J, Noh I. Click Chemistry-Based Injectable Hydrogels and Bioprinting Inks for Tissue Engineering Applications. Tissue Eng Regen Med 2018 155 2018;15:531–46.
11. Rizzo F, Kehr NS. Recent Advances in Injectable Hydrogels for Controlled and Local Drug Delivery. Adv Healthc Mater 2021;10:2001341.
12. Yang YJ, Mai DJ, Dursch TJ, Olsen BD. Nucleopore-Inspired Polymer Hydrogels for Selective Biomolecular Transport. Biomacromolecules 2018;19:3905–16.
13. Grayson ACR, Shawgo RS, Johnson AM, Flynn NT, Li Y, Cima MJ, vd. A BioMEMS review: MEMS technology for physiologically integrated devices. Proc IEEE 2004;92:6–21.
14. Chován T, Guttman A. Microfabricated devices in biotechnology and biochemical processing. Trends Biotechnol 2002;20:116–22.
15. Sohn LL, Schwille P, Hierlemann A, Tay S, Samitier J, Fu J, vd. How Can Microfluidic and Microfabrication Approaches Make Experiments More Physiologically Relevant Cell Syst 2020;11:209
16. Chung BG, Lee KH, Khademhosseini A, Lee SH. Microfluidic fabrication of microengineered hydrogels and their application in tissue engineering. Lab Chip 2011;12:45–59.
17. Yanagawa F, Sugiura S, Kanamori T. Hydrogel microfabrication technology toward three dimensional tissue engineering. Regen Ther 2016;3:45–57.
18. Coutinho DF, Sant S, Shakiba M, Wang B, Gomes ME, Neves NM, vd. Microfabricated photocrosslinkable polyelectrolyte-complex of chitosan and methacrylated gellan gum. J Mater Chem 2012;22:17262–71.
19. Robert Walker T, Wu L, Patel K, Zandieh M, Liu J. Promotion of DNA Adsorption onto Microplastics by Transition Metal Ions. Microplastics 2023, Vol 2, Pages 158-167 2023;2:158–67.
20. Wang X, Fei W, Zhou Z, Zhu M, Chang Y, Guo Q, vd. Immobilization of Multivalent Titanium Cations on Magnetic Composite Microspheres for Highly Efficient DNA Extraction and Amplification. ACS Appl Mater Interfaces 2023;15:42170–81.
21. Çorman ME, Bereli N, Özkara S, Uzun L, Denizli A. Hydrophobic cryogels for DNA adsorption: Effect of embedding of monosize microbeads into cryogel network on their adsorptive performances. Biomed Chromatogr 2013;27:1524–31.
22. Zandieh M, Patel K, Liu J. Adsorption of Linear and Spherical DNA Oligonucleotides onto Microplastics. Langmuir 2022;38:1915–22.
23. Wang J, Wang Z, Huang PJJ, Bai F, Liu J. Adsorption of DNA Oligonucleotides by Self-Assembled Metalloporphyrin Nanomaterials. Langmuir 2022;38:3553–60.
24. Meng Y, Liu P, Zhou W, Ding J, Liu J. Bioorthogonal DNA Adsorption on Polydopamine Nanoparticles Mediated by Metal Coordination for Highly Robust Sensing in Serum and Living Cells. ACS Nano 2018;12:9070–80.
25. Muñoz ADO, Escobedo-Morales A, Skakerzadeh E, Anota EC. Effect of homonuclear boron bonds in the adsorption of DNA nucleobases on boron nitride nanosheets. J Mol Liq 2021;322:114951.
26. Memmedova T, Armutcu C, Uzun L, Denizli A. Polyglycidyl methacrylate based immunoaffinity cryogels for insulin adsorption. Mater Sci Eng C 2015;52:178–85.
27. Yoshikawa T, Umeno D, Saito K, Sugo T. High-performance collection of palladium ions in acidic media using nucleic-acid-base-immobilized porous hollow-fiber membranes. J Memb Sci 2008;307:82–7.
28. Çetin K, Denizli A. Polyethylenimine-functionalized microcryogels for controlled release of diclofenac sodium. React Funct Polym 2022;170:105125.
29. Zhang D, Domke KF, Pettinger B, Zhang D, Domke KF, Pettinger B. Tip-Enhanced Raman Spectroscopic Studies of the Hydrogen Bonding between Adenine and Thymine Adsorbed on Au (111). ChemPhysChem 2010;11:1662–5.
30. Ullah F, Othman MBH, Javed F, Ahmad Z, Akil HM. Classification, processing and application of hydrogels: A review. Mater Sci Eng C 2015;57:414–33.
31. Üzek R, Uzun L, Şenel S, Denizli A. Nanospines incorporation into the structure of the hydrophobic cryogels via novel cryogelation method: An alternative sorbent for plasmid DNA purification. Colloids Surfaces B Biointerfaces 2013;102:243–50.
32. Zandieh M, Liu J. Transition Metal-Mediated DNA Adsorption on Polydopamine Nanoparticles. Langmuir 2020;36:3260–7.
33. Tanaka T, Sakai R, Kobayashi R, Hatakeyama K, Matsunaga T. Contributions of phosphate to DNA adsorption/desorption behaviors on aminosilane-modified magnetic nanoparticles. Langmuir 2009;25:2956–61.
34. Zhang HP, Bai S, Xu L, Sun Y. Fabrication of mono-sized magnetic anion exchange beads for plasmid DNA purification. J Chromatogr B 2009;877:127–33.
35. Perçin I, Sağlar E, Yavuz H, Aksöz E, Denizli A. Poly(hydroxyethyl methacrylate) based affinity cryogel for plasmid DNA purification. Int J Biol Macromol 2011;48:577–82.
36. Chiang CL, Sung CS, Chen CY. Application of silica–magnetite nanocomposites to the isolation of ultrapure plasmid DNA from bacterial cells. J Magn Magn Mater 2006;305:483–90.
37. Ongkudon CM, Danquah MK. Anion exchange chromatography of 4.2 kbp plasmid based vaccine (pcDNA3F) from alkaline lysed E. coli lysate using amino functionalised polymethacrylate conical monolith. Sep Purif Technol 2011;78:303–10.
38. Çimen D, Yilmaz F, Perçin I, Türkmen D, Denizli A. Dye affinity cryogels for plasmid DNA purification. Mater Sci Eng C 2015;56:318–24.
39. Saraji M, Yousefi S, Talebi M. Plasmid DNA purification by zirconia magnetic nanocomposite. Anal Biochem 2017;539:33–8.
40. Medina-Llamas JC, Chávez-Guajardo AE, Andrade CAS, Alves KGB, de Melo CP. Use of magnetic polyaniline/maghemite nanocomposite for DNA retrieval from aqueous solutions. J Colloid Interface Sci 2014;434:167–74.
41. Önal B, Odabaşı M. Design and application of a newly generated bio/synthetic cryogel column for DNA capturing. Polym Bull 2021;78:6011–28.
42. Ceylan Ş, Kalburcu T, Gedikli M, Odabaşı M. Application of Cu2+-attached Magnetite Nanoparticles Embedded Supermacroporous Monolithic Composite Cryogels for DNA Adsorption. Hacettepe J Biol Chem 2011;39:163–72.
43. Han Y, Forde GM. Single step purification of plasmid DNA using peptide ligand affinity chromatography. J Chromatogr B 2008;874:21–6.
44. Liu B, Liu J. DNA adsorption by indium tin oxide nanoparticles. Langmuir 2015;31:371–7.
45. Li X, Zhang J, Gu H. Adsorption and desorption behaviors of DNA with magnetic mesoporous silica nanoparticles. Langmuir

2011;27:6099–106.
46. Çetin K. Magnetic nanoparticles embedded microcryogels for bilirubin removal. Process Biochem 2022;112:203–8.
47. Altaf R, Lin X, Zhuang W qin, Lu H, Rout PR, Liu D. Nitrilotrismethylenephosphonate sorption from wastewater on zirconium-lanthanum modified magnetite: Reusability and mechanism study. J Clean Prod 2021;314:128045.
48. Suresh Kumar P, Ejerssa WW, Wegener CC, Korving L, Dugulan AI, Temmink H, vd. Understanding and improving the reusability of phosphate adsorbents for wastewater effluent polishing. Water Res 2018;145:365–74.
49. Bhar R, Kanwar R, Mehta SK. Surface engineering of nanoparticles anchored meso-macroporous silica heterostructure: An efficient adsorbent for DNA. Mater Chem Phys 2020;255:123541.

Research Article
Hittite Journal of Science and Engineering, 2023, 10 (4) 317–322
ISSN NUMBER: 2148–4171
DOI: 10.17350/hjse19030000321

Mechanical and Tribological Properties of Carbon Fiber/ Glass Fiber-Reinforced Epoxy Hybrid Composites Filled with Al_2O_3 Particles

Cantekin Kaykilarli[1,2] Aymurat Haydarov[1] Duygu Kose[1] Hasibe Aygul Yeprem[1]
[1] Yıldız Technical University, Metallurgical and Materials Engineering, Istanbul, Türkiye.
[2] Bursa Technical University, Metallurgical and Materials Engineering, Bursa, Türkiye.

ABSTRACT

In this study, we produced Aluminum oxide (Al_2O_3) reinforced carbon fiber and glass fiber reinforced polymer (CFRP, GFRP) composites and investigated mechanical and tribological properties. Al_2O_3 was dispersed in epoxy resin using a mechanical stirrer. The composites are produced via the hand lay-up method and dried at room temperature for 48 hours. The properties of composites were determined via Archimedes' method, flexural, impact, hardness and wear tests. The highest flexural strength and hardness were found at 946.3 MPa and 48.7 HBA for 3 wt.% Al_2O_3 reinforced CFRP, respectively. The highest impact strength was observed at 187.4 kJ/m^2 for an un-reinforced GFRP composite. The lowest Coefficient of Friction (COF) and wear depth was found 3 wt.% Al_2O_3 reinforced GFRP composites.

Keywords:
Aluminium oxide; CFRP; Epoxy; GFRP; Hardness; Impact strength

Article History:
Received: 2023/07/18
Accepted: 2023/10/10
Online: 2023/12/31

***Correspondence to**: Cantekin Kaykılarlı,*
E-mail: cantekin.kaykilarli@btu.edu.tr;
Phone +90 224 300 3573

This article has been checked for similarity.

Introduction

Polymers and their composites are used in many common and advanced engineering applications. They are becoming a good alternative to products made out of metal due to several attractive properties, including lightweight, high strength, ease of processing, low waste of material during manufacturing, and cost-effectiveness. As a result, major efforts have been made to use polymers in diverse industrial applications, using a variety of reinforcements, including fibers, to boost the physical and mechanical properties of the polymers. As a result, fiber-reinforced polymer matrix composites are extremely appealing due to their low friction coefficient, biodegradability, high strength, high stiffness, good corrosion resistance, and low weight. These materials are currently used in almost all aspects of daily life, from homes to aerospace applications(1-3).

Fiber-reinforced polymeric composites have become widely accepted for application in various sectors, including infrastructure, automotive, aerospace, and, most recently, oil and gas. Due to their high strengths and low densities, and ease of manufacture, polymers and their composites are being used more frequently. When compared to traditional metallic systems, these materials are appealing due to two key properties. They can be customized to have stacking sequences that offer high strength and stiffness in directions of heavy loading, despite having a relatively low density. Composite materials are made of resin and reinforcement that is chosen for the application and the desired mechanical qualities (4-7).

The reinforcement of fiber-reinforced materials is chosen from carbon, glass, basalt, wood, paper or aramid, while the matrix is selected from various resins (epoxy, polyester, phenolic, vinyl ester, etc.) While the matrix encloses and protects the fibers, the fibers generally act as the primary load-bearing element. Matrices serve as load-transfer components between the fibers, shielding the structure from adverse environmental situations like high temperatures and humidity(8, 9).

Carbon fiber and glass fiber-reinforced polymer (CFRP/GFRP) composites have been frequently used in the aviation and space industry. As a result of their outstanding qualities, including their high strength, flexibility and stiffness, low weight, and excellent fatigue resistance. Glass fibers (GFs) work well under high tensile stress but aren't strong enough for compression

Cite as:
C. KAYKILARLI, A. HAYDAROV, D. KOSE and H.A. YEPREM, "Mechanical and Tribological Properties of Carbon Fiber/Glass Fiber-Reinforced Epoxy Hybrid Composites Filled with Al2O3 Particles" Hittite Journal of Science and Engineering, vol. 10, no. 4, pp. 317–322, 2023. doi:10.17350/hjse19030000321

because of their fragile character. Conversely, plastic materials can handle compression loading very well but cannot resist high tension. The GFRP created by combining these two materials creates a composite material that can withstand compressive and tensile loads. The use of GFRP composites in thermal, electrical and sound insulation, sporting equipment, boat and ship construction, aerospace applications, automotive, and sheet molding compounds is growing as a result of these features. Carbon fibers (CFs) are carbon-based fibers with typical properties such as high tensile strength and stiffness, low weight, high-temperature tolerance, low thermal expansion and great chemical resistance. CFRP composite materials are being used in a growing variety of aircraft components. In comparison to other types of fibers, CFs have a higher success rate and are light in nature(8-11).

High toughness and strength, adhesion, durability at low and high temperatures, low moisture absorption, thermal stability, high chemical, electrical and corrosion resistance, low shrinkage, good adherence to a variety of substrates, and simplicity of production are only a few of the advantages of epoxy. Epoxy is widely used in various products, including adhesives, construction, petrochemicals, automotive, aeronautics, semiconductor encapsulation, biocompatible implants, protective coatings, laminates and electric and electronic systems. Epoxy has excellent properties but a fragile structure, poor tribological performance, limited flame resistance, and low crack strength. The two main methods used to solve the problem are chemical treatment and the addition of second-phase particles (12-18).

Three main ways are often used to evolve the features of polymer matrix composites: the kind of polymer, the types of particles and fibers, and the interface between fibers. By incorporating fillers (such as Aluminum Oxide (Al_2O_3), Titanium Oxide (TiO_2), WC, SiC, and Graphite) into epoxy, the mechanical characteristics of epoxy are improved without changing the glass transition temperature. Al_2O_3 is widely used in the electronics, chemistry, chemical engineering, and aerospace industries due to its exceptional mechanical properties, chemical stability, excellent thermal properties, cost-effectiveness, good corrosion resistance, and enormous electrical properties. However, this material's fracture durability precludes its use in critical structural applications. (13, 14, 19-21).

Some recent works have studied GFRP/CFRP composites reinforced with Al_2O_3. Asi et al.(22) prepared Al_2O_3 (0, 2.5, 7.5, 10, 12.5 and 15 wt.%) reinforced GFRP composites and investigated the mechanical properties. They observed that the tensile strength decreased with the increasing wt.%Al_2O_3. Al_2O_3-reinforced GFRPs' tensile strengths are lower than the unreinforced GFRP composite. However, the highest bending strength was found in a 10 wt.% Al_2O_3 reinforced GFRP composite, and an increase of approximately 33% occurred compared to the unreinforced specimen. Mohanty et al.(23) fabricated nano-Al_2O_3 (0, 1, 2, 3, 4 and 5 wt.%) reinforced Glass/Carbon fiber epoxy composites and investigated composites' mechanical behaviour. They determined that composites' tensile strength decreases with the reinforcement of Al_2O_3. Raju et al.(24) produced GFRP reinforced with Al_2O_3 (0, 5, 7.5 and 10 wt.%) composites and analyzed mechanical and tribological behaviour. They observed that Al_2O_3 reinforced enhanced composites' tensile strength (254 to 352 MPa), hardness (63 to 72 Shore-D) and wear resistance. Nayak et al.(25) prepared $Al_2O_3/SiO_2/TiO_2$ (10 wt.%) reinforced GFRP composites and investigated mechanical properties. The highest hardness and impact energy were found for Al_2O_3-reinforced GFRP composites. Patel et al.(26) prepared Al_2O_3 and SiC (5 wt.%) nanoparticles reinforced GFRP and studied tribological features of the composites. As a result of the wear tests, the lowest wear loss was found in Al_2O_3-reinforced GFRP composites at all applied normal loads and sliding speeds. Zhang et al.(27) focused on the tribological properties of the nano-Al_2O_3 (2, 4, 6, 8 and 10 wt.%) reinforced CFRP composites it produces. Based on their research, they found that reinforcing 4 wt.% Al_2O_3 decreased the rate of wear and the Coefficient of Friction (COF) by 74.7 % and 65.5 %, respectively when compared to the unreinforced CFRP. Kaybal et al.(28) researched mechanical strength of the nano-Al_2O_3 (1, 2, 3, 4 and 5 wt.%) reinforced CFRP. According to this study, the tensile strength and flexural strength reach the highest values with 2 wt.% Al_2O_3 reinforcement.

In the present investigation, we were produced hybrid (Al_2O_3-GFs/CFs) reinforced epoxy matrix composites via the hand lay-up method. This study aims to obtain the optimum reinforcement amount to achieve the produced composites' highest mechanical and tribological properties.

MATERIALS AND METHOD

The epoxy resin (Epikote Resin 828 Lvel) is used with the hardener (Epikure Curing Agent 866) to produce composites. The mixing ratio for epoxy resin and curing agent is 3:1, respectively. Twill CFs (200 gr/m^2, fiber diameter: 7μm, laminate thickness: 0.327 mm) and twill GFs (200 gr/m^2, laminate thickness: 0.15 mm) were used. Al_2O_3 powders (Eti Aluminum, +98.5%, particle size:-100 mesh, Bulk Angle:32-36°, Cas:1344-28-1) are used as reinforcement.

In this study, we used the same production route to fabricate varying composites. Firstly, Al_2O_3 was dispersed in epoxy resin for 4 min using a mechanical stirrer. CFs and GFs were cut to the size of 250 mm length and 250 mm

width. The epoxy curing agent is added to the Al_2O_3-epoxy mixture. The mixture was applied to CFs and GFs with a brush and after that, the composite was cured at room temperature for 48 hours. In this procedure, 4-layer hybrid composites were produced; the GFs-reinforced samples' thickness is approximately 2.2 mm and the thickness of the CFs-reinforced samples is about 1.1 mm. The composition of composites with reinforcement and sample codes are given in Table 1. While generating the sample code (XY), X represents the type of fiber (C: CFs and G: GFs) in the composite and Y represents the amount of Al_2O_3 (wt.%) in the composite.

Table 1. Sample codes and composition of composites

Sample Code	Epoxy:Fiber (wt.% ratio)	Fiber Type	Al_2O_3 (wt.%)
Co	1:1	CFs	-
C3			3
C5			5
C7			7
Go		GFs	-
G3			3
G5			5
G7			7

The epoxy matrix composites' densities were determined according to Archimedes' method in an ethanol medium and mean values were calculated based on three measurements. The fabricated samples were machined to Charpy impact test (l:80 mm x w:10 mm x t:4 mm), flexural strength (l:80 mm x w:10 mm x t:4 mm) and Barcol hardness test by the respective ISO 179-2, ISO 178-3 and ISO 59, respectively. We used a Devotrans Charpy Impact Tester for the impact test, AVK MH1/AS-102 for the 3-point bend test (The maximum load cell capacity: 500 kp) and Barcol Impressor for the Barcol hardness test. Images were taken from the fracture surfaces of the specimens after the impact testing with the Leica M-125 stereomicroscope. Reciprocating dry sliding wear tests were performed in a Bruker™ UMT2 Tribometer under 3 N force with 5 mm/s speed for 20 m of total distance by using 5 mm diameter chrome steel balls (ASTM E52100). Wear depths were obtained by examining the change in Z-axis values on the device. The processing and characterization of epoxy matrix composites are given schematically in Fig.1.

RESULTS AND DISCUSSION

Table 2 illustrates the density values of the composites. Relative density values for the produced specimens are between 94.05% and 80.27%. The relative densities of GFRP composites are always lower than CFRP composites. The highest relative density was observed in the C0 specimen. The relative density of CFRP composite specimens decreased with the reinforcement of Al_2O_3. Nayak et al.(29) prepared nano-Al_2O_3 (0.1, 0.3 and 0.7 wt.%) reinforced GFRP composites, and observed that an increasing Al_2O_3 amount increased the void content. Because of their higher viscosity, highly reinforced materials are more difficult to mix and are more likely to produce voids(30). Also, this could be because the entrapped gas could not get out of the epoxy matrix throughout the production and curing processes(29).

Table 2. Relative density of CFRP and GFRP composites.

Sample Code	Theroretical Density (g/cm³)	Relative Density (%)
Co	1.46	94.05
C3	1.5	90.95
C5	1.528	87.16
C7	1.551	85.01
Go	1.909	84.83
G3	1.946	80.27
G5	1.984	83.43
G7	1.850	84.06

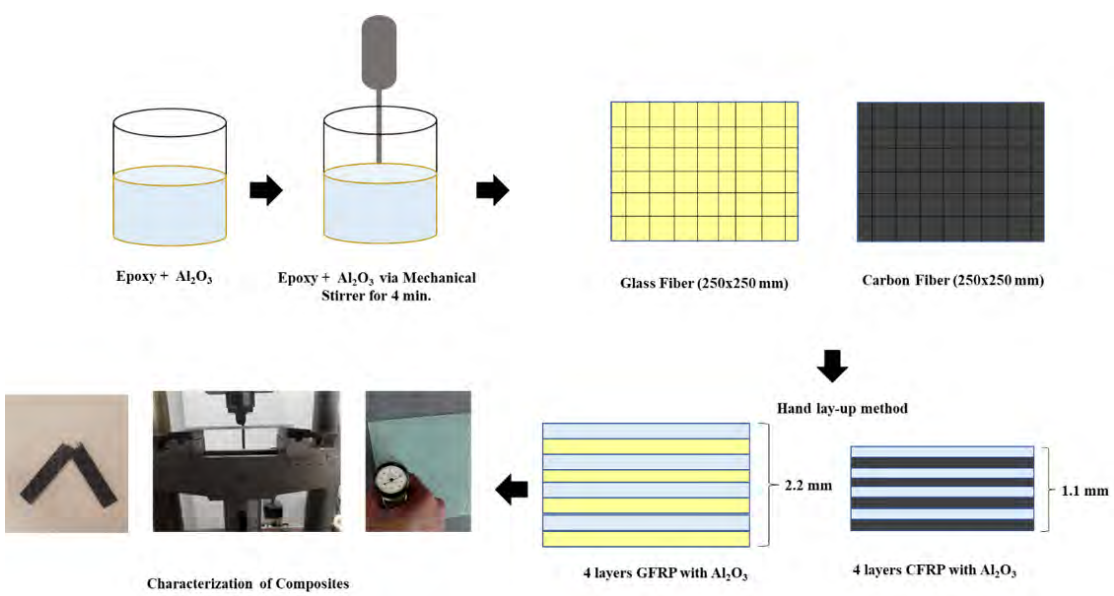

Figure 1. Processing and characterization of epoxy matrix composites

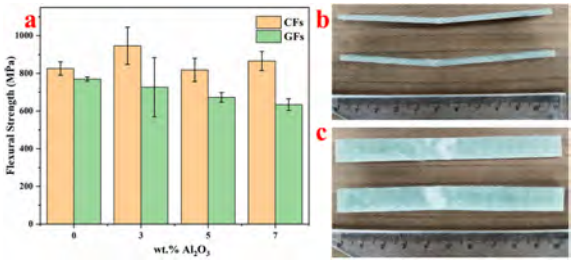

Figure 2. Flexural strength performance of epoxy matrix composites (a) flexural strength of the composites (b,c) image of specimens after testing

The 3-point bending test results of the composites are given in Fig. 2. The data shown are the average of three tests for each sample type. Flexural strength is determined between 946.3 and 634.1 MPa. The highest flexural strength values are obtained for 3 wt.% Al_2O_3 reinforced CFRP composites. With the addition of 3 wt.% Al_2O_3, the flexural strength increased by 15% compared to the unreinforced CFRP sample. However, Al_2O_3 reinforcement above these amounts affected the flexural strength adversely for CFRP composites. Unlike the CFRP, Al_2O_3 reinforcement decreased the flexural strength of GFRP composites and this decrease increased with increasing Al_2O_3 content. This is because as the Al_2O_3 content increases, the void content and Al_2O_3 particle agglomeration also increase, which can cause matrix swelling and the development of microcracks at the interface(29, 31). Moreover, the lower flexural properties may have been brought on by the filler's and epoxy resin matrix's poor interface bonding(22). Similar results are also available in the literature. Wang et al. prepared Al_2O_3 reinforced CFRP and analyzed flexural strength and they determined that the maximum flexural strength was 760 MPa with 15 g/m^2 (areal densities of Al_2O_3) Al_2O_3 reinforced composites(32). Asi et al. produced GFRP-filled Al_2O_3 particles and investigated flexural strength. They determined that the optimum wt.% Al_2O_3 amounts was 10%(22). These studies found that above the optimum amounts, flexural strength was deteriorating.

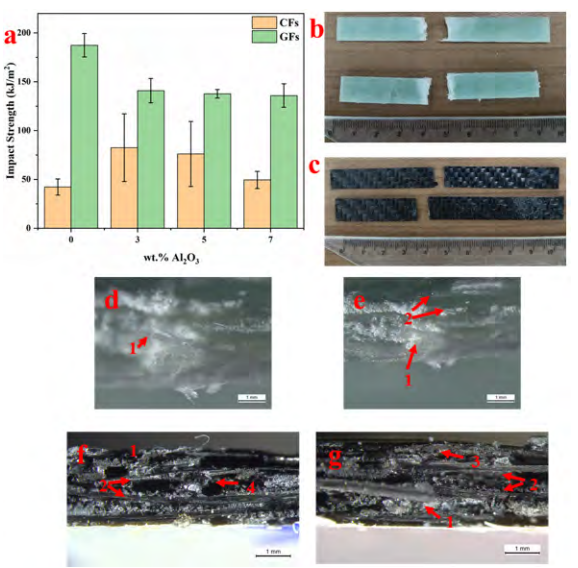

Figure 3. Impact performance of epoxy matrix composites (a) impact strength of GFRP/CFRP composites with varying wt.% Al_2O_3 (b,c) image of specimens after testing and stereomicroscope image of specimens after impact test (d) G0, (e) G5, (f) C0 and (g) C7

The results from the varying amounts of Al_2O_3 reinforcement on the composite from the Charpy impact test are illustrated in Fig. 3. The data shown are the average of three tests for each sample type. The impact strength is determined between 42.2 and 187.4 kJ/m^2. The highest impact strength was found in unreinforced GFRP, and there was a decrease in impact strength with Al_2O_3 reinforcement (Approximately 28% decrease with the reinforcement of 7 wt.% Al_2O_3). Compared to GFRP, CFRP showed much lower impact strength overall. On the other hand, there was a remarkable 80.22% increase in the impact strength of the CFRP with the addition of 3 wt.% Al_2O_3. Increasing the Al_2O_3 amount also had a negative effect on CFRP. The stereomicroscope images (Fig. 3 (d-g)) were shown the presence of fiber breaks (1), delamination (2), voids (3) and matrix breakage (4) in the fracture surfaces. Wang et al. prepared Al_2O_3-reinforced CFRP and investigated impact strength. They found that the optimum Al_2O_3 was 15 g/m^2 and with the increase of the reinforcement ratio to 20%, the impact strength decreased by approximately 16%(32).

Fig. 4 demonstrates the effect of Al_2O_3 for CFRP/GFRP composites on hardness behaviour. Hardness is obtained between 33.5 and 48.7 HBA. The maximum hardness value in both composite types was obtained in the samples reinforced with 3 wt.% Al_2O_3. Compared to the unreinforced samples, there was a 12.99% and 7% increase in hardness for CFRP and GFRP, respectively. Increasing the Al_2O_3 amount above 3 wt.% also had a negative effect on the hardness of both composite types. It's a general rule that the hardness of a material goes up as the filler increases. Fillers give epoxy resins their hardness, and as the amount of filler increases, so does the hardness of the epoxy(33). It was observed that agglomeration in CFRP composites decreased the impact and flexural strength with above 3 wt.% Al_2O_3; hence, a decrease in hardness is also observed. Similar results are also available in previous studies(33-35).

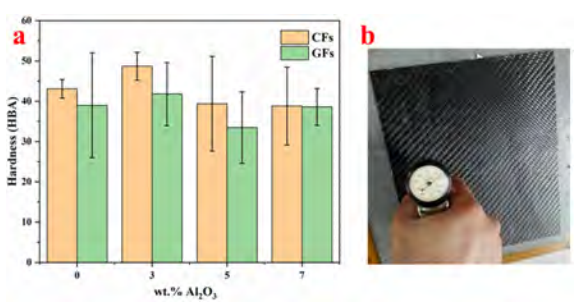

Figure 4. Hardness results of the composites (a) the hardness of composites with varying wt.% Al_2O_3 and (b) Barcoll hardness test view

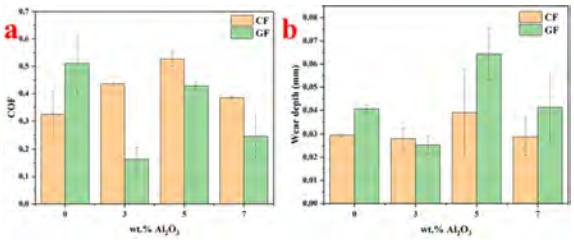

Figure 5. Wear test results of the composites (a) COF and (b) wear depth

The COF and wear depth of composites that originated from varying Al_2O_3 wt.% amounts are illustrated in Fig. 5. The average COF and wear depth values refer to at least three tests. The COF and wear depth values are between 0.1625-0.5264 and 0.0252-0.0642 mm, respectively. The composites' lowest COF and wear depth values were determined for the G3 samples. Studies in the literature show that the materials with the lowest COF and wear depth have the highest wear resistance (36-38). The highest COF was obtained for the C5 samples, and the maximum wear depth was observed G5 samples. In CFRP composites, adding Al_2O_3 increased the COF value compared to the unreinforced sample. In contrast, in GFRP composites, adding Al_2O_3 increased the COF value compared to the unreinforced sample. The lowest wear depth for both composite types was obtained in the samples reinforced with 3 wt.% Al_2O_3. Zhang et al. found the lowest COF and wear rate results for 4 wt.% nano-Al_2O_3 reinforced CFRP composites(27).

CONCLUSIONS

The GFRP and CFRP reinforced with Al_2O_3 composites are produced via the hand lay-up method and investigated the mechanical and tribological properties. The conclusions are as follows:

- The relative density of the composites generally decreased with Al_2O_3 reinforcement. Also, the relative densities of CFRP composites are higher compared to GFRP.
- The highest flexural strength values are obtained for 3 wt.% Al_2O_3 reinforced CFRP composites. Al_2O_3 reinforcement decreased the flexural strength of GFRP composites and this decrease increased with increasing Al_2O_3 amount.
- The highest impact strength was found in unreinforced GFRP, and there was a decrease in impact strength with Al_2O_3 reinforcement. On the other hand, there was an outstanding increase in the impact strength of the CFRP with the addition of 3 wt.% Al_2O_3.
- The maximum hardness value in both composite types were obtained in the samples reinforced with 3 wt.% Al_2O_3.
- The lowest COF and wear depth was found 3 wt.% Al_2O_3 reinforced GFRP composites.

As a result of the studies, it has been determined that the optimum Al_2O_3 ratio is 3 wt.%. Future research will focus on ensuring a more homogenous distribution of reinforcements in the epoxy as well as improved surface adherence between the reinforcement and the matrix.

CONFLICT OF INTEREST

Authors approve that to the best of their knowledge, there is not any conflict of interest or common interest with an institution/organization or a person that may affect the review process of the paper.

AUTHOR CONTRIBUTION

Cantekin Kaykilarli: Investigation, Characterization, Writing-Review&Editing
Aymurat Haydarov: Production, Characterization, Writing.
Duygu Kose: Production, Characterization, Writing.
Hasibe Aygul Yeprem: Investigation, Supervision, Writing-Review&Editing

REFERENCES

1. Sampathkumaran P, Seetharamu S, Thomas P, Janardhana M. A study on the effect of the type and content of filler in epoxy–glass composite system on the friction and slide wear characteristics. Wear. 2005;259(1-6):634-41.
2. Omrani E, Menezes PL, Rohatgi PK. State of the art on tribological behavior of polymer matrix composites reinforced with natural fibers in the green materials world. Engineering Science and Technology, an International Journal. 2016;19(2):717-36.
3. Kessler MR. Polymer matrix composites: A perspective for a special issue of polymer reviews. Polymer Reviews. 2012;52(3):229-33.
4. Basavarajappa S, Arun K, Davim JP. Effect of filler materials on dry sliding wear behavior of polymer matrix composites–a Taguchi approach. Journal of minerals and materials characterization and engineering. 2009;8(05):379.
5. El-Tayeb N, Gadelrab R. Friction and wear properties of E-glass fiber reinforced epoxy composites under different sliding contact conditions. Wear. 1996;192(1-2):112-7.
6. Kukureka S, Hooke C, Rao M, Liao P, Chen Y. The effect of fibre reinforcement on the friction and wear of polyamide 66 under dry rolling–sliding contact. Tribology International. 1999;32(2):107-16.
7. Zum Gahr K-H. Microstructure and wear of materials: Elsevier;1987.
8. Rajak DK, Wagh PH, Linul E. Manufacturing technologies of carbon/glass fiber-reinforced polymer composites and their properties: A review. Polymers. 2021;13(21):3721.
9. Karataş MA, Gökkaya H. A review on machinability of carbon fiber reinforced polymer (CFRP) and glass fiber reinforced polymer (GFRP) composite materials. Defence Technology. 2018;14(4):318-

26.
10. Ho K-C, Jeng M-C. Tribological characteristics of short glass fibre reinforced polycarbonate composites. Wear. 1997;206(1-2):60-8.
11. Fortin GY, Elbadry EA, Hamada H. Crashworthiness of recycled cardboard panels reinforced with hybrid columnar aluminum tube-GFRP rods. Polymer Composites. 2019;40(11):4215-27.
12. Domun N, Hadavinia H, Zhang T, Sainsbury T, Liaghat G, Vahid S. Improving the fracture toughness and the strength of epoxy using nanomaterials–a review of the current status. Nanoscale. 2015;7(23):10294-329.
13. Kaykılarlı C, Yeprem HA, Uzunsoy D. Mechanical and tribological characterization of graphene nanoplatelets/Al2O3 reinforced epoxy hybrid composites. Fullerenes, Nanotubes and Carbon Nanostructures. 2023:1-13.
14. Kesavulu A, Mohanty A. Compressive performance and thermal stability of alumina—graphene nanoplatelets reinforced epoxy nanocomposites. Materials Research Express. 2019;6(12):125329.
15. Naous W, Yu XY, Zhang QX, Naito K, Kagawa Y. Morphology, tensile properties, and fracture toughness of epoxy/Al2O3 nanocomposites. Journal of Polymer Science Part B: Polymer Physics. 2006;44(10):1466-73.
16. Wang ZZ, Gu P, Zhang Z, Gu L, Xu YZ. Mechanical and tribological behavior of epoxy/silica nanocomposites at the micro/nano scale. Tribology Letters. 2011;42:185-91.
17. Kumar V, Sinha SK, Agarwal AK. Tribological studies of epoxy composites with solid and liquid fillers. Tribology International. 2017;105:27-36.
18. Kangishwar S, Radhika N, Sheik AA, Chavali A, Hariharan S. A comprehensive review on polymer matrix composites: material selection, fabrication, and application. Polymer Bulletin. 2023;80(1):47-87.
19. Yadav P, Purohit R, Kothari A. Study of friction and wear behaviour of epoxy/nano SiO2 based polymer matrix composites-a review. Materials Today: Proceedings. 2019;18:5530-9.
20. Ouyang Y, Bai L, Tian H, Li X, Yuan F. Recent progress of thermal conductive ploymer composites: Al2O3 fillers, properties and applications. Composites Part A: Applied Science and Manufacturing. 2022;152:106685.
21. Kesavulu A, Mohanty A. Tribological characterization of graphene nanoplatelets/alumina particles filled epoxy hybrid nanocomposites. Journal of Applied Polymer Science. 2020;137(46):49518.
22. Asi O. Mechanical properties of glass-fiber reinforced epoxy composites filled with Al 2O3 particles. Journal of reinforced plastics and composites. 2009;28(23):2861-7.
23. Mohanty A, Srivastava VK, Sastry PU. Investigation of mechanical properties of alumina nanoparticle-loaded hybrid glass/carbon-fiber-reinforced epoxy composites. Journal of Applied Polymer Science. 2014;131(1).
24. Raju BR, Suresha B, Swamy RP, Kanthraju BSG. Investigations on mechanical and tribological behaviour of particulate filled glass fabric reinforced epoxy composites. 2013.
25. Nayak RK, Dash A, Ray B. Effect of epoxy modifiers (Al2O3/SiO2/TiO2) on mechanical performance of epoxy/glass fiber hybrid composites. Procedia materials science. 2014;6:1359-64.
26. Patel G, Chaudhary V, Mehta B, Swarnkar A, editors. Effect of Al2O3 and SiC nanoparticles on tribological properties of bi-directional glass fiber reinforced composites. IOP Conference Series: Materials Science and Engineering; 2021: IOP Publishing.
27. Zhang X. Study on the tribological properties of carbon fabric reinforced phenolic composites filled with nano-Al2O3. Journal of Macromolecular Science, Part B. 2017;56(8):568-77.
28. Kaybal HB, Ulus H, Demir O, Şahin ÖS, Avcı A. Effects of alumina nanoparticles on dynamic impact responses of carbon fiber reinforced epoxy matrix nanocomposites. Engineering Science and Technology, an International Journal. 2018;21(3):399-407.
29. Nayak RK. Influence of seawater aging on mechanical properties of nano-Al2O3 embedded glass fiber reinforced polymer nanocomposites. Construction and Building Materials. 2019;221:12-9.
30. Lewis JS, Barani Z, Magana AS, Kargar F, Balandin AA. Thermal and electrical conductivity control in hybrid composites with graphene and boron nitride fillers. Materials Research Express. 2019;6(8):085325.
31. Biswas S, Satapathy A. A study on tribological behavior of alumina-filled glass–epoxy composites using Taguchi experimental design. Tribology Transactions. 2010;53(4):520-32.
32. Wang Z, Huang X, Bai L, Du R, Liu Y, Zhang Y, et al. Effect of micro-Al2O3 contents on mechanical property of carbon fiber reinforced epoxy matrix composites. Composites Part B: Engineering. 2016;91:392-8.
33. Gbadeyan O, Kanny K, Turup Pandurangan M. Tribological, mechanical, and microstructural of multiwalled carbon nanotubes/short carbon fiber epoxy composites. Journal of Tribology. 2018;140(2):022002.
34. Megahed M, Fathy A, Morsy D, Shehata F. Mechanical performance of glass/epoxy composites enhanced by micro-and nanosized aluminum particles. Journal of Industrial Textiles. 2021;51(1):68-92.
35. Pani B, Chandrasekhar P, Singh S. Application of box-behnken design and neural computation for tribo-mechanical performance analysis of iron-mud-filled glass-fiber/epoxy composite and parametric optimization using PSO. Polymer Composites. 2019;40(4):1433-49.
36. Akçamlı N, Şenyurt B. Fabrication and characterization of in-situ Al3Ni intermetallic and CeO2 particulate-reinforced aluminum matrix composites. Ceramics International. 2021;47(15):21197-206.
37. Song J, Liu T, Shi H, Yan S, Liao Z, Liu Y, et al. Time-frequency analysis of the tribological behaviors of Ti6Al4V alloy under a dry sliding condition. Journal of Alloys and Compounds. 2017;724:752-62.
38. Öztürk A, Ezirmik K, Kazmanlı K, Ürgen M, Eryılmaz O, Erdemir A. Comparative tribological behaviors of TiN, CrN and MoNCu nanocomposite coatings. Tribology International. 2008;41(1):49-59.

Research Article
Hittite Journal of Science and Engineering, 2023, 10 (4) 323–329
ISSN NUMBER: 2148–4171
DOI: 10.17350/HJSE19030000322

Examination Of Perlite-Polymer Interface Interactions in Polypropylene-Based Composites via Several Compatibilizers

Çagrialp Arslan[1] Umit Tayfun[2] Mehmet Dogan[3]
[1]Bartin University, Textile Engineering, Bartin, Türkiye
[2]Bartin University, Basic Sciences, Bartin, Türkiye
[3]Erciyes University, Textile Engineering, Kayseri, Türkiye

ABSTRACT

The surface interaction between the polymer and the mineral additive is one of the most significant aspects influencing the efficiency of mineral-filled polymeric composites. In this work, three distinct compatibilizers were introduced to composites based on polypropylene (PP) and perlite to improve interactions between the constituents. On composites comprising 10% expanded perlite content, three different ratios of ethylene vinyl acetate copolymer (EVA), thermoplastic polyurethane elastomer (TPU), and maleic anhydride grafted polypropylene (MA-PP) compatibilizers were employed. The composite was produced using an approach designated melt blending followed by injection molding. The composites containing MA-PP compatibilizer possessed the most outstanding performance, according to the results of mechanical, physical, and dynamic mechanical evaluations and morphological characterizations. The investigated aspects indicated a rise in the composites containing 10 percent compatibilizer with the lowest adding amount, whereas performances declined at high compatibilizer contents. Along with these results, it was determined that the compatibilizers included in the PP/perlite composite system assisted in the fabrication of the composites by promoting the force values and melt flow rates identified during melt mixing. Following the test outcomes, MA-PP performed better than TPU and EVA in terms of compatibilizer efficiency. In general, it has been revealed that the selection of MA-PP compatibilizer in the manufacturing stages would offer benefits in terms of both simplicity of processing and mechanical strength where expanded perlite will be adopted as a natural filler for PP-based composites.

Article History:
Received: 2023/09/12
Accepted: 2023/11/28
Online: 2023/12/31

***Correspondence to**: Mehmet Doğan, Bartin University, Textile Engineering, 74100, Bartın, TÜRKİYE*
E-Mail: mehmetd@erciyes.edu.tr;
Phone: +90 352 207-66 66.

This article has been checked for similarity.

Keywords:
Mineral additive; Polymer composites; Expanded perlite; Compatibilizer; Polypropylene; Polymer processing

INTRODUCTION

Because they are inexpensive and straightforward to handle, minerals are frequently used as reinforcement for polymer-based substances. Due to the low degree of incompatibility between the natural mineral surface and the polymer phase, the incorporation of mineral additives in polymeric composites has several limitations despite benefits like low weight, low cost, and recyclability (1-5). As a practical option to address the compatibility difficulties, tuning the chemical nature of the matrix-filler interface via integration of compatibilizer leads to improved mechanical resistance of composite materials (6-10).

The amorphous volcanic silica glass known as perlite is a naturally formed mineral with a high level of water. This aluminosilicate may expand by thirty times its original volume after heating. The majority of the world's perlite reserves, or more than 50%, are in Türkiye. Similar to volcanic particulate minerals, expanded perlite powder was used as an additive for various polymeric matrices (6, 11, 12). Polymers compounded with perlite mineral include polyolefins, polyesters, elastomers, and copolymers based on various forms such as films, foams, resins, fabrics, and 3D parts. Table 1 summarizes the polymers and investigated properties by citing these research studies (13-51).

As indicated in Table 1, research works dealing with PP/perlite composites were performed in four studies which reported that incompatibility between inor-

Table 1. PER reinforced polymer composites in the literature.

Polymer matrix	Examined behavior	Reference number
Polyethylene (PE)	Thermal and mechanical	(13-19)
Polypropylene (PP)	Mechanical and processing	(20-23)
Polystyrene (PS)	Mechanical	(24, 25)
Polyvinylalcohol (PVA)	Thermal and mechanical	(26)
Acrylonitrile-butadiene-styrene (ABS)	Flame retardancy and mechanical	(27-29)
Polylacticacid (PLA)	Crystallinity and thermal stability	(30, 31)
Polyethyleneglycol (PEG)	Heat storage	(32)
Hydroxyapatite (HA)	Tissue engineering	(33, 34)
Polyaniline (PAn)	Electrical conductivity	(35)
Natural rubber	Odour-adsorbing	(36, 37)
Polyester fabrics	Acoustical	(38)
Polyphenylene sulphide (PPS)	Tribological	(39)
Polyurethane (PU)	Thermal insulation	(40-42)
Paraffin	Heat storage	(43, 44)
Epoxy resin	Ablative	(45-48)
Novalac resin	Tribological	(49)
Chitosan	Thermal stability	(50)
Polymethacrylicacid (PMAA)	Drug delivery	(51)
Butadiene rubber	Industrial goods	(52)

ganic perlite filler and organic PP phase influenced the mechanical behavior of composites negatively (20-23). Since the efficiency of maleic anhydride grafting is stated as the favored option for polymer composites (53-55), maleic anhydride grafted PP (PP-MA) was preferred as a compatibilizer. In addition to PP-MA, thermoplastic polyurethane (TPU) and ethyle-vinyl-acetate (EVA) were utilized to increase surface interactions in perlite-loaded PP composites attributed to their miscibility in the PP phase (56-59).

The interphase between additive and polymer phases plays a key role in the properties of composite materials attributed to physical and chemical aspects. The formation of interfacial interactions on the polymer-additive interface by integration of compatibilizers that can interact with both perlite and PP. For this reason, PP-MA, TPU, and EVA were compounded to enhance the interface adhesion of the inorganic perlite phase with organic PP matrix. Based on the findings of this study, performances of PP/perlite composites in terms of mechanical, morphological, processing, and melt-flow properties were compared to PP/EVA, PP/TPU, and PP/PP-MA composites involving perlite. Additionally, adding amount of perlite powder was investigated based on examined behaviors.

MATERIAL AND METHODS

Materials

PP with the trade name of Petoplen EH-251 was obtained from Petkim, İzmir, Türkiye. MA grafted PP was used as a compatibilizer with a commercial name Exxelor™ PO 1020 supplied by ExxonMobil, Texas, USA. The degree of grafting for PP-MA was indicated as a high graft level by the producer. Ester-based TPU (R130A85) was purchased from Ravago Petrochemicals, İzmir, Türkiye. The commercial name of EVA was Alcudia PA-461 supplied by Repsol S.A., Madrid, Spain. The vinyl acetate content of this EVA grade was 33%. According to their datasheets provided by producers, melting temperatures of EVA, TPU, and PP-MA polymers were 59 °C, 190 °C, and 162 °C, respectively.

Expanded perlite with a bulk density of 300–1000 g/cm^3 was supplied by Eti Maden, İzmir, Türkiye. The average particle size of PER was found to be 18 μm thanks to the particle size distribution curve shown in Fig. 1.

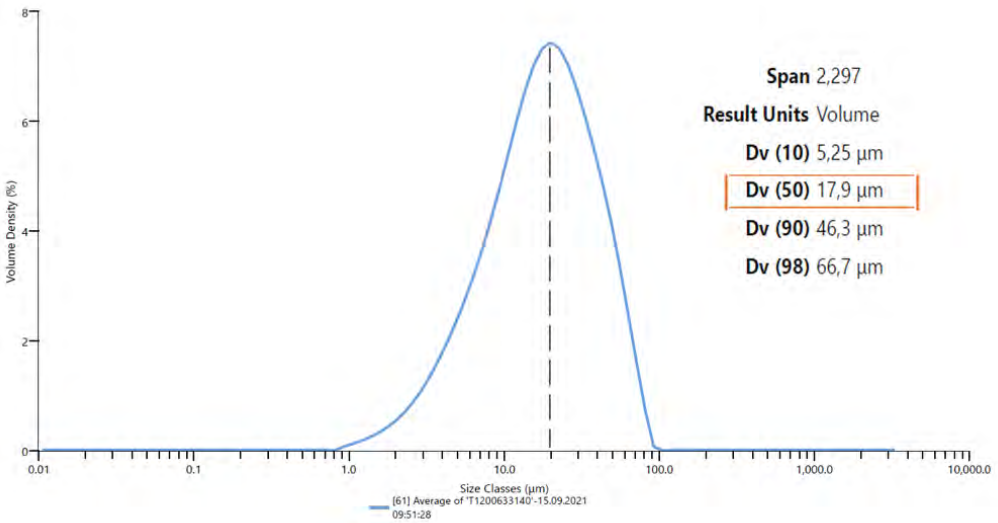

Figure 1. Particle size distribution curve of PER.

Composite Production

PP, TPU, PP-MA pellets, and PER powder were dried under vacuum at 80 °C for 2 h to remove moisture content before the compounding process. Composite samples were fabricated via Xplore MC15HT micro-extruder Adding amount of PER in composites was kept constant at 10% by weight. Three different concentrations for compatibilizers 10%, 20%, and 30% by weight were used. Processing temperature of 185°C, screew speed of 100 rpm, and mixing time of 4 min were applied during the melt-mixing process After the compounding step, dog-bone shaped test specimens with a dimension of 7.6 × 2.0 × 80 mm^3 for the tensile test and the dimension of 45 × 20 × 6.5 mm^3 for the D-type Shore hardness test was shaped using Daca injection molding instrument.

Characterization Techniques

Malvern Panalytical Mastersizer 3000 was used to evaluate the particle size of PER powder. Xplore Instruments program was employed to quantify force values throughout the extrusion process. The screw force values in the melt were determined using the micro-compounder's rheological software as a function of mixing time. Lloyd LR 30 K universal tensile testing machine was used for tensile properties of composites. Shore hardness values were determined using the Zwick R5LB041 digital hardness device. MFI measurements were performed via Coesfield Meltfixer LT using a 2.16 kg standard load at 185°C. The JSM-6400 Electron Microscope, a field emission scanning electron microscope, was used for observing the morphological characteristics of composite materials. A small coating of gold was applied to the surfaces of the cracked samples from the tensile test to establish conductive surfaces.

RESULTS AND DISCUSSION

Force Measurements

According to Fig. 2, force vs. time graphs demonstrate that PER additions elevated mixing force values due to powder incorporation boosted shear force as a result of increased melt viscosity throughout the extrusion operation. Compatibilizer inclusions with 10% content yielded lower force values compared to the PP/PER composite. The inclusion of EVA yielded a remarkable reduction in force values of PP/PER, whereas higher force values were obtained by TPU and PP-MA additions compared to the PP/PER EVA sample. Before high-scale production stages, this metric offers experimental data for planning manufacturing on the cost of fabricating the resultant composite materials. Since lower force data were recorded in compatibilizer-included composites relative to the force values of the PP/PER sample, the production of PER-filled PP composites can be carried out more economically in the presence of EVA, PP-MA, and TPU.

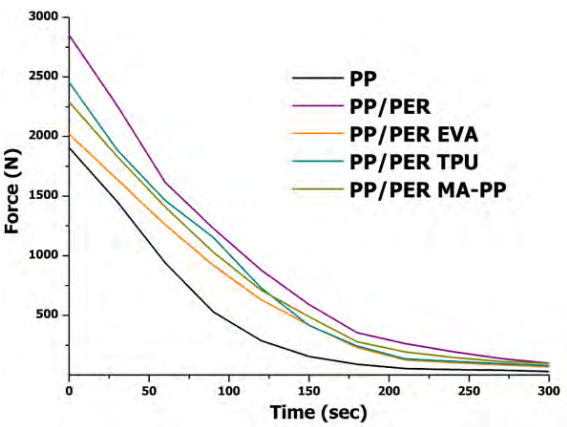

Figure 2. Force vs. time curves of PP and composites.

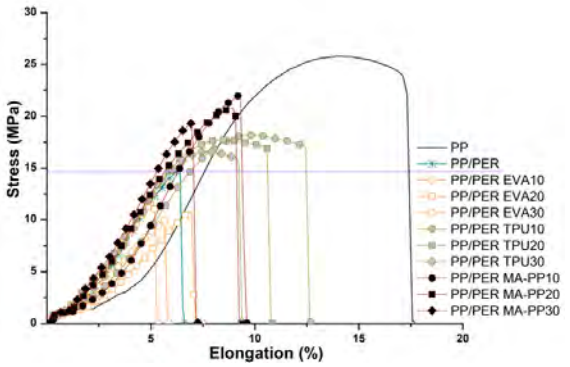

Figure 3. Stress vs. strain curves of composites.

Tensile Properties

Fig. 3 depicts tensile stress vs. percent strain curves. Tensile test data for PP and its composites, which include tensile strength, strain at break, and tensile modulus parameters are illustrated in Fig. 4.

The unfilled PP displayed ductile behavior according to its stress vs. strain curve in Fig. 3 in which necking behavior was observed. Since there was no necking property at the ultimate strength value. On the contrary, brittle characteristic was obtained after the incorporation of PER. Additionally, tensile stress and strain exhibited dramatic decline by PER addition. Using TPU as a compatibilizer caused to increase in the ductile behavior of composites stem from its high-strain elastomeric property whereas integration of PP-MA showed no effect on the brittle form of PP/PER.

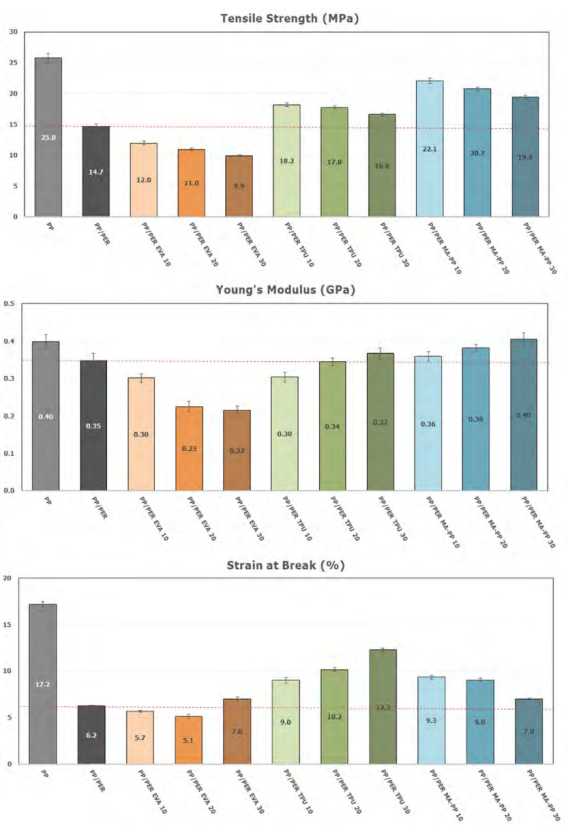

Figure 4. Tensile test data of samples.

Fig. 4 implied that EVA addition to the PP/PER system reduced tensile strength and Young's modulus parameters as well as strain values. As a common result, an increase in compatibilizer concentration resulted in a decline in the tensile strength of composites. TPU and MA-PP exhibited higher strength values compared to the PP/PER sample. The greatest tensile strength performance was achieved as PER-containing composites compounded with PP-MA compatibilizer since MA graft on PP structure enhanced compatibility between PER and polymer interface (55, 60).

Based on Young's modulus data, EVA displayed the worst performance among compatibilizers since remarkable reductions in modulus were observed. Conversely, TPU and PP-MA additions showed a positive effect on the modulus parameter of PP/PER. Young's modulus of composites enhanced as the added amount of compatibilizer increased

TPU-incorporated composites displayed a remarkable increase in percentage strain parameters attributed to the well-known high elongation behavior of TPU elastomer. PP/PER EVA composites gave the lowest results in terms of tensile strain.

Hardness Results

D-type Shore hardness data of unfilled PP and PER-filled PP composites are listed in Table 2. There were no significant differences in hardness measurement results compared to the reference material (PP). The shore hardness of PP displayed a slight increase with the addition of PER powder. Since EVA has an elastomeric nature, its

Table 2. Shore hardness results of composites.

Sample code	Hardness (Shore D)
PP	77.0 ± 0.1
PP/PER	77.5 ± 0.1
PP/PER EVA 10	76.5 ± 0.1
PP/PER EVA 20	76.0 ± 0.1
PP/PER EVA 30	75.0 ± 0.1
PP/PER TPU 10	78.0 ± 0.1
PP/PER TPU 20	78.5 ± 0.1
PP/PER TPU 30	79.5 ± 0.1
PP/PER MA-PP 10	77.5 ± 0.1
PP/PER MA-PP 20	77.5 ± 0.1
PP/PER MA-PP 30	78.0 ± 0.1

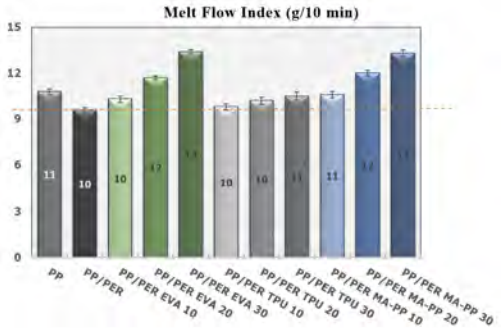

Figure 5. MFI data of samples.

integration into the PP/PER composite system resulted in reductions in the Shore D hardness of composites. On the contrary, TPU inclusions yielded improvement in hardness results despite it has elastomeric characteristics. The main reason for this observation might be the higher Shore D value of TPU with respect to PP. Similarly, PP-MA addition led to an increase in the Shore D parameter of the PP/PER composite.

Melt-flow Behaviors

Melt-flow index analysis is widely employed in thermoplastics for assessing the viscosity of molten polymers. Fig. 5 depicts the MFI characteristics of PP and related composites. When compared to unfilled PP, PER-incorporated composite possessed a lower MFI value. The rising quantity of MFI was found to be notable for composite samples containing a higher percentage of compatibilizers. TPU-loaded composites gave lower MFI values that were very similar to that of PP/PER. MFI specifications for composites were found to be in a limited spectrum while compared to unfilled PP as an overall finding regarding the melt-flow behavior of PER-loaded PP composites.

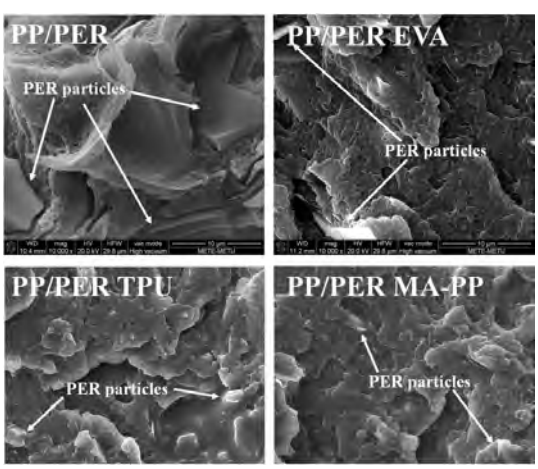

Figure 6. SEM micro-images of composites.

Morphological Analysis

The morphological study of composite samples was accomplished using SEM micro-images, which are illustrated in Fig. 6. Large gaps between PER particles and the PP matrix were detected in the SEM micrograph of PP/PER. The presence of compatibilizers donated strong adhesion and dispersion homogeneity in composite morphology. The formation of large gaps between phases was found to disappear after the inclusion of EVA as well as TPU. Similar to other compatibilizers, introducing PP-MA caused enhanced surface adhesion and distribution quality of PER according to the SEM image in Fig. 6. The result offered visible confirmation for improvements in associated composite performances pointed out in previous chapters.

CONCLUSION

One of the most crucial factors affecting the performance of mineral-filled polymeric composites is the surface interaction between the polymer and the mineral additive. In this research study, three different compatibilizers were used to enrich the interactions between phases in perlite-containing polypropylene (PP) composites. For this purpose, three different ratios of ethylene vinyl acetate copolymer (EVA), thermoplastic polyurethane elastomer (TPU), and maleic anhydride grafted polypropylene (MA-PP) compatibilizers were used on composites containing 10 percent expanded perlite mineral. Melt mixing followed by injection molding processes were used as the composite production process. In light of the findings obtained after mechanical, physical, and dynamic mechanical analysis and morphological characterizations, composites containing MA-PP compatibilizer showed the best performance. In the composites containing 10 percent compatibilizer with the lowest adding amount, an improvement was observed in the investigated properties, and a decrease in performances was detected at high compatibilizer concentrations. In addition to these findings, it was observed that the force values and melt flow rates measured during melt mixing, compatibilizers-introduced into the PP/perlite composite system facilitated the processing of the composites. According to the test results, the performance ranking among compatibilizers was found to be MA-PP > TPU > EVA. As a general conclusion, it has been evaluated that the preference of MA-PP compatibilizer in the production stages where expanded perlite will be used as a natural filler in PP-based composites will provide advantages in terms of both ease of processing and mechanical strength.

ACKNOWLEDGEMENT

The authors wish to thank Prof. Teoman Tinçer for his permission to work in his laboratory at the Chemistry Department of Middle East Technical University.

CONFLICT OF INTEREST

Authors approve that to the best of their knowledge, there is not any conflict of interest or common interest with an institution/organization or a person that may affect the review process of the paper.

AUTHOR CONTRIBUTION

Çağrıalp Arslan: Methodology, Software, Validation, Writing- original draft. Ümit Tayfun: Data curation, Visualization, Investigation, Writing- review and editing. Mehmet Doğan: Supervision, Conceptualization.

References

1. Xanthos M. Modification of polymer mechanical and rheological properties with functional fillers. Functional Fillers for Plastics. 2005:17-38.
2. Kıralp S, Özkoç G, Çamurlu P, Doğan M, Baydemir Tuncay B. Modern Çağın Malzemesi Plastikler, ODTÜ Yayıncılık, Ankara, 2007.
3. Mazumdar S. Composites Manufacturing: Materials, Product, and Process Engineering: CRC Press; 2001.
4. Billingham N. Plastics additives Edited by R. Gachter and H. Müller, Hanser Verlag, Munich, 1991.
5. Mastura M, Noryani M. Mineral-filled Composite: A Review on Characteristics, Applications, and Potential Materials Selection Process. Mineral-Filled Polymer Composites. 2022:25-43.
6. Liang J-Z. Reinforcement and quantitative description of inorganic particulate-filled polymer composites. Composites part B: engineering. 2013;51:224-32.
7. Dike AS, Yilmazer U. Mechanical, thermal and rheological characterization of polystyrene/organoclay nanocomposites containing aliphatic elastomer modifiers. Materials Research Express. 2020;7(1):015055.
8. Ansari M, Ismail H. Effect of compatibilisers on mechanical properties of feldspar/polypropylene composites. Polymer-Plastics Technology and Engineering. 2009;48(12):1295-303.
9. Donnet J. Nano and microcomposites of polymers elastomers and their reinforcement. Composites Science and Technology. 2003;63(8):1085-8.
10. Drelich J, Miller J. A critical review of wetting and adhesion phenomena in the preparation of polymer-mineral composites. Mining, Metallurgy & Exploration. 1995;12:197-204.
11. Çoban O, Yilmaz T. Volcanic particle materials in polymer composites: a review. Journal of Materials Science. 2022;57(36):16989-7020.
12. Ciullo PA. Industrial minerals and their uses: a handbook and formulary: William Andrew; 1996.
13. Atagür M, Sarikanat M, Uysalman T, Polat O, Elbeyli İY, Seki Y, et al. Mechanical, thermal, and viscoelastic investigations on expanded perlite–filled high-density polyethylene composite. Journal of Elastomers & Plastics. 2018;50(8):747-61.
14. Öktem GA, Tincer T. Preparation and characterization of perlite-filled high-density polyethylenes. I. Mechanical properties. Journal of applied polymer science. 1994;54(8):1103-14.
15. Öktem GA, Tincer T. Preparation and characterization of perlite-filled high-density polyethylenes. II. Thermal and flow properties. Journal of Applied Polymer Science. 1994;54(8):1115-22.
16. Öktem GA, Tincer T. A study on the yield stress of perlite-filled high-density polyethylenes. Journal of materials science. 1993;28:6313-7.
17. Sahraeian R, Hashemi S, Esfandeh M, Ghasemi I. Preparation of nanocomposites based on LDPE/Perlite: mechanical and morphological studies. Polymers and Polymer Composites. 2012;20(7):639-46.
18. Sahraeian R, Esfandeh M. Mechanical and morphological properties of LDPE/perlite nanocomposite films. Polymer Bulletin. 2017;74:1327-41.
19. Heidari BS, Davachi SM, Sahraeian R, Esfandeh M, Rashedi H, Seyfi J. Investigating thermal and surface properties of low-density polyethylene/nanoperlite nanocomposites for packaging applications. Polymer Composites. 2019;40(7):2929-37.
20. Mattausch H, Laske S, Cirar K, Flachberger H, Holzer C, editors. Influence of processing conditions on the morphology of expanded perlite/polypropylene composites. AIP Conference Proceedings; 2014: American Institute of Physics.
21. Özdemir F. Perlit İçeriğinin Odun Plastik Kompozitlerin Yanma Dayanımına Etkisi. Bartın Orman Fakültesi Dergisi. 2020;22(3):852-60.
22. Spoerk M, Sapkota J, Weingrill G, Fischinger T, Arbeiter F, Holzer C. Shrinkage and warpage optimization of expanded-perlite-filled polypropylene composites in extrusion-based additive manufacturing. Macromolecular materials and engineering. 2017;302(10):1700143.
23. Mattausch H, Laske S, Hohenwarter D, Holzer C, editors. The effect of mineral fillers on the rheological, mechanical and thermal properties of halogen-free flame-retardant polypropylene/expandable graphite compounds. AIP Conference Proceedings; 2015: AIP Publishing.
24. de Oliveira AG, Jandorno Jr JC, da Rocha EBD, de Sousa AMF, da Silva ALN. Evaluation of expanded perlite behavior in PS/Perlite composites. Applied Clay Science. 2019;181:105223.
25. de Oliveira AG, da Rocha EBD, Jandorno Jr JC, de Sousa AMF, da Silva ALN. Evaluation of thermoforming potential of polystyrene/perlite composites. Polymer Bulletin. 2023:1-13.
26. Tian H, Tagaya H. Dynamic mechanical property and photochemical stability of perlite/PVA and OMMT/PVA nanocomposites. Journal of materials science. 2008;43:766-70.
27. Çelen U, Balçik Tamer Y, Berber H. The potential use of natural expanded perlite as a flame retardant additive for acrylonitrile-butadiene-styrene based composites. Journal of Vinyl and Additive Technology. 2023.
28. Alghadi AM, Tirkes S, Tayfun U. Mechanical, thermo-mechanical and morphological characterization of ABS based composites loaded with perlite mineral. Materials Research Express. 2019;7(1):015301.
29. Angelopoulos PM, Kenanakis G, Viskadourakis Z, Tsakiridis P, Vasilopoulos KC, Karakassides MA, et al. Manufacturing of ABS/expanded perlite filament for 3D printing of lightweight components through fused deposition modeling. Materials Today: Proceedings. 2022;54:14-21.
30. Tian H, Tagaya H. Preparation, characterization and mechanical properties of the polylactide/perlite and the polylactide/

montmorillonite composites. Journal of Materials Science. 2007;42:3244-50.
31. Aksoy E., Tirkeş S., Tayfun U., Tirkeş S., Expanded perlite mineral as a natural additive used in polylactide-based biodegradable composites. Turkish Journal of Science & Technology 2023; DOI: 10.55525/tjst.1282216.
32. Zhang X, Wen R, Tang C, Wu B, Huang Z, Min X, et al. Thermal conductivity enhancement of polyethylene glycol/expanded perlite with carbon layer for heat storage application. Energy and Buildings. 2016;130:113-21.
33. Güngör SK. Pumice and perlite co-substituted hydroxyapatite: Fabrication and characterization. MANAS Journal of Engineering. 2020;8(2):132-7.
34. Karip E, Muratoğlu M. A study on using expanded perlite with hydroxyapatite: Reinforced bio-composites. Proceedings of the Institution of Mechanical Engineers, Part H: Journal of Engineering in Medicine. 2021;235(5):574-82.
35. Arsalani N, Hayatifar M. Preparation and characterization of novel conducting polyaniline–perlite composites. polymer international. 2005;54(6):933-8.
36. Masłowski M, Miedzianowska J, Strzelec K. Hybrid straw/perlite reinforced natural rubber biocomposites. Journal of Bionic Engineering. 2019;16:1127-42.
37. Rattanaplome T, Pornprasit P, Chantaramee N, editors. The Potential of Perlite as an Odour-Adsorbing Fillers in Natural Rubber Vulcanizates. Macromolecular Symposia; 2015: Wiley Online Library.
38. Karaca E, Omeroglu S, Akcam O. Investigation of the effects of perlite additive on some comfort and acoustical properties of polyester fabrics. Journal of Applied Polymer Science. 2016;133(16).
39. Sahin AE, Cetin B, Sinmazcelik T. Investigation of mechanical and tribological behaviour of expanded perlite particle reinforced polyphenylene sulphide. Proceedings of the Institution of Mechanical Engineers, Part L: Journal of Materials: Design and Applications. 2021;235(10):2356-67.
40. Ai MX, Cao LQ, Zhao XL, Xiang ZY, Guo XY. Preparation and characterization of polyurethane rigid foam/expanded perlite thermal insulation composites. Advanced Materials Research. 2010;96:141-4.
41. Li T-T, Chuang Y-C, Huang C-H, Lou C-W, Lin J-H. Applying vermiculite and perlite fillers to sound-absorbing/thermal-insulating resilient PU foam composites. Fibers and Polymers. 2015;16:691-8.
42. Członka S, Kairytė A, Miedzińska K, Strąkowska A. Polyurethane composites reinforced with walnut shell filler treated with perlite, montmorillonite and halloysite. International Journal of Molecular Sciences. 2021;22(14):7304.
43. Karaipekli A, Biçer A, Sarı A, Tyagi VV. Thermal characteristics of expanded perlite/paraffin composite phase change material with enhanced thermal conductivity using carbon nanotubes. Energy conversion and management. 2017;134:373-81.
44. Karaıpeklı A, Sarı A, Kaygusuz K. Thermal characteristics of paraffin/expanded perlite composite for latent heat thermal energy storage. Energy Sources, Part A. 2009;31(10):814-23.
45. Kucharczyk W, Dusiński D, Żurowski W, Gumiński R. Effect of composition on ablative properties of epoxy composites modified with expanded perlite. Composite Structures. 2018;183:654-62.
46. Rolon B, Flores J, Gutierrez V. Design and manufacture of a fiber pyro expanded perlite/epoxy composite for thermal insulation. International Journal of Advancements in Technology. 2017;8(03).
47. Allameh-Haery H, Kisi E, Fiedler T. Novel cellular perlite–epoxy foams: Effect of density on mechanical properties. Journal of Cellular Plastics. 2017;53(4):425-42.
48. Alsaadi M, Erkliğ A. Effect of perlite particle contents on delamination toughness of S-glass fiber reinforced epoxy matrix composites. Composites Part B: Engineering. 2018;141:182-90.
49. Singh T. Tribological performance of volcanic rock (perlite)-filled phenolic-based brake friction composites. Journal of King Saud University-Engineering Sciences. 2021.
50. Doğan M, Yüksel H, Kizilduman BK. Characterization and thermal properties of chitosan/perlite nanocomposites. International Journal of Materials Research. 2021;112(5):405-14.
51. Mahkam M, Vakhshouri L. Colon-specific drug delivery behavior of pH-responsive PMAA/perlite composite. International Journal of Molecular Sciences. 2010;11(4):1546-56.
52. Edres N, Buniyat-zadeh I, Turp SM, Soylak M, Aliyeva S, Binnetova N, Guliyeva N, Mammadyarova S, Alosmanov R. Structural characterization composites based on butadiene rubber and expanded perlite. Preprints 2023, 2023101338. https://doi.org/10.20944/preprints202310.1338.v1
53. Dike AS, Yilmazer U. Improvement of organoclay dispersion into polystyrene-based nanocomposites by incorporation of SBS and maleic anhydride-grafted SBS. Journal of Thermoplastic Composite Materials. 2020;33(4):554-74.
54. Luna CB, Siqueira DD, Araújo EM, Wellen RM, Jeferson Alves de Melo T. Approaches on the acrylonitrile-butadiene-styrene functionalization through maleic anhydride and dicumyl peroxide. Journal of Vinyl and Additive Technology. 2021;27(2):308-18.
55. Tayfun Ü, Kanbur Y. Asidik ve basik pomza içeren polipropilen kompozitlerinin mekanik, fiziksel ve morfolojik özellikleri. Sakarya University Journal of Science. 2018;22(2): 333-339.
56. Feng J, Yuan Q, Sun X, Yang F, Cui K, Li W, et al. Improving the properties of ABS by blending with PP and using PP-g-PS as a compatibilizer. Polymer-Plastics Technology and Materials. 2021;60(7):798-806.
57. Goodarzi V, Jafari SH, Khonakdar HA, Seyfi J. Morphology, rheology and dynamic mechanical properties of PP/EVA/clay nanocomposites. Journal of Polymer Research. 2011;18:1829-39.
58. Yildirimkaraman O, Yildiz UH, Akar AO, Tayfun U. Evaluation of water repellency in bentonite filled polypropylene composites via physical and mechanical methods. IOP SciNotes. 2020;1(2):024804.
59. Premphet K, Horanont P. Phase structure of ternary polypropylene/elastomer/filler composites: effect of elastomer polarity. Polymer. 2000;41(26):9283-90.
60. Kanbur Y, Tayfun Ü. Polipropilen/huntit kompozitlerinin mekanik, fiziksel ve morfolojik özellikleri. Sakarya University Journal of Science. 2017; 21(5): 1045-1050.

Research Article
Hittite Journal of Science and Engineering, 2023, 10 (4) 331–337
ISSN NUMBER: 2148–4171
DOI: 10.17350/HJSE19030000323

Performance Comparison of Waste Cooking Oil on Coal Slime Flotation with Sunflower Oil and Kerosene

Dilek Senol Arslan[1] Hasan Hacifazlioglu[2]
[1]Abdullah Gul University, Nanotechnology Engineering, Kayseri, Türkiye
[2]Istanbul University-Cerrahpasa University, Mining Engineering, Istanbul, Türkiye

ABSTRACT

This study explores the potential use of waste cooking sunflower oil (WSO) as an eco-friendly collector for coal slime flotation. WSO and coal slime are both waste materials and can be hazardous to human health and the environment, if not disposed of properly. In this study, co-disposal of the two wastes was investigated; a kerosene (petroleum derived oil) and crude sunflower oil (CSO) were used for collector efficiency comparisons. This study also presents a green, low-cost and environmentally friendly alternative. Kinetic flotation tests were carried out to study the flotation selectivity, flammability and combustible recovery. Contact angle measurements were performed with 3 different oils (CSO, WSO and kerosene) by sessile drop method to determine the hydrophobicity and surface properties of coal. Fourier-transform infrared (FTIR) spectroscopy was utilized to analyze for the chemical composition of both WSO and slime coal samples .

Article History:
Received: 2023/09/13
Accepted: 2023/12/04
Online: 2023/12/31

***Correspondence to**: Dilek Senol Arslan, Abdullah Gul University, Nanotechnology Engineering, 38080, Kayseri, TÜRKİYE*
E-Mail: dilek.senol@agu.edu.tr;
Phone: +90 539 799 39 00.

This article has been checked for similarity.

Keywords:
Sunflower oil; Waste cooking oil; Kerosene; Coal slime; Flotation

INTRODUCTION

Waste cooking oil, a liquid waste from kitchens and food sectors, can be hazardous to the environment and human health [1, 2]. The challenges of the treatment of WCOs are primarily involve: the disposal-collection strategy and waste reconversion [3]. In terms of WCO reconversion, they can be employed as primary raw materials in a variety of industrial processes, for instance for the production of biofuel or bio-lubricants, animal feed, and asphalt additives. Other WCO applications are only those that are directly related to their chemical composition.

The mining and washing of coal produces coal slime as a by-product. It is a semi-solid material comprised of water and crushed coal. It is mostly composed of flotation waste from coking coal preparation plants, slurry created after hydraulic coal transportation as well as washing slurry from power plant coal washing facilities [4-6].

Kerosene is a common collector in coal flotation, although it has a high collector consumption (approximately 10 kg/t) and a high cost [7, 8]. Turkey produces 5 million tons of bituminous run of mine coal annually. About 5-7% of these coals are taken under the thickener as "coal slime" or "coal fines wastes" after being washed in dense medium plants. After being dewatered using filter presses, these coals are either disposed of in waste pools or used as fuel for thermal power plants. Concentration of these coal slimes with very fine size (d50 ~ 35 μm) by flotation method is a very costly process. Because it contains high amounts of clay minerals and these clays adsorb large amounts of collectors. Prices per liter of petroleum product in Turkey are higher than in other countries of the world many times over. Therefore, to optimize the coal flotation process in Turkey, an economic collector must be found. In the present case, Turkey does not have any flotation plant for the recovery of coal slime. The biggest reason for this is the collector cost. Kerosene is a petroleum product collector, which is particularly preferred in coal flotation due to its high yield and selectivity. As petroleum products are non-renewable and have extremely flammable properties, there is a need for new research on alternative collectors. In this context, the use of vegetable oils as an alternative collector to petroleum products for coal flotation has been reported by researchers [9-19]. Vegetable oils (VOs) have low concentrations of nitrogen, sulfur,

Cite as:
Senol-Arslan D, Hacifazlioglu H. Performance Comparison of Waste Cooking Oil on Coal Slime Flotation with Sunflower Oil and Kerosene. Hittite Journal of Science and Engineering 2023;10(4):331-337. doi:10.17350/hjse19030000323

and heavy metals, it is also a non-polluting raw material that is renewable and readily available. VOs are being actively researched for alternative applications, such as biodiesel production and utilization as raw materials in the chemical and industrial sectors. These oils contain long-chain fatty acids that possess dual functions as frothers and collectors, thanks to their ester groups that contribute to their frothing abilities [10, 20, 21].Thus, it was assumed that WSO would improve coal particle flotation recovery [9, 12, 22]. Moreover, crude soybean and olive oils, each vegetable oils, were mentioned withinside the literature as collectors for fine coal recovery. For example, Colza oil turned into used as a collector to get high-calorific and low-ash coal. Additionally, Polanga and Mahua oils were utilized as collectors to increase the floatability of high ash Indian non-coking coal [23]. Numerous researchers have indicated the potential use of vegetable oils or waste cooking oils (WSO s) as collectors in coal flotation and agloflotation processes [11, 21]. The use of WSO s as a collector can be cause to as the two main problems that can occur in flotation plants. The first of these is the clogging of the liquid carrier pipes and sluices with oil. This problem can be solved by using various surfactants. The other problem is the oily wastewater that will come out after the process. There are many methods that can be applied to remove oils from oily waste water. For example, gravimetric separators remove free oil from wastewater [24, 25]. According to the US Department of Agriculture (USDA) data for the years of 2021-2022 world vegetable oil production is 214.8 million tones. This oil is used for cooking more than half of it, and on average ~ 100 million tons of WSO is produced every year [26, 27]. In this study, WSO was used as a collector in the coal flotation and the results were compared with the kerosene and sunflower oil as a collector.

MATERIAL AND METHODS

Materials

The coal slime utilized in the flotation studies was sourced from the thickener underflow stream of a coal washing plant in Turkey, where Zonguldak bituminous coal was processed (Fig. 1).

Figure 1. Image of coal slimes and clean coal production from the slime pool by flotation.

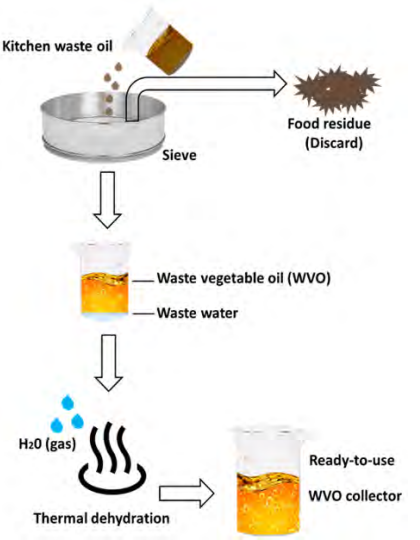

Figure 2. Flowsheet of collector prepared from kitchen waste oil.

The plant operates with a capacity of 150 t/h. Coal with a size of -100 + 1 mm is washed by a heavy-medium cyclone with three products; raw coal with a size of -1 mm is deslimed by a hydrocyclone (Ø400 mm) and the coarser fraction is routed through coal spirals. The hydrocyclone overflow material (coal slime) is sent to a thickener (Ø12 m) and then pumped into the coal sludge pool.

WSO was obtained from the kitchen waste cooking oil. The waste oil was collected in a 500 ml beaker with mixture of oil, waste water and food residue. Due to waste oil contains food residue, firstly the raw materials were sieved for the removal of solid waste and then WSO collector was prepared via filtration and heating processes. For contact angle measurements, we obtained the coal sample as a lump size from the entrance of a washery plant located in Zonguldak, Turkey.

Characterization of Coal Fine Wastes

Proximate analysis was performed to determine the characteristics of the waste coal sample. Proximate analysis was performed on a dry basis and the ash content was 33.75% the total sulfur content was 0.68%. The calculated volatile matter and fixed carbon contents are 29.10% and 37.45%, respectively. According to these results, it can be said that coal has high ash content and low sulfur content. It is in the category of medium volatile coal in terms of volatile matter content.

As a result of the size analysis of the waste coal sample with the Mastersizer 3000 laser diffraction particle size analyzer, the average particle size (d50) of the material was found to be 45 micrometers, and the d80 size was 190 micrometers.

Table 1. Properties of the WSO.

Physical Properties	Value
Viscosity	73 mPa/s
Density	0.91 g/cm³
Oil-water interfacial tension	22.02 mN/m

Collector Types; CSO, WSO and Kerosene

CSO (2000 g/t) was obtained from Kristal company in Izmir, Turkey and used as received in the experiments. WSO (2000 g/t) was used multiple times to cook meat, vegetables, and fish. Properties of the WSO are presented in Table 1.

Kerosene (from Tupras Company in Izmir, Turkey) as a traditional collector was used to compare with the proposed collectors in coal flotation process. Eucalyptus oil is used as a frother.

METHODS

Kinetic Flotation Tests and Release Tests

Flotation tests were carried out in a Denver machine with a 1.5-liter cell capacity. The impeller speed was set to 1100 revolutions per minute. In all experiments, the solid ratio was set at 10%. The sample was mixed well with tap water in the cell for 10 minutes before each flotation test to ensure that the surface was wet. Kinetic flotation tests were performed to determine WSO, CSO and kerosene collection potential (for 30, 60, and 240 seconds of froth scrapping).

The obtained concentrates underwent filtration, followed by washing with acetone and drying in an oven. Prior to initiating the kinetic flotation tests, a "release test" procedure, developed by Dell, was employed to determine the final washability limit of the coal sample [28]. The optimal washability result was achieved by varying stirring speeds in a Denver cell and employing high reagent dosages (10 kg/t WSO , 0.4 kg/t eucalyptus oil). Fig. 3 illustrates a schematic representation of the particle-oil adsorption process during coal flotation, using kerosene, CSO, and WSO.

To assess the flotation performance, various metrics including yield, assay, efficiency index, recovery, and selectivity index were examined. In this study, the comparison of flotation performance was based on the combustible recovery-concentrated ash curve. Additionally, the effectiveness of coal flotation was evaluated using an efficiency index (EI), which was calculated using Eq. 1 [29, 30].

$$EI=CRx(\frac{At}{Ac}) \quad (1)$$

where CR: combustible recovery, Ac:concentrate ash content, and At: tailing ash content [31].

Contact Angle Measurements

Contact angle is a common technique for determining a material's wettability. As mentioned earlier, wettability is determined by measuring the contact angle formed between the solid and the liquid surface when they come into contact [32].

The contact angle of kerosene, CSO and WSO was measured using the Sessile Drop method on a flat coal surface with an Attention theta contact angle goniometer (Fig. 4).

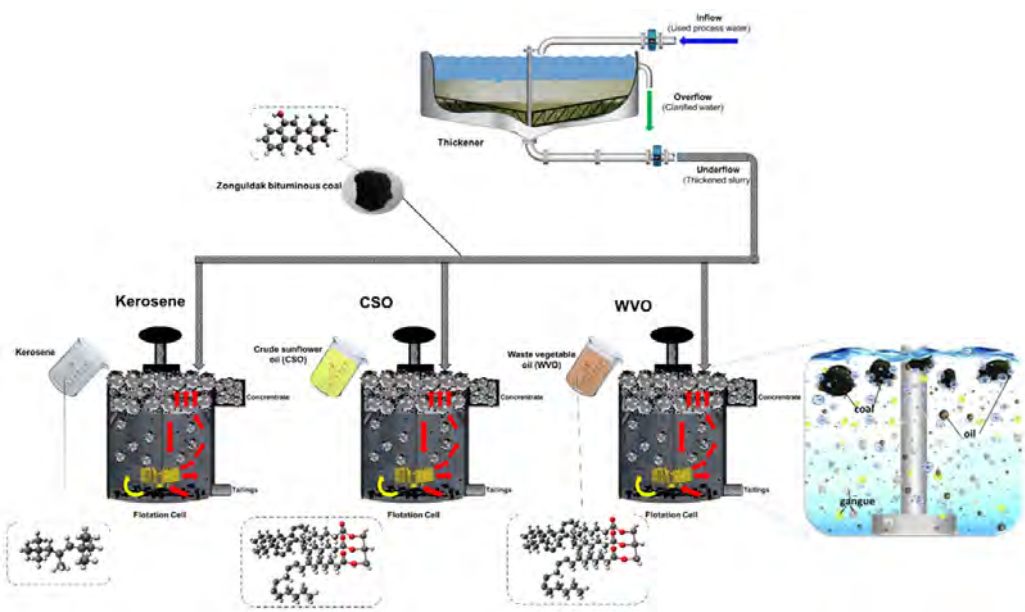

Figure 3. Schematic illustration of coal flotation with Kerosene, CSO and WSO.

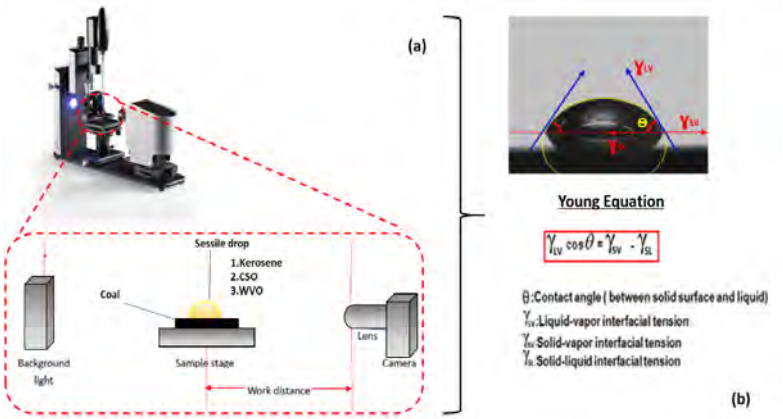

Figure 4. (a) The illustration of the contact angle goniometer (b) schematic representation of wetting statics in Young's equation for solid-liquid-vapor system.

Contact angle measurements were taken after a 15-20 second interval once the water drop size had increased. This approach was utilized to determine the contact angle values. All measurements were conducted at a temperature range of approximately 20-22°C.

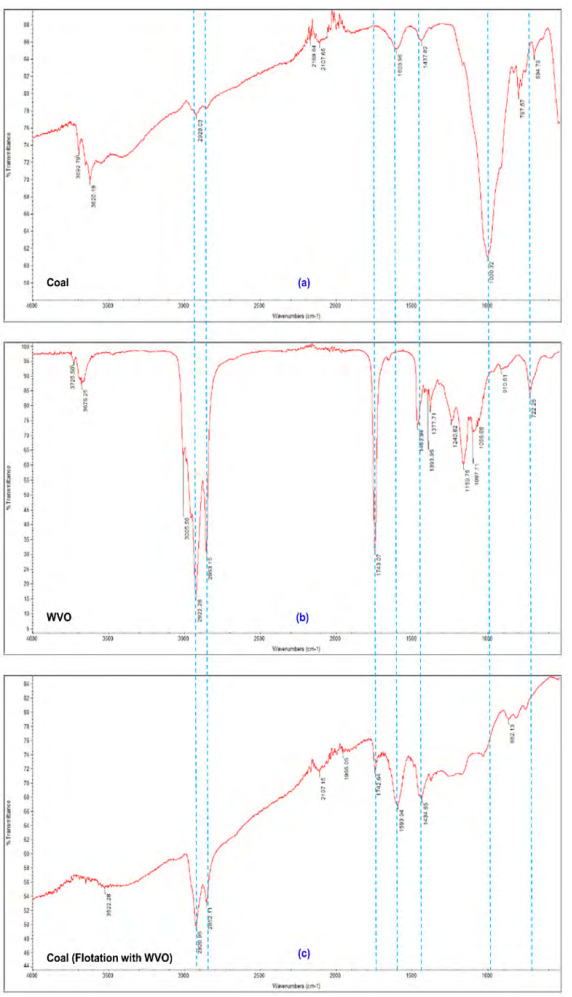

Figure 5. FT-IR spectrums of samples: a) coal, b) WSO, and c) coal floated with WSO.

The contact angle represents the angle created by a liquid droplet on a solid surface, as determined by the Young equation [33]. In Fig. 4 (b), the contact angle of an oil droplet on coal is depicted, influenced by three interfacial tensions: liquid-vapor, solid-vapor, and solid-liquid. This relationship is described by Young's equation, as shown in Eq. 2.

$$\gamma_{LV}\cos\theta = \gamma_{SV} - \gamma_{SL} \quad (2)$$

where θ is the contact angle, γ_{LV} :liquid-vapor, γ_{SV}:solid-vapor, and γ_{SL}: solid-liquid are the interfacial tensions.

RESULTS AND DISCUSSION

FTIR spectra can be used to evaluate the chemical characteristics of coal, WSO and coal floated with WSO samples , which were recorded with Thermo Scientific Nicolet 6700 FT-IR Spectrometer, over range of 400–4000 cm^{-1}. The FTIR spectrum of coal is presented in Fig. 5.

The band at 1437 cm^{-1} is attributed to vibration of CH_2 group and hydrophobic functional [34, 35]. The peaks at 2853 cm^{-1}, 2922 cm^{-1} are related to C-H stretching. [36]. The peak at 722 cm^{-1} may be the O-H stretching [37]. The peaks at 3522 cm^{-1} and at 1593 cm^{-1} are for OH and COOH group, respectively. The peaks around 1000 cm^{-1} may be attributable to C-O-C. According to literature [30, 35, 38, 39] the bands at 3452 cm^{-1} were assigned to OH vibrations. The peaks observed at 2920 cm^{-1} is due to the aliphatic hydrocarbon groups vibration in coal [40].

Releasing test results for WSO, CSO, and kerosene is important for assessing their suitability for different applications, ensuring compliance with standards, and ensuring optimal performance and efficiency. As seen in Fig. 6, kerosene has a higher collection capacity than WSO. In the experiments using kerosene, 8.97% ash clean coal was recovered with 64.58% combustible recovery value, while in the experiments using WSO, 9.88% ash clean coal was

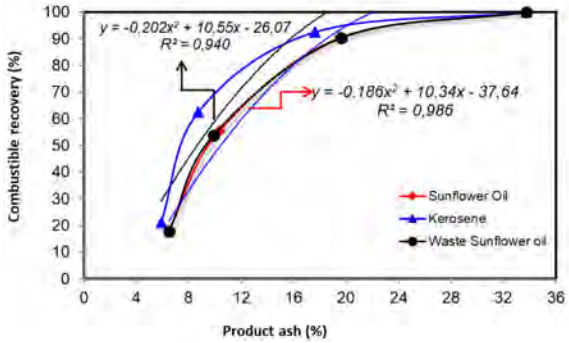

Figure 6. Release test results with WSO, CSO and kerosene.

recovered with 53.73% combustible recovery value. If clean coal product with 10% ash is desired to be sold, the kerosene collector has a combustible recovery rate of approximately 69%, while the WSO has a rate of around 54%. The lower combustible recovery of WSO has been hypothesized to be due to the hydrophilic oxygen bonds present in its structure, which limits its ability to collect. Kerosene is an effective collector due to its absence of oxygen groups and its purely hydrocarbon structure. Recent research suggests that oxygen-containing functional groups, particularly the carboxyl group, play a crucial role in enhancing coal surface wettability [41]. Zhou et al. (2015) have reported that carboxyl and hydroxyl groups are the most effective promoters of surface wettability based on XPS peak-split data. Fig. 7 illustrates the results of kinetic flotation tests conducted using CSO, WSO , and kerosene.

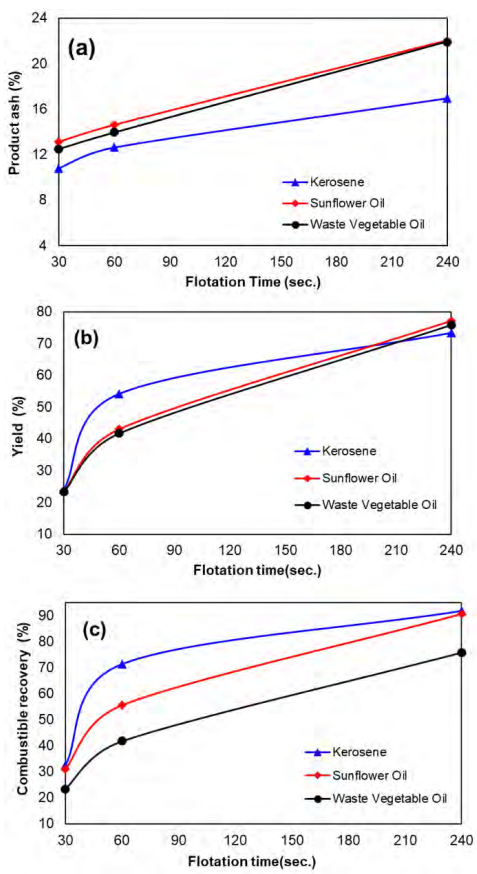

Figure 7. (a) Product ash, (b) yield and combustible recovery values obtained in kinetic tests depending on flotation time with WSO, CSO and kerosene used as collectors.

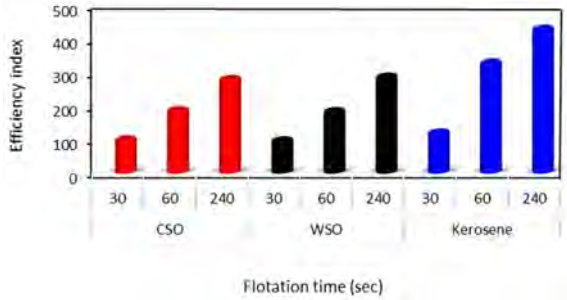

Figure 8. Flotation efficiency index (EI) at various collecting times with WSO, CSO, and kerosene.

Fig. 7 indicates that the combustible recovery of kerosene at the end of 240 seconds flotation time is 94.17%, while the combustible recovery value obtained with WSO is 88.98%. The results indicate that the kerosene collector exhibits higher selectivity compared to CSO and WSO. For instance, after 240 seconds of flotation, the product ash obtained was 17.94% with kerosene, whereas it was 21.73% with the WSO collector.

The efficiency index of CSO, WSO, and kerosene collectors increased as flotation time increased for the three types of collectors, as shown in Fig. 8. At all-time intervals, the efficiency index of kerosene was higher than that of CSO and WSO. For instance, after 240 seconds of flotation time, the efficiency index for kerosene is 471.65, whereas for WSO it is 284.80.

As depicted in Fig. 9, the contact angles measured for kerosene, WSO, and CSO oils on the coal surface were 100o, 91o, and 88o, respectively. The results from Fig. 7 show that kerosene exhibits superior collecting properties on the coal surface compared to CSO and WSO. Hence, these findings support the flotation experiments.

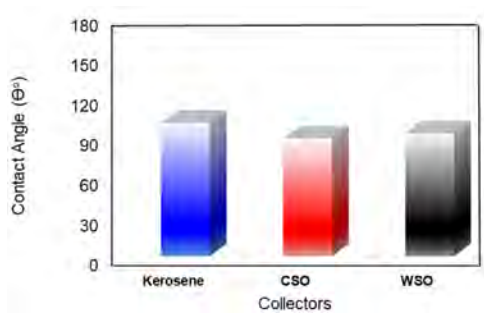

Figure 9. A representation of the contact angles formed by sessile liquid drops (kerosene, CSO and WSO) on the smooth surface of coal.

CONCLUSION

This study shows that using WSO oil in coal slime flotation is applicable, green, efficient, low-cost, and environmentally friendly. The results were evaluated with kerosene and WSO, which have a significant difference between them. Based on the study's findings, WSO effectively lowered the ash content of fine bituminous coal from 33.75% to 6.50%. While WSO can result in clean coal with low ash content, its combustible recovery is lower than that of kerosene. It is most likely due to the WSO 's lower surface coating ability than kerosene. In the release test, WSO achieved a clean coal with 10% ash and a combustible recovery of 54%, while kerosene had a higher recovery of 69%. Kerosene also showed greater selectivity, with a product ash of 17.94% compared to 21.73% for WSO after 240 seconds of flotation. The selectivity index for kerosene was 471.65, while WSO had a lower value of 284.80. Overall, WSO 's performance was approximately 15% lower than kerosene in all aspects, and it had a 40% lower efficiency index compared to kerosene. This is an expected result, but in the near future, oil reserves will be depleted and mankind will turn to renewable resources.

CONFLICT OF INTEREST

Authors approve that to the best of their knowledge, the¬re is not any conflict of interest or common interest with an institution/organization or a person that may affect the review process of the paper.

AUTHOR CONTRIBUTION

All authors contributed to the study conception and de¬sign. Material preparation, data collection and analysis. Dilek Şenol-Arslan: Conceptualization, Methodology, Writing - original draft, Visualization. Hasan Hacıfazlıoğlu: Data curation, Investigation, Supervision, Writing - review and editing.

References

1. Singh-Ackbarali, D., et al., Potential of used frying oil in paving material: solution to environmental pollution problem. Environmental Science and Pollution Research, 2017. 24: p. 12220-12226.
2. Khodadadi, M.R., et al., Recent advances on the catalytic conversion of waste cooking oil. Molecular Catalysis, 2020. 494: p. 111128.
3. Teixeira, M.R., R. Nogueira, and L.M. Nunes, Quantitative assessment of the valorisation of used cooking oils in 23 countries. Waste Management, 2018. 78: p. 611-620.
4. Wang, H., et al., Morphological and structural evolution of bituminous coal slime particles during the process of combustion. Fuel, 2018. 218: p. 49-58.
5. 5. Tan, J., et al., Using low-rank coal slime as an eco-friendly replacement for carbon black filler in styrene butadiene rubber. Journal of Cleaner Production, 2019. 234: p. 949-960.
6. Guo, H., et al., Efficient utilization of coal slime using anaerobic fermentation technology. Bioresource Technology, 2021. 332: p. 125072.
7. Liu, D., et al., Flotation specificity of coal gasification fine slag based on release analysis. Journal of Cleaner Production, 2022. 363: p. 132426.
8. Zhang, R., et al., Recovering unburned carbon from gasification fly ash using saline water. Waste Management, 2019. 98: p. 29-36.
9. Klimpel, R., Frothers. Reagents in mineral technology, 1988.
10. Dey, S. and S. Pani, Effective processing of low-volatile medium coking coal fines of Indian origin using different process variables of flotation. International Journal of Coal Preparation and Utilization, 2012. 32(6): p. 253-264.
11. Hacifazlioglu, H. and D. Senol-Arslan, Sunflower oil as green collector in bituminous coal flotation. Energy Sources, Part A: Recovery, Utilization, and Environmental Effects, 2017. 39(15): p. 1602-1609.
12. Alonso, M., C. Castano, and A. Garcia, Performance of vegetable oils as flotation collectors for the recovery of coal from coal fines wastes. Coal Perparation, 2000. 21(4): p. 411-420.
13. Klimpel, R. and R. Hansen, Frothers: Reagents in Mineral Technology. 1987, Marcel Dekker, New York, NY.
14. Hacifazlioglu, H., Effect of temperature on coal flotation with waste vegetable oil as collector. International Journal of Coal Preparation and Utilization, 2018. 38(4): p. 163-169.
15. Arcos, F. and L. Uribe, Evaluation of the Use of Recycled Vegetable Oil as a Collector Reagent in the Flotation of Copper Sulfide Minerals Using Seawater. Recycling, 2021. 6(1): p. 5.
16. de Oliveira, P., et al., Apatite flotation using pataua palm tree oil as collector. Journal of Materials Research and Technology, 2019. 8(5): p. 4612-4619.
17. Zhu, X.-n., et al., Cleaner approach to fine coal flotation by renewable collectors prepared by waste oil transesterification. Journal of Cleaner Production, 2020. 252: p. 119822.
18. Zhu, X.-n., et al., Clean utilization of waste oil: Soap collectors prepared by alkaline hydrolysis for fluorite flotation. Journal of Cleaner Production, 2019. 240: p. 118179.
19. Fan, G., et al., Clean products from coal gasification waste by flotation using waste engine oil as collector: Synergetic cleaner disposal of wastes. Journal of Cleaner Production, 2021. 286: p. 124943.
20. Valdés, A.F. and A.B. Garcia, On the utilization of waste vegetable oils (WSO) as agglomerants to recover coal from coal fines cleaning wastes (CFCW). Fuel, 2006. 85(5-6): p. 607-614.
21. Vasumathi, N., et al., Eco friendly and cost-effective reagent for coal flotation. International Journal of Engineering Research, 2013. 2(7): p. 418-423.
22. Moudgil, B.M. and P. Somasundaran, Reagents in mineral Technology. 1988: M. Dekker.
23. Das, B. and P. Reddy, The utilization of non-coking coal by flotation using non-conventional reagents. Energy Sources, Part A: Recovery, Utilization, and Environmental Effects, 2010. 32(19): p. 1784-1793.
24. Yu, L., M. Han, and F. He, A review of treating oily wastewater. Arabian journal of chemistry, 2017. 10: p. S1913-S1922.
25. Hanafy, M. and H. Nabih, Treatment of oily wastewater using dissolved air flotation technique. Energy Sources, Part A, 2007. 29(2): p. 143-159.
26. Anastas, P.T. and J.C. Warner, Principles of green chemistry. Green chemistry: Theory and practice, 1998: p. 29-56.
27. Williams, C., Y. Peng, and R. Dunne, Eucalyptus oils as green collectors in gold flotation. Minerals Engineering, 2013. 42: p. 62-67.

28. Dell, C., et al., Release analysis: a comparison of techniques. Trans. Inst. Min. Metal., Sec., C, Mineral Process Extr. Metal, 1972. 81: p. C89.
29. Firth, B.A., A.R. Swanson, and S.K. Nicol, Flotation circuits for poorly floating coals. International Journal of Mineral Processing, 1979. 5(4): p. 321-334.
30. Gui, X., et al., Intensification mechanism of oxidized coal flotation by using oxygen-containing collector α-furanacrylic acid. Powder Technology, 2017. 305: p. 109-116.
31. Vanangamudi, M., K. Pillai, and T. Rao, Effect of some operating variables on the efficiency index of a coal flotation operation. International Journal of Mineral Processing, 1981. 8(1): p. 1-7.
32. Zhou, G., et al., Effects of oxygen element and oxygen-containing functional groups on surface wettability of coal dust with various metamorphic degrees based on XPS experiment. Journal of analytical methods in chemistry, 2015. 2015.
33. Young, T., An essay on the cohesion of fluids. Philosophical Transactions of the Royal Society of London, 1805. 95: p. 65-87.
34. Zzeyani, S., et al., Assessment of the waste lubricating oils management with antioxidants vegetables extracts based resources using EPR and FTIR spectroscopy techniques. Energy, 2019. 180: p. 206-215.
35. Xia, W., J. Yang, and C. Liang, Improving oxidized coal flotation using biodiesel as a collector. International Journal of Coal Preparation and Utilization, 2013. 33(4): p. 181-187.
36. Jiao, A., S. Tian, and H. Lin, Analysis of Outburst Coal Structure Characteristics in Sanjia Coal Mine Based on FTIR and XRD. Energies, 2022. 15(6): p. 1956.
37. Sun, W., et al., Preparation of hydrolyzate of hogwash oil (HHO) and its application in separating diaspore from kaolinite. Minerals Engineering, 2010. 23(9): p. 670-675.
38. Xia, Y., Y. Xing, and X. Gui, Oily collector pre-dispersion for enhanced surface adsorption during fine low-rank coal flotation. Journal of Industrial and Engineering Chemistry, 2020. 82: p. 303-308.
39. Yao, S., et al., Evolution of coal structures: FTIR analyses of experimental simulations and naturally matured coals in the Ordos Basin, China. Energy Exploration & Exploitation, 2011. 29(1): p. 1-19.
40. Li, W., et al., Hydrocarbon Generation and Chemical Structure Evolution from Confined Pyrolysis of Bituminous Coal. Acs Omega, 2020. 5(31): p. 19682-19694.
41. Wan, H., et al., Effect of the oxygen-containing functional group on the adsorption of hydrocarbon oily collectors on coal surfaces. Physicochemical Problems of Mineral Processing, 2022. 58.

Research Article
Hittite Journal of Science and Engineering, 2023, 10 (4) 339–348
ISSN NUMBER: 2148–4171
DOI: 10.17350/HJSE19030000324

Thermodynamic Analysis of the Integrated System that Produces Energy by Gradual Expansion from the Waste Heat of the Solid Waste Facility

Ahmet Elbir
Suleyman Demirel University, YEKARUM, Isparta, Türkiye

ABSTRACT

The rapid increase in consumer societies leads to a rise in waste facilities. Especially when considering the amount of power used in waste plants and the corresponding waste heat generated, an approach to recover waste heat from these facilities has been proposed. Initially, the waste heat from the solid waste facility was assessed using the Rankine cycle. Subsequently, an Organic Rankine Cycle (ORC) system was integrated into the lower cycle of the steam Rankine cycle. The integrated system was completed by harnessing waste heat from the Rankine steam cycle in the carbon dioxide cycle. These power generation systems are designed with two turbines, each with gradual expansion. Using sub-cycles, 1 kg/s of air at 873.2 K was obtained by evaluating the waste heat. In terms of energy efficiency, it can be observed that the R744 gradual expansion cycle exhibits the highest energy and exergy efficiency. Cooling with water in heat exchangers reduces exhaust efficiency. The highest mass flow requirement is found in the ORC system when the R123 fluid is used. The energy efficiency for the entire system was calculated as 22,4%, and the exergy efficiency for the entire system was calculated as 60.7%. When Exergo Environment Analysis was made, exergy stability factor was found to be %60.7, exergetic sustainability index was found to be 2.66. There is also 370K waste heat available, which is recommended for use in drying units. These calculations were performed using the Engineering Equation Solver (EES) program.

Keywords:
Energy; Exergy; Gradual expansion; Waste heat; Exergo environment analysis

Article History:
Received: 2023/09/27
Accepted: 2023/11/17
Online: 2023/12/31

***Correspondence to**: Ahmet Elbir,*
Suleyman Demirel University, YEKARUM,
Isparta, TÜRKİYE
E-Mail: ahmetelbir@sdu.edu.tr;
Phone: +90 506 711 88 59.

This article has been checked for similarity.

INTRODUCTION

Gas turbines are thermal machines commonly used in applications such as power generation or aircraft propulsion. The principle of gradual expansion (stepwise expansion) is a design feature employed to increase efficiency and optimize the performance of gas turbines. In this context, waste gases at high temperatures and pressures, resulting from the operational principles of gas turbines in industrial processes, energy production facilities, and other similar applications, can be repurposed and converted into energy without harming the environment. Thermal energy obtained by recycling waste heat can be used in various ways, such as hot water production, steam generation, or electricity production, thereby enhancing energy efficiency and striving for more effective resource utilization. This article will explore methods for utilizing waste heat from gas turbines, discussing the advantages, challenges, and application areas of these methods. Thus, the significance of this innovative approach, which contributes to sustainable energy production, will be emphasized. Published studies in the literature, They realized an integrated Organic Rankine Cycle (ORC) to recover the waste heat of exhaust gases in the Afyon Biogas Power Plant, which produces biogas from chicken manure. They stated that waste heat recovery to the power plant greatly increases the performance parameters and economic cost savings values of the system. They calculated the maximum power capacity of the facility supported by the Organic Rankine Cycle as 4828.8 kW. They calculated the energy and exergy efficiencies as 37.4% and 32.1%, respectively, when the power plant operates under optimum operating conditions [1]. In this article, thermodynamic and thermoeconomic analyzes as well as optimization of the organic Rankine cycle (ORC) were carried

Cite as:
*Elbir A. Thermodynamic Analysis of the Integrated System that Produces Energy by Gradual Expansion from the Waste Heat of the Solid Waste Facility. Hittite Journal of Science and Engineering 2023;10(4):**339-348**. doi:10.17350/hjse19030000**324***

out. The system was applied to an existing solid waste power plant with an installed power of 5.66 MW in order to generate additional power from exhaust gas. The originality of this article is that they made calculations based on the analysis of the possibility of converting the exhaust gas at 566 °C into electricity using the ORC system in the waste-to-energy concept [2]. They calculated the energetic and exergetic analysis of a multiple generation system consisting of a micro gas turbine, an organic Rankine cycle (ORC), an absorption cooler and a water heater [3]. He aimed to increase the efficiency of systems by using thermodynamic cycles from waste heat sources. The thermodynamic results of increasing the efficiency of the system by adding subcycles of the waste heat of a gas turbine to the designed system were examined [4]. Provides the design, analysis and optimization of a new municipal solid waste fueled combined cycle power plant to meet the grid electricity needs of an urban municipality [5]. They implemented a gas turbine cycle model adopting the organic Rankine cycle (ORC) in which supercritical CO_2 (S-CO_2) was used as the working fluid. Thermodynamic analysis of the system used Aspen Plus and EES programs. As a result of thermodynamic analyses, the electricity production capacity, energy and exergy efficiencies of the proposed system were found to be 1530.88 kW, 23.30% and 59.60%, respectively [6]. Thermodynamic and thermoeconomic analyzes as well as optimization of the organic Rankine cycle (ORC) were carried out. The system was adapted to an existing solid waste power plant with an installed power of 5.66 MW in order to generate additional power from exhaust gas [7]. They integrated the organic Rankine cycle (ORC) into a 2 MW natural gas engine to generate electricity by recovering the engine's exhaust heat [8]. In their study, they proposed a thermoeconomic optimization study of a vehicle-mounted ORC unit to recover waste heat from various exhaust gas conditions of a vehicle [9]. They have made a detailed comparison of the potential of ORC and S-CO_2 as bottoms of industrial gas turbines in Combined Heat and Power (CHP) system. They stated that the S- CO_2 dip cycle gives better results than ORC in both electrical and thermal efficiency, since the cycle pressure ratio is not affected by the thermal user temperature in the s-CO_2 solution examined [10]. Thermodynamic analysis of the single-stage, single-expansion S-CO_2/ORC system, which operates at the same lower and upper temperatures as the single-stage, double-expansion S-CO_2/ORC system, was examined [11]. They designed an organic Rankine cycle (ORC) waste heat recovery system with an internal heat exchanger (IHE) to recover waste heat from

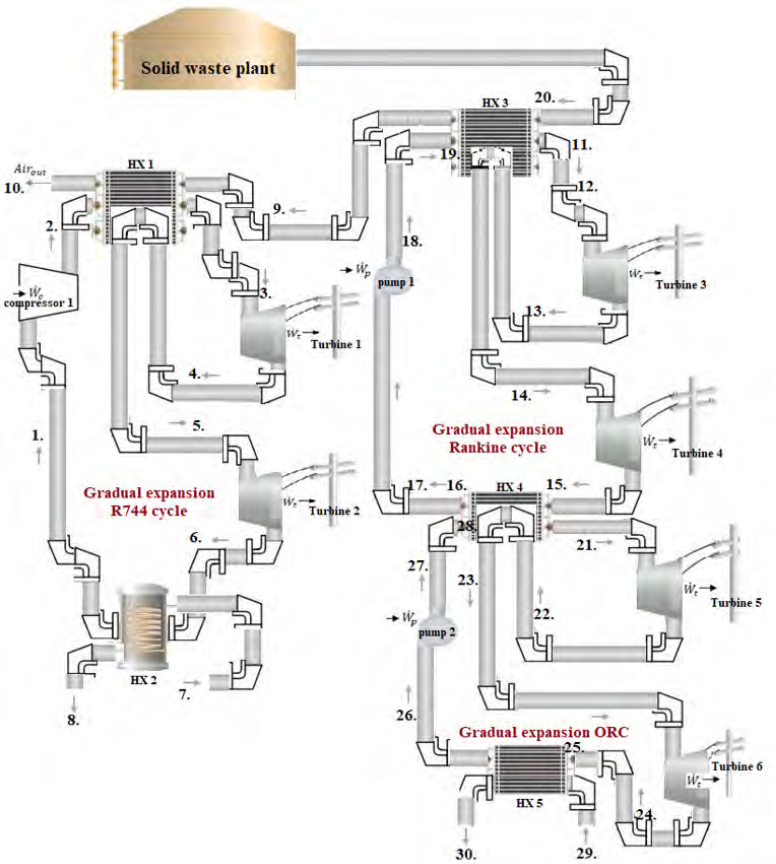

Figure 1. Integrated power generation plant with thermodynamic analysis.

diesel engine exhaust [12]. The main difference between stepwise expansion with reheat (Regenerative Rankine Cycle) and Non-Regenerative Rankine cycle energy cycles is energy recovery. Gradual expansion with reheat improves efficiency by recovering the energy of the steam after expansion and contributes to more electricity production. Stepless expansion, on the other hand, expands without this recovery process and is therefore less energy efficient. Which cycle is preferred depends on the specific requirements and cost factors of the application.

In the design of gradual expansion, the strategy of reheating and raising the fluid's temperature during pressure drops between the blades in gas turbines is employed to enhance thermal efficiency and performance. This process is often referred to as reheat or interstage heating. Consequently, reheating and increasing the fluid's temperature through reheat or intermediate stage heating in gas turbines offer several benefits, including improved thermal efficiency, enhanced performance, a broad operating range, and optimized control. This strategy represents a crucial design method used by engineers to ensure that gas turbines operate with greater effectiveness and efficiency.

MATERIAL AND METHODS

System Description

Fig. 1 shows the schematic view of the integrated power generation facility for which thermodynamic analysis was performed.

In Fig. 1, the waste heat from the solid waste facility was first evaluated in the Rankine cycle. An ORC system has been added to the lower cycle of the steam Rankine cycle. The integrated system was completed by adding the waste heat from the Rankin steam cycle to the carbon dioxide cycle. These power generating systems are designed with two turbines each with gradual expansion.

1. 2→3: Heat transfer from adiabatic and counterflow Heat Exchanger, waste heat transfer to carbon dioxide cycle 9→10 HX-1

2. 3→4: Expanding the adiabatic Turbine-1 to generate work

3. 4→5: Heat transfer from adiabatic and counterflow Heat Exchanger, waste heat to carbon dioxide cycle HX-1

4. 5→6: Reheating the working fluid to Turbine-2 inlet temperature,

5. 6→1: Heat removal by Heat Exchanger as isobar. HX-2

6. 1→2: Increasing the pressure of the with the adiabatic compressor.

7. 18→12: Heat transfer from adiabatic and counterflow Heat Exchanger, waste heat transfer to Rankine cycle 20→9 HX-3

8. 12→13: Expanding the adiabatic Turbine-3 to generate work

9. 13→14: Heat transfer from adiabatic and counterflow Heat Exchanger, waste heat to Rankine cycle HX-4

10. 14→15: Reheating the working fluid to Turbine-4 inlet temperature,

11. 15→17: Heat removal by Heat Exchanger as isobar. HX-4

12. 17→18: Increasing the pressure of the saturated liquid with the adiabatic pump.

13. 27→21: Heat transfer from adiabatic and counterflow Heat Exchanger, waste heat transfer to ORC 24→20 HX-4

14. 12→13: Expanding the adiabatic Turbine-5 to generate work

15. 13→14: Heat transfer from adiabatic and counterflow Heat Exchanger, waste heat to ORC HX-4

16. 14→15: Reheating the working fluid to Turbine-6 inlet temperature,

17. 15→17: Heat removal by Heat Exchanger as isobar. HX-5

18. 17→18: Increasing the pressure of the saturated liquid with the adiabatic pump.

Assumptions for thermodynamic analysis:

Pure substance is used in the system.

All compression processes in the system are adiabatic.

Pressure drops in system components and pipeline as well as heat transfer over the pipeline were also neglected.

All heat exchangers are counter flow. Heat exchanges are identical.

System operates in steady state.

Gravitational potential energy and kinetic energy are not taken into account.

The isentropic efficiency of compressors, pumps and turbines is 90%

The ambient temperature was taken as 293.2 K.

The exhaust exit temperature of the furnace or heating system used in the solid waste facility was taken as 873.2 K [13].

Energy and exergy analyzes

For steady state in thermodynamic analysis, the basic mass balance equation can be given as follows [14-15,16];

$$\sum \dot{m}_{in} = \sum \dot{m}_{ex} \tag{1}$$

where $\dot{m}$ is the mass flow rate, the in and ex indices represent the inlet and outlet states, respectively. The energy balance is given as:

$$\begin{aligned} &\dot{Q}_{in} + \dot{W}_{in} + \sum_{in} \dot{m}(\mathrm{h} + \frac{v^2}{2} + \mathrm{gz}) \\ &= \dot{Q}_{ex} + \dot{W}_{ex} + \sum_{ex} \dot{m}(\mathrm{h} + \frac{v^2}{2} + \mathrm{gz}) \end{aligned} \tag{2}$$

Here, $\dot{Q}$ is the heat transfer rate, $\dot{W}$ is the power, h is the specific enthalpy, v is the velocity, z is the height, and g is the gravitational acceleration. The entropy balance equation for steady-state conditions is written as:

$$\sum_{in} m_{in} s_{in} + \sum_{k} \frac{\dot{Q}}{T_k} + \dot{S}_{gen} = \sum_{ex} m_{ex} s_{ex} \tag{3}$$

where s is the specific entropy and $\dot{S}_{gen}$ is the entropy generation rate. The exergy balance equation can be written as:

$$\begin{aligned} &\sum \dot{\mathrm{m}}_{\mathrm{in}}\, ex_{in} + \sum \dot{E}x_{Q,in} + \sum \dot{E}x_{W,in} \\ &= \sum \dot{\mathrm{m}}_{ex}\, ex_{ex} + \sum \dot{E}x_{Q,\mathrm{ex}} + \sum \dot{E}x_{W,\mathrm{ex}} + \dot{E}x_D \end{aligned} \tag{4}$$

The specific flow exergy can be written as:

$$ex = x_{ph} + ex_{ch} + \mathrm{ex}_{\mathrm{p}t} + ex_{kn} \tag{5}$$

The kinetic and potential parts of the exergy are assumed to be negligible. Also, the chemical exergy is assumed to be negligible. The physical or flow exergy (ex_{ph}) is defined as:

$$ex_{ph} = (h - h_o) - T_o(s - s_o) \tag{6}$$

where h and s represent specific enthalpy and entropy, respectively, in the real case. h_o and s_o are enthalpy and entropy at reference medium states, respectively.

Exergy destruction is equal to specific exergy times mass;

$$E_{xd} = ex * m \tag{8}$$

$\dot{E}x_D$, are work-related exergy ratios and are given as:

$$Ex_D = T_0 \dot{S}_{gen} \tag{9}$$

$\dot{E}x_W$, are work-related exergy ratios and are given as:

$$Ex_W = \dot{W} \tag{10}$$

$\dot{E}x_Q$, are the exergy rates related to heat transfer and are given as below.

$$\dot{E}x_Q = (1 - \tfrac{T_o}{T})\dot{\mathrm{Q}} \tag{11}$$

$\dot{E}x_{D,syst.}$ Exergy destruction in the system;

$$\dot{E}x_{D,syst.} = \dot{E}x_{in} + \dot{E}x_{out} \tag{12}$$

What work comes out of the system;

$$\dot{W}net_{out} = \dot{Q}_{in} - \dot{Q}_{out} \tag{13}$$

system thermal efficiency (η);

$$\eta = \frac{energy\ in\ exit\ outputs}{total\ energy\ inlets} \tag{14}$$

The exergy efficiency (ψ) can be defined as follows;

$$\psi = \frac{exergy\ in\ exit\ outputs}{total\ exergy\ inlets} \tag{15}$$

Exergoenvironmental Analysis

fei shows exergoenvironmental impact factor, $\dot{E}x_{D,tot.}$ is total exergy destruction rate, $\dot{E}x_{D,in.}$ is input exergy rate [17],

$$fei = \frac{\dot{E}x_{Dtot.}}{\dot{E}x_{\mathrm{in.}}} \tag{16}$$

Cei is exergoenvironmental impact coefficient, ψ_{ex} represents exergy efficiency of the system,

$$Cei = \frac{1}{\psi_{ex}/100} \tag{17}$$

Φei is exergoenvironmental impact index,

$$\Phi\mathrm{ei} = \mathrm{fei} \times \mathrm{Cei} \tag{18}$$

Φeii represents exergoenvironmental impact improvement,

$$\Phi\mathrm{eii} = \frac{1}{\Phi\mathrm{ei}} \tag{19}$$

fes is the exergy stability factor,

$$\mathrm{fes} = \frac{\dot{E}x_{D,out.}}{\dot{E}x_{D,out.} + \dot{E}x_{D,tot.}} \tag{20}$$

Φest represents exergetic sustainability index.

$$\Phi\mathrm{est} = \mathrm{fes} \times \Phi\mathrm{eii} \tag{21}$$

Table 1. Thermodynamic properties of the positions of the carbon dioxide cycle.

Location	T [K]	s [kJ/kg.K]	P [bar]	h [kJ/kg]	ex[kj/kg]
1.R744	313.2	-1.08	80	-103.6	214.1
2.R744	374.9	-1.072	190	-70.52	244.7
3.R744	460	-0.7164	190	75.99	287
4.R744	428.2	-0.7108	135	54.51	263.9
5. R744	460	-0.6163	135	96.41	278.8
6.R744	412.7	-0.6072	80	62.73	241.8
7. Water inlet	293.2	0.2965	1	84.01	0
8.Water outlet	303.2	0.4374	1	126	0.7042
9.Air inlet	492.2	7.371	1	495.3	47.97
10.Air outlet	370	7.08	1	370.8	8.675
To. R744	293.2	-0.01403	1	-5.168	0

RESULTS AND DISCUSSION

In one study, modeling ORC as a second stage waste heat recovery system after the primary steam cycle, the system efficiency of the steam cycle was found to be 7.63%. With the addition of ORC, this efficiency increased to 7.81% [18]. R123 has a low boiling point temperature (27.82 °C), making it a preferable fluid for aluminum cycles. They calculated the efficiency of the Basic ORC system as 6.15% and the Regenerative ORC system as 7.98% [19]. In a study optimized for reheated S-CO_2 Brayton cycle, thermal efficiency was found to be 15.2–36.3% and 14.8–35.6% [20]. In examining the Exergo Environmental Analysis, they found the exergy stability factor to be 60% and the exergetic sustainability index to be 2.62.

Thermodynamic properties of the positions of the carbon dioxide cycle are presented in Table 1.

Comparison between regenerative reheat cycle and non-regenerative non-reheat cycle is provided in Fig. 3.

Table 2 compares the thermodynamic results of the system operating with reheating and gradual expansion in the case of stepless and non-reheating operation.

Considering the carbon dioxide cycle, in case of switching from the reheated gradual expansion cycle to the conventional cycle, there will be a 71.4% decrease in exergy efficiency and a 32.5% decrease in energy efficiency. Additionally, the mass flow rate of carbon dioxide will increase by 3.7%, while the mass flow rate of water required for cooling will also increase by 4.3%.

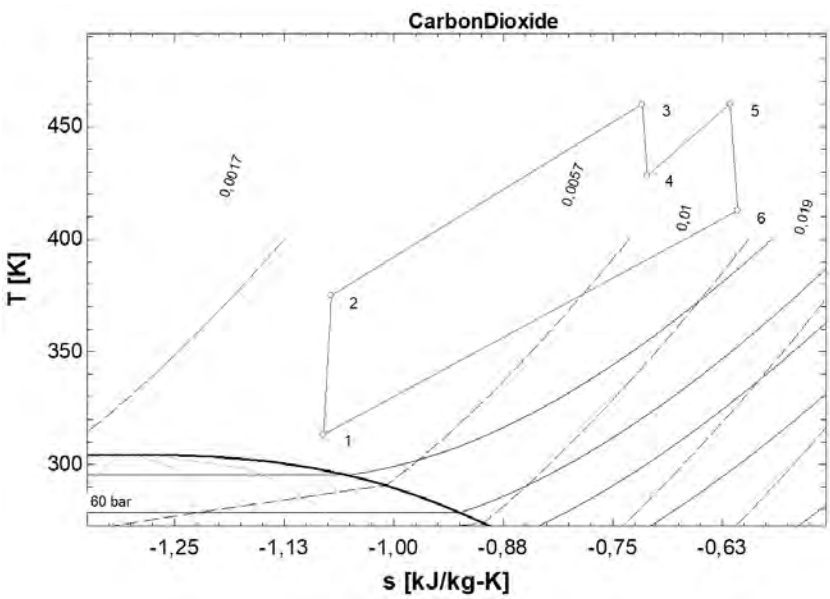

Figure 2. The temperature entropy diagram for the R744 gradual expansion.

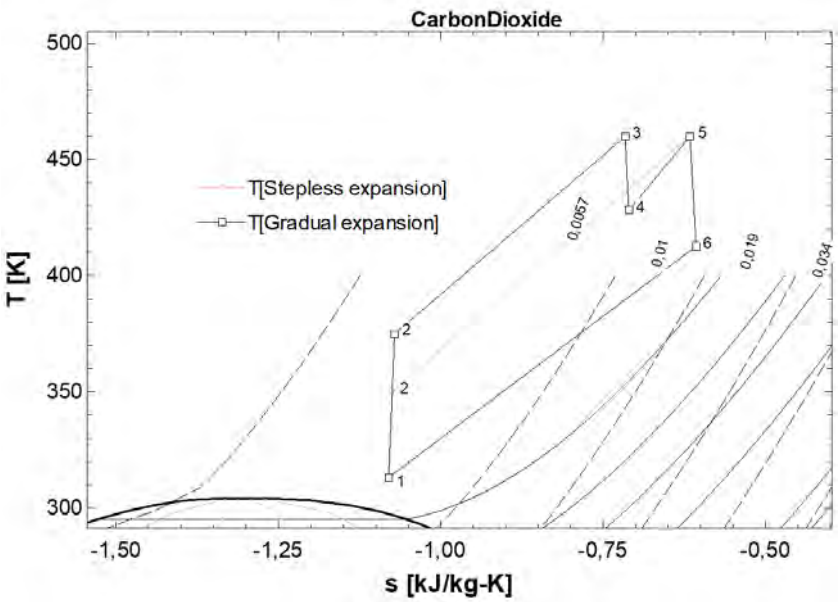

Figure 3. Comparison of regenerative and non-regenerative cycles for carbon dioxide as the working fluid.

Table 2. Thermodynamic consequences of gradual and stepless expansion.

location	R744 Cycle gradual expansion	location	R744 Cycle stepless expansion
Q in [9-10]	124,5 kW	Q in [9-10]	124.5 kW
R744exergy	78.96 %	R744exergy	22.6 %
R744energy	24.9 %	R744energy	16,8 %
Ex comp1	1.71 kW	Ex comp1	1.062 kW
Ex Turb.1	1.08 kW	Ex Turb.1	1.83 kW
Ex Turb.2	1.76 kW	Ex Turb.2	-----
Ex HX1	1.889 kW	Ex HX1	7.036 kW
Ex HX2	20.12 kW	Ex HX2	20.86 kW
HX1	95.19 %	HX1	82.1 %
HX2	10.08 %	HX2	10.03 %
comp1 [1-2]	92.17 %	comp1 [1-2]	91.62 %
Turb.1 [3-4]	92.92 %	Turb.1 [3-4]	92.6 %
Turb.2 [5-6]	92.66 %	Turb.2 [5-6]	-----
m R744	0.6608 kg/s	m R744	0.6857 kg/s
Wcomp.1 [1-2]	21.88 kW	Wcomp.1 [1-2]	1.68 kW
WTurb.1 [3-4]	14.19 kW	WTurb.1 [3-4]	23.09 kW
WTurb.2 [5-6]	22.25 kW	WTurb.2 [5-6]	-----
Q out [1-6]	109.9 kW	Q out [1-4]	114.1 kW
m su	2.616 kg/s	m su [	2.728 kg/s

Table 3. Thermodynamic properties of the positions of the Rankine cycle.

Location	T [K]	s [kJ/kg.K]	P [bar]	h [kJ/kg]	ex[kj/kg]
11. water	443.5	6.662	7.989	2768	817.8
12. water	505.5	6.966	7.989	2912	872.6
13. water	452.3	6.991	4.738	2812	765.4
14. water	505.5	7.227	4.738	2925	809.1
15. water	395.5	7.287	1.487	2716	582.9
16. water	384.2	7.226	1.487	2693	577
17. water	384.2	1.431	1.487	466	49.42
18. water	384.3	1.431	7.989	466.8	50.13
19. water	443.5	2.045	7.989	720.6	123.9
To.water	293.2	6.846	1	293.4	0
20. Air inlet	873.2	7.982	1	903.4	276.7
9.Air outlet	492.2	7.371	1	495.3	47.94

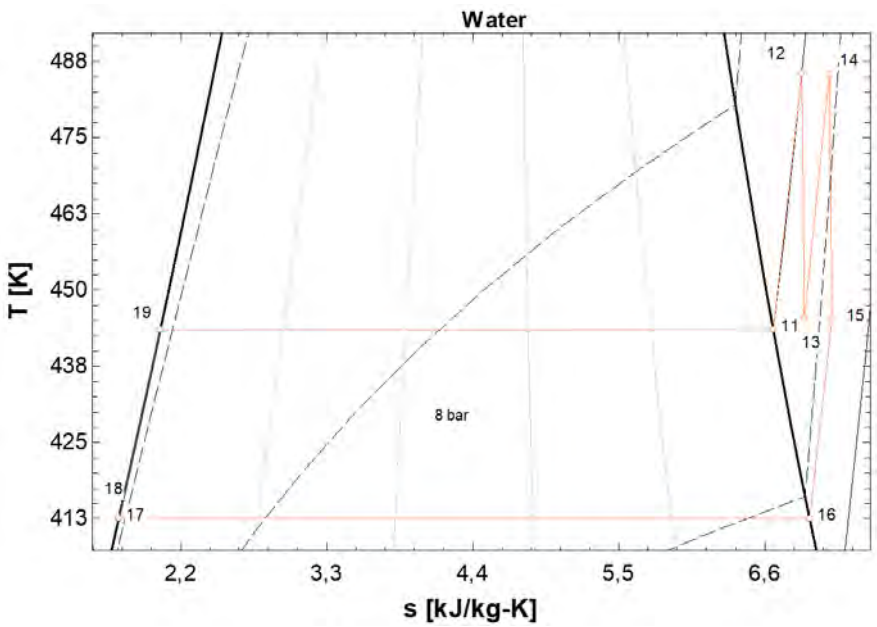

Figure 4. The temperature entropy diagram for the Rankine gradual expansion.

Table 3 gives the thermodynamic values of the positions in the Rankine cycle for Figure 4.

Table 4 gives the thermodynamic properties of the ORC positions.

The temperature entropy diagram for the ORC gradual expansion is given in Fig. 5.

In Table 5, the thermodynamic results of all subcomponents are shown for both the R744 gradual expansion transcritical cycle, the steam gradual expansion Rankine cycle, and the ORC gradual expansion for R123 refrigerant; Heat exchange, energy and exergy analysis of system components, amount of fluid used in the system, power produced in the cycles and power consumed are calculated and presented separately.

The results were obtained by evaluating 1 kg/s air waste heat at 873.2 K with sub-cycles. In terms of energy efficiency, it is seen that the R744 gradual expansion has the highest energy and exergy efficiency. Cooling with water in heat exchangers reduces the exhaust efficiency. The mass flow requirement is highest in ORC, where R123 fluid is used. The energy efficiency for the entire system was calculated as 22.4% and the exergy efficiency for the entire system was

Table 4. Thermodynamic properties of ORC positions.

Location	T [K]	s [kJ/kg.K]	P [bar]	h [kJ/kg]	ex[kj/kg]
21. R123	363.2	1.689	6.259	436.9	35.53
22. R123	348.9	1.691	3.904	429.7	27.61
23. R123	363.2	1.724	3.904	441.4	29.75
24. R123	338.9	1.729	1.549	426.5	13.38
25. R123	313.2	1.67	1.549	407.2	11.34
26. R123	313.2	1.143	1.549	241.9	0.7897
27. R123	313.4	1.143	6.259	242.3	1.123
28. R123	363.2	1.304	6.259	297	8.599
To. R123	293.2	1.074	1	221.1	0
29. Water inlet	293.2	0.2972	1	84.22	0
30. Water outlet	303.2	1.074	1	221.1	0.7042

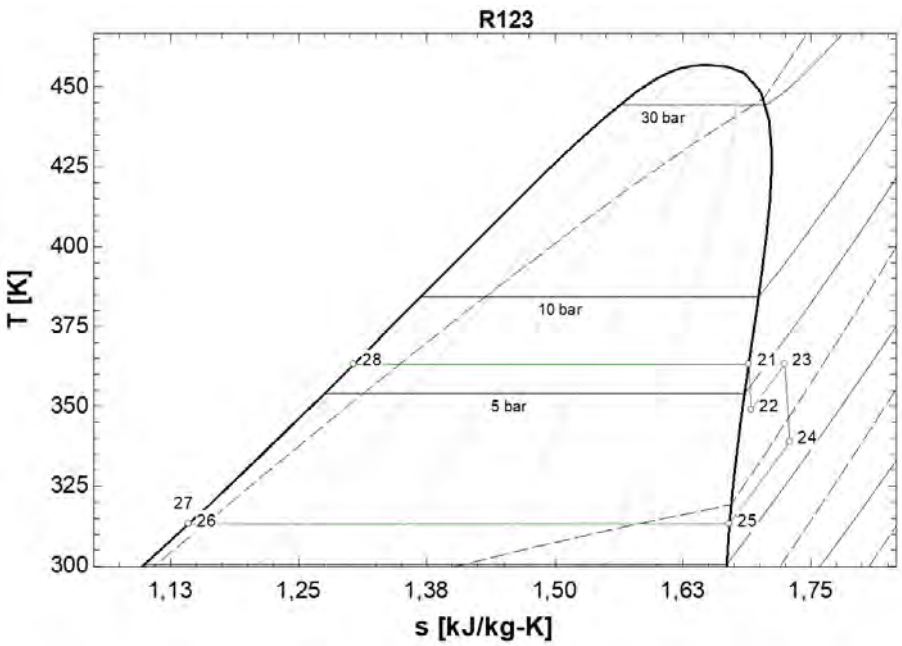

Figure 5. Temperature entropy diagram for ORC.

calculated as 60.7%. fei shows exergoenvironmental impact factor (0.138) is total exergy destruction rate, (37.049 kW) is input exergy rate(268.02 kW), Cei is exergoenvironmental impact coefficient (1.64), ψ_ex represents exergy efficiency of the system (60.7), Φei is exergoenvironmental impact index (0.227), Φeii represents exergoenvironmental impact improvement (4.39), fes is the exergy stability factor (60.7), Φest represents exergetic sustainability index (2.66). When Exergo Environment Analysis was made, exergy stability factor was found to be %60.7, exergetic sustainability index was found to be 2.66 . There is also 370 K waste heat. It is recommended to use a temperature of 370 K for drying units. Since carbon dioxide has a higher heat conduction coefficient than water, it accelerates heat transfer. At the same time, carbon dioxide has a lower viscosity than water, which allows the fluid to move more easily within the heat exchanger and reduces energy losses. The study results reveal compatible results when compared to other literature studies. The focus of this study will make a significant contribution towards increasing the usability of gradual expansion.

CONCLUSION

The rapid increase in consumer societies means an increase in waste facilities. Processing these waste products in facilities brings with it high energy costs. The gas turbines used in these facilities have serious waste heat. In this study, a thermodynamic proposal has been

Table 5. Thermodynamic results of all subcomponents.

location	H_2O Cycle	location	R123 Cycle	location	R744 Cycle
Q_{in}^{heat} [9-20]	408.1 kW	Q_{in}^{heat} [15-17]	358.9 kW	Q_{in}^{heat} [9-10]	124,5 kW
ψ H2Oexergy	4.3 %	ψ R123exergy	7.3 %	ψ R744exergy	78.96 %
η H2Oenergy	12 %	η R123energy	10.73 %	η R744energy	24.9 %
Ex pump.1	0.01 kW	Ex pump.2	0.06 kW	Ex comp1	1.71 kW
Ex Turb.3	1.15 kW	Ex Turb.5	1.17 kW	Ex Turb.1	1.08 kW
Ex Turb.4	2.78 kW	Ex Turb.6	2.49 kW	Ex Turb.2	1.76 kW
Ex HX3	90.6 kW	Ex HX4	21.52 kW	Ex HX1	1.889 kW
Ex HX4	21.52 kW	Ex HX5	26.67 kW	Ex HX2	20.12 kW
ϕ HX3	60.39 %	ϕ HX4	74.7 %	ϕ HX1	95.19 %
ϕ HX4	74.7 %	ϕ HX5	25.1 %	ϕ HX2	10.08 %
ϕ pump.1 [17-18]	92.37 %	ϕ pump.2 [26-27]	90.68 %	ϕ comp1 [1-2]	92.17 %
ϕ Turbine.3 [12-13]	93.25 %	ϕ Turbine.5 [21-22]	91.5 %	ϕ Turbine.1 [3-4]	92.92 %
ϕ Turbine.4 [14-15]	92.29 %	ϕ Turbine.6 [23-24]	91.26 %	ϕ Turbine.2 [5-6]	92.66 %
m water	0.1595 kg/s	m R123	1.739 kg/s	m R744	0.6608 kg/s
Wpump.1 [17-18]	0.1213 kW	Wpump.2 [26-27]	0.6402 kW	Wcompressor.1 [1-2]	21.88 kW
WTurbinr.3 [12-13]	15.93 kW	WTurbinr.5 [21-22]	12.61 kW	WTurbinr.1 [3-4]	14.19 kW
WTurbinr.4 [14-15]	33.31 kW	WTurbinr.6 [23-24]	25.98 kW	WTurbinr.2 [5-6]	22.25 kW
Q_{in}^{heat} [15-17]	358.9 kW	Q_{in}^{heat} [24-26]	321 kW	Q_{in}^{heat} [1-6]	109.9 kW
m air [20-10]	1 kg/s	m water [29-30]	7.676 kg/s	m water [7-8]	2.616 kg/s

put forward on how to reduce this waste heat into useful energy. Carbon dioxide's higher heat conduction coefficient accelerates heat transfer, while its lower viscosity allows for easier fluid movement within the heat exchanger, reducing energy losses. In terms of energy efficiency, it is seen that the R744 transcritical gradual expansion has the highest energy and exergy efficiency. Water cooling in heat exchangers reduces exergy efficiency. Since the cooling water has a low temperature, the temperature difference is high. This can increase heat transfer efficiency and improve exergy efficiency. The mass flow requirement is highest in ORC, where R123 fluid is used. The energy efficiency for the entire system was calculated as 22.4% and the exergy efficiency for the entire system was calculated as 60.7%. When Exergo Environment Analysis was made, exergy stability factor was found to be %60.7, exergetic sustainability index was found to be 2.66. It is recommended to use a temperature of 370 K for drying units. The study results reveal compatible results when compared to other literature studies.

As a result, reheating and increasing the temperature of the fluid using reheat or intermediate stage heating in gas turbines will provide a number of benefits such as increasing thermal efficiency, improving performance, having a wide operating range and optimizing control. This strategy will be an important design method used by engineers to ensure efficient operation of the facility with systems integrated into waste facilities.

ACKNOWLEDGEMENT

The author received no financial support for the research, authorship, and/or publication of this article.

CONFLICT OF INTEREST

Authors approve that to the best of their knowledge, there is not any conflict of interest or common interest with an institution/organization or a person that may affect the review process of the paper.

References

1. Arslan M, Yılmaz C. Thermodynamic Optimization and Thermoeconomic Evaluation of Afyon Biogas Plant assisted by organic Rankine Cycle for waste heat recovery. Energy. 2022; 248, 123487.
2. Özahi E, Tozlu A, Abuşoğlu A. Thermoeconomic multi-objective optimization of an organic Rankine cycle (ORC) adapted to an existing solid waste power plant. Energy conversion and management. 2018; 168, 308-319.

3. Ruwa TL, Abbasoğlu S, Akün E. Energy and Exergy Analysis of Biogas-Powered Power Plant from Anaerobic Co-Digestion of Food and Animal Waste. Processes. 2022; 10(5), 871.
4. Elbir A. Thermodynamic analysis of combined power cycle, combining heat from a waste heat source with sub-cycles. Thermal Science. 2023; 27(4 Part B), 3031-3041.
5. Mondal P, Samanta S, Zaman SA, Ghosh S. Municipal solid waste fired combined cycle plant: Techno-economic performance optimization using response surface methodology. Energy Conversion and Management. 2021; 237, 114133.
6. Tozlu A, Ozahi E, Abusoglu A. Thermodynamic and thermoeconomic analyses of an organic Rankine cycle adapted gas turbine cycle using S- CO2. Journal of the Faculty of Engineering and Architecture of Gazi University. 2018; 33(3).
7. Özahi E, Tozlu A, Abuşoğlu A. Thermoeconomic multi-objective optimization of an organic Rankine cycle (ORC) adapted to an existing solid waste power plant. Energy conversion and management. 2018; 168, 308-319.
8. Valencia Ochoa G, Cárdenas Gutierrez J, Duarte Forero J. Exergy, economic, and life-cycle assessment of ORC system for waste heat recovery in a natural gas internal combustion engine. Resources. 2020; 9(1), 2.
9. Wu X, Zhang N, Xie L, Ci W, Chen J, Lu S. Thermoeconomic Optimization Design of the ORC System Installed on a Light-Duty Vehicle for Waste Heat Recovery from Exhaust Heat. Energies. 2022; 15(12), 4486.
10. Ancona MA, Bianchi M, Branchini L, De Pascale A, Melino F, Peretto A, Torricelli N. Systematic comparison of ORC and S-CO2combined heat and power plants for energy harvesting in industrial gas turbines. Energies. 2021; 14(12), 3402.
11. Elbir A, Şahin ME, Özgür AE, Bayrakçi HC. Thermodynamic Analysis of A Novel Combined Supercritical CO2 And Organic Rankine Cycle. International Journal Of Engineering And Innovative Research. 2023; 5(1), 33-47.
12. Yang K, Zhang H, Song S, Yang F, Liu H, Zhao G, Yao B. Effects of degree of superheat on the running performance of an organic Rankine cycle (ORC) waste heat recovery system for diesel engines under various operating conditions. Energies. 2014; 7(4), 2123-2145.
13. Thekdi A, Nimbalkar SU. Industrial waste heat recovery-potential applications, available technologies and crosscutting r&d opportunities (No. ORNL/TM-2014/622). Oak Ridge National Lab. (ORNL), Oak Ridge, TN (United States). 2015.
14. Cengel YA, Boles MA. Thermodynamics: an engineering approach. McGraw-Hill New York. 2011.
15. Dincer I, Rosen MA. Exergy: energy, environment and sustainable development. Elsevier Science. 2012.
16. Bejan A, Tsatsaronis G, Moran M. Thermal design and optimization. New York: Jonh Wiley and. 1996
17. Sharifishourabi M. Energetic and Exergetic Analysis of a Solar Organic Rankine Cycle with Triple Effect Absorption System (Master's thesis, Eastern Mediterranean University (EMU)-Doğu Akdeniz Üniversitesi (DAÜ)). 2016.
18. Satheeshkumar A, Lim CW. The Performance Of Waste Heat Recovery Systems Using Steam Rankine Cycle And Organic Rankine Cycle For Power Generation, International Journal Of Engineering And Advanced Technology. 2019; 9(2),4172-4177.
19. Li M, Wang J, He W, Gao L, Wang B, Ma S, Dai Y. Construction and preliminary test of a low-temperature regenerative Organic Rankine Cycle (ORC) using R123. Renewable energy. 2013; 57, 216-222.
20. Hossain MJ, Chowdhury JI, Balta-Ozkan N, Asfand F, Saadon S, Imran M. Design optimization of supercritical carbon dioxide (S-CO2) cycles for waste heat recovery from marine engines. Journal of Energy Resources Technology. 2021; 143(12), 120901.
21. Klein SA. Engineering Equation Solver(EES). F-Chart Software, Version 10.835-3D. 2020.